AD-A128 181 DIFFRACTION BY PARALLEL PLATES WITH APPLICATION TO LENS ANTENNAS(U) ILLINOIS UNIV AT URBANA ELECTROMAGNETICS LAB L GRUN ET AL. SEP 80 UIEM-80-7 NSF-ENG77-20820 1/2

UNCLASSIFIED F/G 9/5 NL

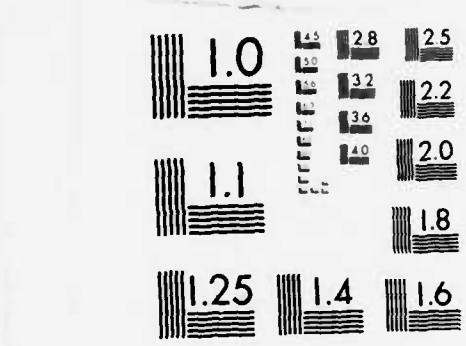

ELECTROMAGNETICS LABORATORY
SCIENTIFIC REPORT NO. 80-7

September 1980

DIFFRACTION BY PARALLEL PLATES WITH APPLICATION TO LENS ANTENNAS

L. GRUN
S. W. LEE

ELECTROMAGNETICS LABORATORY
DEPARTMENT OF ELECTRICAL ENGINEERING
ENGINEERING EXPERIMENT STATION
UNIVERSITY OF ILLINOIS AT URBANA-CHAMPAIGN
URBANA, ILLINOIS 61801

SUPPORTED BY
NATIONAL SCIENCE FOUNDATION
GRANT NSF-ENG-77-20820
AIR FORCE OFFICE OF
SCIENTIFIC RESEARCH
GRANT AFOSR 80-0179

"The views and conclusions contained in this document are those of the authors and should not be interpreted as necessarily representing the official policies or endorsements, either expressed or implied, of the Air Force Office of Scientific Research or the U. S. Government."

UNCLASSIFIED
SECURITY CLASSIFICATION OF THIS PAGE (When Data Entered)

REPORT DOCUMENTATION PAGE		READ INSTRUCTIONS BEFORE COMPLETING FORM
1. REPORT NUMBER	2. GOVT ACCESSION NO.	3. RECIPIENT'S CATALOG NUMBER
4. TITLE (and Subtitle) DIFFRACTION BY PARALLEL PLATES WITH APPLICATION TO LENS ANTENNAS		5. TYPE OF REPORT & PERIOD COVERED Scientific 6. PERFORMING ORG. REPORT NUMBER EM 80-7; UILU-ENG 80-2550
7. AUTHOR(s) L. Grun S. W. Lee		8. CONTRACT OR GRANT NUMBER(s) NSF-ENG-77-20820 AFOSR 80-0179
9. PERFORMING ORGANIZATION NAME AND ADDRESS Electromagnetics Laboratory Department of Electrical Engineering University of Illinois, Urbana, Illinois 61801		10. PROGRAM ELEMENT, PROJECT, TASK AREA & WORK UNIT NUMBERS Project/Task 2305J3
11. CONTROLLING OFFICE NAME AND ADDRESS National Science Foundation Washington, DC Air Force Office of Scientific Research Bolling AFB, DC 20332		12. REPORT DATE September 1980 13. NUMBER OF PAGES 133
14. MONITORING AGENCY NAME & ADDRESS (if different from Controlling Office) RADC/ACFC Hanscom AFB, MA 01731 (for AFOSR)		15. SECURITY CLASS. (of this report) Unclassified 15a. DECLASSIFICATION/DOWNGRADING SCHEDULE

16. DISTRIBUTION STATEMENT (of this Report)

Distribution is unlimited

17. DISTRIBUTION STATEMENT (of the abstract entered in Block 20, if different from Report)

18. SUPPLEMENTARY NOTES

The views and conclusions contained in this document are those of the authors and should not be interpreted as necessarily representing the official policies or endorsements, either expressed or implied, of the Air Force Office of Scientific Research or the U.S. Government.

19. KEY WORDS (Continue on reverse side if necessary and identify by block number)

Waveguide lens antenna, GTD, Diffraction by parallel plates, High frequency diffraction, Mutual coupling in lens antenna, Wiener-Hopf technique.

20. ABSTRACT (Continue on reverse side if necessary and identify by block number)

Scattering of an incident plane, or cylindrical, wave by a staggered parallel-plate waveguide is examined. Of particular interest are the modal coefficients of the unattenuated modes in the waveguide when the incident field is an E-wave. Several past approaches based on ray techniques are critically examined. It is found that they are not applicable when the stagger is small or when the incident field is a cylindrical wave. For the latter incidence, we introduce here an aperture field method, in which the modal coefficients are calculated through the Fourier decomposition

DD FORM 1 JAN 73 1473 EDITION OF 1 NOV 65 IS OBSOLETE

UNCLASSIFIED
SECURITY CLASSIFICATION OF THIS PAGE (When Data Entered)

of the scattered field at the waveguide aperture. To determine this scattered field, we apply the uniform asymptotic theory for the primary contribution, and the spectral theory for the first interaction.

Extensive numerical data show that the aperture field method gives accurate results in canonical problems whose exact solutions are known. As an application to the design of the constrained waveguide lens antenna, our method enables one to determine the field distributed over the lens in a more exact manner.

UILU-ENG-80-2550

Electromagnetics Laboratory Report No. 80-7

DIFFRACTION BY PARALLEL PLATES WITH APPLICATION TO LENS ANTENNAS

by

L. Grun

S. W. Lee

Electromagnetics Laboratory
Department of Electrical Engineering
University of Illinois at Urbana-Champaign
Urbana, Illinois 61801

Scientific Report

September 1980

Supported by

Grant No. NSF-ENG-77-20820
National Science Foundation
Washington, D.C.

Grant No. AFOSR 80-0179
Air Force Office of Scientific Research
Bolling AFB, Washington, D.C. 20332

Monitoring Agency

RADC/ACFC
Hanscom AFB, MA 01731

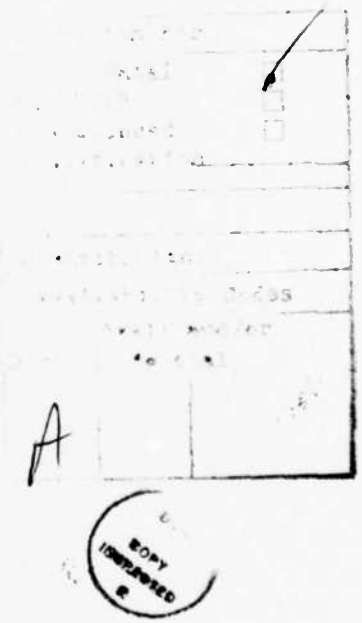

ABSTRACT

Scattering of an incident plane, or cylindrical, wave by a staggered parallel-plate waveguide is examined. Of particular interest are the modal coefficients of the unattenuated modes in the waveguide when the incident field is an E-wave. Several past approaches based on ray techniques are critically examined. It is found that they are not applicable when the stagger is small or when the incident field is a cylindrical wave. For the latter incidence, we introduce here an aperture field method, in which the modal coefficients are calculated through the Fourier decomposition of the scattered field at the waveguide aperture. To determine this scattered field, we apply the uniform asymptotic theory for the primary contribution, and the spectral theory for the first interaction.

Extensive numerical data show that the aperture field method gives accurate results in canonical problems whose exact solutions are known. As an application to the design of the constrained waveguide lens antenna, our method enables one to determine the field distributed over the lens in a more exact manner.

TABLE OF CONTENTS

LIST OF FIGURES

BASIC CONVENTIONS

1: MKS units and $e^{-i\omega t}$ time variation are used.

2: $\gamma = (\alpha^2 - k^2)^{1/2} = -i(k^2 - \alpha^2)^{1/2}$, where $\alpha = \sigma + i\tau$ and

$$k = k_1 + ik_2 \quad , \quad k_2 << k_1$$

3: The Fourier pair is

$$\Phi(x,\alpha) = \frac{1}{\sqrt{2\pi}} \int_{-\infty}^{\infty} \phi(x,z) e^{i\alpha z} \, dz$$

$$\phi(x,z) = \frac{1}{\sqrt{2\pi}} \int_{-\infty}^{\infty} \Phi(x,\alpha) e^{-i\alpha z} \, d\alpha$$

4: The Fresnel integral is given by

$$F(x) = \frac{e^{-i\pi/4}}{\sqrt{\pi}} \int_{x}^{\infty} e^{it^2} \, dt \quad , \quad x \text{ real.}$$

5:
$$\text{sgn}(x) = \begin{cases} +1 & x > 0 \\ -1 & x < 0 \end{cases}$$

6: $$g(kr) = \frac{e^{i(kr+\pi/4)}}{\sqrt{8\pi kr}}$$

7: C = Euler's Constant = .57721 ...

8: $\text{sinc}(x) = \sin(x)/x$

9: $$H(x \leq b) = \begin{cases} 1 & \text{if} \quad x \leq b \\ 0 & \text{otherwise} \end{cases}$$

I. INTRODUCTION

This thesis considers the problem of the scattering of a plane or cylindrical wave by the staggered parallel-plate guide in Figure 1 when the stagger dimension "ℓ" is of moderate size compared to the wavelength. In particular, we are interested in finding the modal coefficients of the unattenuated modes when the incident field is an E-wave. The problem goes back to the early 1940's when Kock [18] and Ruze [28] realized that a waveguide can serve as a refracting medium and wide angle scanning antennas can be designed very much the same way as natural dielectric lenses. While these designs proved successful, researchers immediately understood that for a thorough, quantiative design the scattering of a plane wave by the guide, which constitutes the basic element of the lens, had to be well-understood. Recent developments in satellite communications have revived interest in the waveguide lens [13], and make the problem considered here all the more relevant.

Among the first to consider the scattering of a plane wave by a guide have been Carlson and Heinz [10], Lengyel [22] and Whitehead [32]. However, they studied the problem in which the parallel-plate guide was but the single element of an infinite, periodic array of guides. In such a case, the Wiener-Hopf Method and other classical techniques [32] gave an exact solution. These solutions applied to the single, isolated guide, however, give poor results and the isolated guide has, generally, no exact, closed-form solution. The one exception to this statement is when the stagger "ℓ " is zero. Then, the Wiener-Hopf Method may be used and the solution obtained in the manner outline in Chapter II. While this solution is useful in its own right, it casts little light on how to proceed when "ℓ" is not zero or very small.

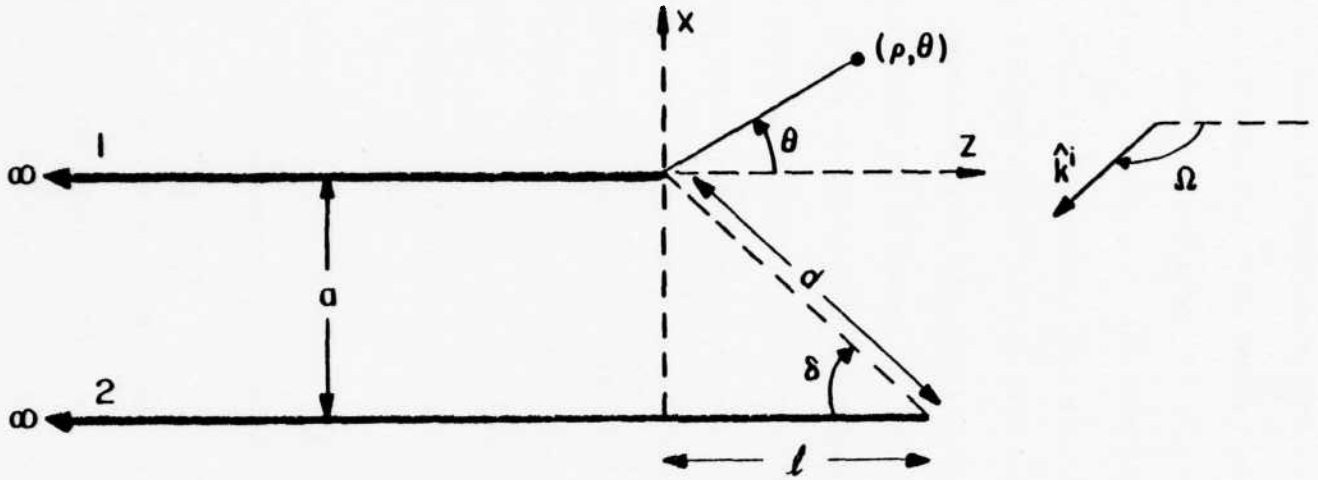

$\delta > 0$

$|\theta| \leq \pi$ Positive Counterclockwise

$|\Omega| > \pi/2$ Positive Counterclockwise

Figure 1. Diffraction of a plane wave by a staggered parallel-plate waveguide.

The introduction of ray techniques to the study of scattering by Keller [17], and later improvement to the theory of Aklauwalia, Lewis and Boersma [1] provided for a new way to attack the problem. Instead of obtaining the full solution, rays can be used to follow each scattering off the plates, and from each scattering the modal coefficients computed by Fourier series analysis. This approach was first presented by Yee, Keller and Felsen in 1968 [30]; a critique of this method is given in Chapter III. In Chapter III, we show that the YKF method presents a difficult singularity problem when "ℓ" is not zero and, furthermore, makes use of unwarranted assumptions about the ray nature of the scattered fields in computing the effects of multiple scattering between the plates. A much more rigorous use of ray optics for the unstaggered guide is given by Boersma [2], [5], but his solution is not easily extended to the staggered guide. The Modified Diffraction Coefficient, given by Lee [19], [20], is a new way to account for the multiple scattering in toto, but the MDC, which combines functional analysis and ray optics, can be properly used only when "ℓ" is large - usually larger than one wavelength. Furthermore, all the previous works mentioned above examined the incident plane wave case only.

The approach to the problem in this thesis is to first find an accurate approximation of the total field on the guide aperture, and then by Fourier decomposition compute the modal coefficients. Because of the difficulty in formulating the multiple scattered fields when "ℓ" is not zero or large we include in the aperture field, for the incident plane wave, only the first interaction, or scattering, between the plates of the guide. Previous plane-wave investigations of the scattered field that included the first interaction were conducted by Jones [16] and Boersma [4], but their results

respectively were in terms of very elaborate doubly infinite integrals and series. In this thesis the primary scattering field is given by the canonical or UAT solution to the scattering by a half-plane, and for the plane wave the first interaction is found by the Spectral Theory of Diffraction, recently introduced by Mittra and Rahmat-Samii [26]. This formulation of the aperture field, given in Chapter IV, is relatively easy to compute and is equally valid for all stagger size and plate separation "a." Using this aperture field, extensive data for the modal coefficient of the important TE_{10} mode are presented in Chapter IV, and an application to the study of waveguide lens antennas is given. Finally, conclusions are presented in Chapter VI.

Finally, we note several conventions used in this thesis. (1) The time factor is $e^{-i\omega t}$ and is suppressed. (2) All angles are between $-\pi$ and $+\pi$, positive counterclockwise, unless otherwise noted. (3) The E-wave problem is examined in detail, the extension to the H-wave problem is only stated.

II. SUMMARY OF THE WIENER-HOPF METHOD, THE SPECTRAL THEORY OF DIFFRACTION (STD) AND THE UNIFORM ASYMPTOTIC THEORY OF DIFFRACTION (UAT)

For convenience of reference and as an introduction to the notation used in this work, the Wiener-Hopf Method, the Spectral Theory of Diffraction, and the Uniform Asymptotic Theory of Diffraction are briefly summarized below.

A. The Wiener-Hopf Method

Before we come to the problem of scattering by a half-plane, a quick discussion of some elements of the Fourier transform complex number theory relevant to the Wiener-Hopf Method is presented.

A.1. Mathematical preliminaries

First, if $\phi(x,z)$ and $\Phi(x,\alpha)$ form a Fourier transform pair, with $\alpha = \sigma + i\tau$ and if $\phi(x,z)$ has an asymptotic behavior given by $\phi(x,z) \sim Ae^{\tau^- z}$, as $z \to +\infty$, then the half-range Fourier transform, $\Phi_+(x,\alpha)$, defined by

$$\Phi_+(x,\alpha) = \frac{1}{\sqrt{2\pi}} \int_0^\infty \phi(x,z) e^{i\alpha z}\, dz \quad , \tag{II.1}$$

will be analytic in the region $\tau > \tau^+$. This statement is true for any $\phi(x,z)$ that is "well-behaved" and for any kernel that is continuous in α and z and analytic in z. In II.1, it is $e^{i\alpha z}$. A more rigorous formulation of the sufficient conditions involved in this discussion can be found in [25] or [29]. We assume throughout that $\phi(x,z)$ is such that the conditions in [25] or [29] are indeed satisfied and the final results may be applied in a straightforward manner.

Likewise, if $\phi(x,z) \sim Be^{\tau^+ z}$, $z \to -\infty$, then $\Phi_-(x,\alpha)$, which is given by

$$\Phi_-(x,\alpha) = \frac{1}{\sqrt{2\pi}} \int_{-\infty}^0 \phi(x,z) e^{i\alpha z}\, dz \quad , \tag{II.2}$$

is analytic in the region $\tau < \tau^+$. Note that the subscripts "+" and "-" can now be used to indicate that the function involved is analytic in some "plus" or "minus," that is, upper or lower region in the α plane.

We now define two functions $\phi_{(+)}(x,z)$ and $\phi_{(-)}(x,z)$ as

$$\phi_{(+)}(x, z) = \begin{cases} \phi(x, z) & z > 0 \\ 0 & z < 0 \end{cases} \tag{II.3a}$$

and

$$\phi_{(-)}(x, z) = \begin{cases} 0 & z > 0 \\ \phi(x, z) & z < 0 \end{cases} . \tag{II.3b}$$

Then, from the analytic properties of Φ_- and Φ_+ in their respective regions, it is easily shown that $\phi_{(+)}$, Φ_+ and $\phi_{(-)}$, Φ_- are Fourier transform pairs.

Also essential to the Wiener-Hopf method is the factorization and decomposition of complex-valued functions. By factorization, we mean expressing a function $G(\alpha)$ as the product of "plus" and "minus" functions, that is, $G(\alpha) = G_+(\alpha)G_-(\alpha)$, where $G_+(\alpha)$ is regular for $\tau > \tau^-$ and $G_-(\alpha)$ is regular for $\tau < \tau^+$, τ^-, τ^+ some numbers. For a well-posed problem, we will have $\tau^+ > \tau^-$ so that a region exists in which $G_+(\alpha)$ and $G_-(\alpha)$ are both regular. In contrast, decomposition refers to expressing a function $S(\alpha)$ as a sum of "plus" and "minus" functions such that $S(\alpha) = S_+(\alpha) + S_-(\alpha)$, where, as before, we expect to find some region, $\tau^- < \tau < \tau^+$, in which $S_+(\alpha)$ and $S_-(\alpha)$ are both analytic.

A useful formula that is later used for factoring an entire, even function $G(\alpha)$ is

$$G(\alpha) = G(0) \prod_{i=1}^{\infty} \left(1 - \frac{\alpha}{i\gamma_n}\right) e^{-i\alpha/an} \prod_{i=1}^{\infty} \left(1 + \frac{\alpha}{i\gamma_n}\right) e^{+i\alpha/an} \tag{II.4}$$

where $\pm i\gamma_n$ are the simple zeroes of $G(\alpha)$ and $\gamma_n \to an + b$, $n \to \infty$. It is obvious that the first product is analytic in the upper-half-plane given by $\tau > \tau^-$, where τ^- is determined by the location of γ_0 in the α plane.

For decomposition of a function $S(\alpha)$ analytic in some strip $\tau^- < \tau < \tau^+$, and which has the property that $|S(\alpha)| \to 0$ uniformly as $|\sigma| \to \infty$ within that strip, we will have occasion to use the following formulas.

$$S_+(\alpha) = \frac{1}{2\pi i} \int_{-\infty+ic}^{\infty+ic} \frac{S(\beta)}{(\beta - \alpha)}\, d\beta \qquad \tau < c < \tau^+ \tag{II.5a}$$

and

$$S_-(\alpha) = -\frac{1}{2\pi i} \int_{-\infty+id}^{\infty+id} \frac{S(\beta)}{(\beta - \alpha)}\, d\beta \qquad \tau^- < d < \tau^+ \quad . \tag{II.5b}$$

That is, within the strip, using Equations (II.5a) and (II.5b), we can write $S(\alpha) = S_+(\alpha) + S_-(\alpha)$.

The above equations for decomposition are also useful for factorization. If $G(\alpha)$ is analytic and nonzero in some strip $a < \tau < b$, then by taking $\ln G_+(\alpha)G_-(\alpha)$ we can use (II.5a) and (II.5b) to find

$$G_+(\alpha) = \exp\left[\frac{1}{2\pi i} \int_{-\infty+ic}^{\infty+ic} \frac{\ln G(\alpha)}{(\beta - \alpha)}\, d\beta\right] \qquad \tau^- < c < \tau^+ \tag{II.6a}$$

and

$$G_-(\alpha) = \exp\left[-\frac{1}{2\pi i} \int_{-\infty+id}^{\infty+id} \frac{\ln G(\alpha)}{(\beta - \alpha)}\, d\beta\right] \qquad \tau^- < d < \tau^+ \quad . \tag{II.6b}$$

Now, however, we require that within the strip $|G(\alpha)| \to 1$ uniformly as

$|\sigma| \to \infty$. Notice that, because of the use of the exponential, $G_+(\alpha)$ and $G_-(\alpha)$ are also nonzero in their regions of regularity. Other factorization and decomposition formulas can be found in [24] or [25]. Having finished these mathematical preliminaries, we now come to the problem that illustrates the three methods in this chapter - scattering by a half plane.

A.2. Scattering by a half-plane

Consider the problem in Figure 2. We wish to find the scattered field when the incident field is

$$\phi^i(x,z) = e^{ik(x\sin\Omega+z\cos\Omega)} = e^{ik\rho\cos(\Omega-\theta)} \tag{II.7}$$

where ϕ^i can be E_y^i for an E wave, and H_y^i for an H wave. Without loss of generality, we place the restriction $\pi > \Omega > 0$. There are now two ways to start formulating the Wiener-Hopf problem: (a) use the Green's function method which then leads to an integral equation, or (b) use the differential equation. Although the Green's function method is more general, the second approach, called Jones' Method [15], is simpler and clearly shows the requirements for the Wiener-Hopf solution.

We now examine the E-wave problem in some detail and later state the equivalent results for the H-wave. First let $\phi^t = \phi^s + \phi^i$, ϕ^s being the scattered field. Then ϕ^s satisfies the source-free Helmhotz equation

$$\partial_x^2\phi^s + \partial_z^2\phi^s + k^2\phi^s = 0 \tag{II.8a}$$

with the boundary condition

$$\phi^s(0,z) = -\phi^i(0,z) \quad -\infty < z < 0 \quad . \tag{II.8b}$$

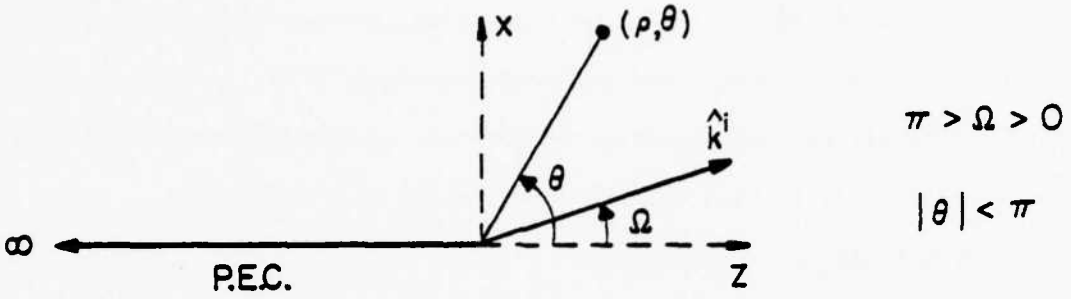

Figure 2. Diffraction of a plane wave by a half-plane.

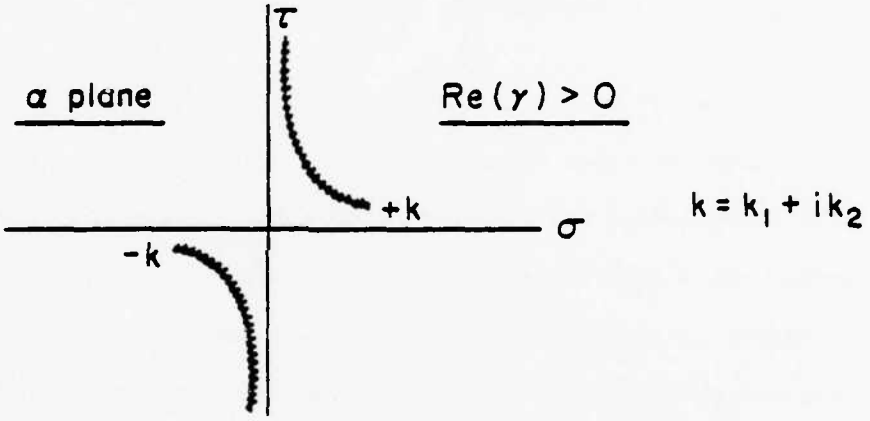

Figure 3. Branch cuts of $\gamma = (\alpha^2 - k^2)^{1/2}$.

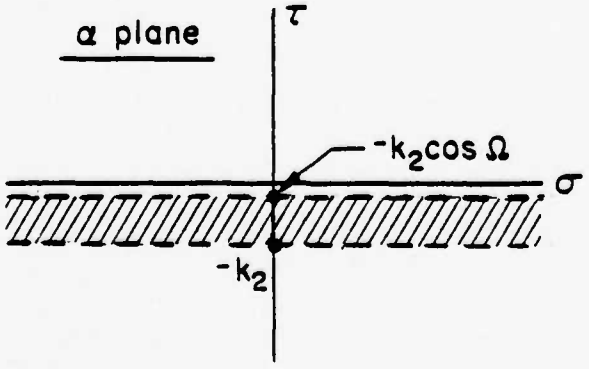

Figure 4. Region of the Wiener-Hopf Equation (II.13).

A small but finite loss is introduced by letting $k = k_1 + ik_2$. The Wiener-Hopf solution begins by transforming (II.8a) and (II.8b) into the spectral or transform domain, by multiplying both sides of (II.8a) and (II.8b) by $e^{i\alpha z}/\sqrt{2\pi}$ and integrating over all z. If this operation is performed Equations (II.8a) and (II.8b) then become

$$\partial_x^2\phi^s(x, \alpha) - \gamma^2\phi^s(x, \alpha) = 0 \qquad \text{(II.9a)}$$

and

$$\phi_-^s(0, \alpha) = -\phi_-^i \ (0, \alpha) \qquad \tau < -k_2 \cos \Omega \ , \qquad \text{(II.9b)}$$

where the subscript "minus" appears because (II.8b) is true only for $-\infty < z < 0$. The function $\gamma = (\alpha^2 - k^2)^{1/2}$ is defined by its value on the upper or proper sheet, as shown in Figure 3. These branch cuts insure that the radiation condition is satisfied for all α on the real-number line and that $\mathrm{Re}(\gamma) > 0$ on the entire sheet. Note that γ is analytic in the region $k_2 > \tau > -k_2$.

The solution to (II.9b) is

$$\phi^s(x, \alpha) = A(\alpha)e^{-\gamma|x|} \ , \qquad \text{(II.10)}$$

so that at $x = 0$ we have

$$-\phi_-^i(0, \alpha) + \phi_+^s(0,\alpha) = A(\alpha) \qquad \text{(II.11)}$$

where, since ϕ_+^s satisfies the radiation condition, ϕ_+^s is analytic for $\tau > -k_2$. Defining $J_-(\alpha)$ as being proportional to the transform of the total induced current on the plate, we get

$$J_-(\alpha) = \tfrac{1}{2}\{\partial_x\phi_-^s(0^+, \alpha) - \partial_x\phi_-^s(0^-, \alpha)\} = -\gamma A(\alpha) \ . \qquad \text{(II.12)}$$

Combining (II.12) with (II.11), we obtain the Wiener-Hopf equation

$$\phi_+^s(0, \alpha) + \left[\frac{1}{\gamma}\right] J_-(\alpha) - \phi_-^i(0, \alpha) = 0, \quad -k_2 \cos \Omega > \tau > -k_2, \tag{II.13}$$

(see Figure 4), which is in the standard Wiener-Hopf form

$$R(\alpha)\phi_+^s(\alpha) + G(\alpha)J_-(\alpha) + T(\alpha) = 0 \quad \tau^+ > \tau > \tau^- \quad , \tag{II.14}$$

with R, G, T given and analytic in $\tau^+ > \tau > \tau^-$ and the unknowns ϕ_+^s, J_- analytic in $\tau > \tau^-$, $\tau < \tau^+$, respectively. Although Equations (II.13) and (II.14) are algebraic equations in two unknowns, by using the Wiener-Hopf Method, a solution is still possible.

The first step is to factor $G(\alpha) = (1/\gamma)$ into its "plus" and "minus" parts. For this particular case, it is obvious that

$$G_+(\alpha) = (\alpha + k)^{-1/2} \quad , \tag{II.15a}$$

and

$$G_-(\alpha) = (\alpha - k)^{-1/2} \quad . \tag{II.15b}$$

Dividing both sides by $G_+(\alpha)$, it follows that

$$\phi_+^s(0, \alpha)(\alpha + k)^{1/2} + (\alpha - k)^{1/2} J_-(\alpha) - (\alpha + k)^{1/2} \phi_-^i(0, \alpha) = 0. \tag{II.16}$$

The next step is to decompose $(\alpha + k)^{1/2}\phi_-^i$. Again, the decomposition can be done by inspection, and with $\phi_-^i(0,\alpha)$ given by

$$\phi_-^i(0, \alpha) = -i/[\sqrt{2\pi}(\alpha + k \cos \Omega)], \quad \tau < -k_2 \cos \Omega \quad , \tag{II.17}$$

one can write

$$\frac{i(\alpha + k)^{1/2}}{\sqrt{2\pi}(\alpha + k\cos\Omega)} = \frac{i[(\alpha + k)^{1/2} - (k - k\cos\Omega)^{1/2}}{\sqrt{2\pi}(\alpha + k\cos\Omega)}$$

$$+ \frac{i}{\sqrt{2\pi}} \frac{(k - k\cos\Omega)^{1/2}}{(\alpha + k\cos\Omega)} \quad . \tag{II.18}$$

The first term on the right-hand side is $S_+(\alpha)$ which, because of the cancellation of the singularity at $\alpha = -k\cos\Omega$, is analytic for $\tau > -k_2$. The second term on the right is $S_-(\alpha)$, and it is obviously analytic for $\tau < -k_2 \cos\Omega$. Combining (II.15a) thru (II.18), we have

$$(\alpha + k)^{1/2}\, \phi^s_+(0, \alpha) - \frac{i[(\alpha + k)^{1/2} - (k - k\cos\Omega)^{1/2}}{\sqrt{2\pi}(\alpha + k\cos\Omega)}$$

$$= -\frac{J_-(\alpha)}{(\alpha - k)^{1/2}} - \frac{i(k - k\cos\Omega)^{1/2}}{\sqrt{2\pi}(\alpha + k\cos\Omega)} \tag{II.19}$$

for $-k_2\cos\Omega > \tau > -k_2$. The right side of (II.19) is analytic in the upper-half plane, $\tau > -k_2$, the left side analytic in the lower-half plane, $\tau < -k_2\cos\Omega$. Since there is a region where both sides of (II.19) are analytic and equal to each other, it is possible to analytically continue both sides of (II.19) into the entire complex plane, and obtain the equations,

$$(\alpha + k)^{1/2}\, \phi^s_+(0, \alpha) - \frac{i[(\alpha + k)^{1/2} - (k - k\cos\Omega)^{1/2}}{\sqrt{2\pi}(\alpha + k\cos\Omega)} = P(\alpha) \tag{II.20a}$$

and

$$-\frac{J_-(\alpha)}{(\alpha - k)^{1/2}} - \frac{i(k - k\cos\Omega)^{1/2}}{\sqrt{2\pi}(\alpha + k\cos\Omega)} = P(\alpha) \quad , \tag{II.20b}$$

where $P(\alpha)$ is an entire function. We see that the Wiener-Hopf Method

leads to two equations in which the two unknowns may be solved for within some entire function, $P(\alpha)$.

To completely solve (II.20a) or (II.20b), another condition must be applied to find $P(\alpha)$. In electromagnetics, this condition is the "edge condition," [23], which states that no charge may accumulate at the edge. This, in turn, implies that $\phi^s(\rho, \theta) = 0(\rho^\delta)$, $\rho \to 0$, $1 > \delta > 0$, and, therefore, $\phi_+^s(0, \alpha) = 0(\alpha^{-1-\delta})$ as $|\alpha| \to \infty$. Inspecting the asymptotic behavior of (II.20a) and using Liouville's theorem $P(\alpha)$ must be zero. Then, from (II.20a) and (II.12)

$$J_-(\alpha) = -\frac{i(k - k\cos\Omega)^{1/2}(\alpha - k)^{1/2}}{\sqrt{2\pi}(\alpha + k\cos\Omega)} = -\gamma A(\alpha) \quad . \tag{II.21}$$

Finally, solving for $A(\alpha)$ and inverse Fourier transforming $\phi^s(x, \alpha)$ we obtain the desired result

$$\phi^s(x, z) = \frac{1}{2\pi}\int_{-\infty}^{\infty}\left[\frac{2(k - k\cos\Omega)^{1/2}(k - \alpha)^{1/2}}{(\alpha + k\cos\Omega)}\right]\frac{e^{-\gamma|x|}}{2\gamma}e^{-i\alpha z}\,d\alpha. \tag{II.22}$$

For an H-wave, $\phi^s = H_y^s$, the boundary condition in the transform domain is $\partial_x\phi_-^s(0, \alpha) = -\partial_x\phi_-^i(0, \alpha)$, $\phi^s(x, \alpha) = \mathrm{sgn}(x)A(\alpha)\,e^{-\gamma|x|}$, and the current, which is polarized in the z direction, is

$$J_-(\alpha) = \frac{1}{2}\{\phi_-^s(0^+, \alpha) - \phi_-^s(0^-, \alpha)\} = A(\alpha) \quad . \tag{II.23}$$

If the same considerations as for the E-wave are followed, the scattered field for the H wave is

$$\phi^s(x, z) = \frac{\mathrm{sgn}(x)}{2\pi}\int_{-\infty}^{\infty}\left[\frac{2(k + k\cos\Omega)^{1/2}(\alpha + k)^{1/2}}{(\alpha + k\cos\Omega)}\right]\frac{e^{-\gamma|x|}}{2\gamma}e^{-i\alpha z}\,dz. \tag{II.24}$$

In summary, once an equation of the type (II.14) is derived, the Wiener-Hopf method allows one to solve it for its two unknowns within some entire function $P(\alpha)$. The essential features of the Wiener-Hopf Method are then factorization and decomposition, the use of analytic continuation, and the necessity of imposing another physical constraint to obtain a full solution.

B. Spectral Theory of Diffraction (STD)

In the course of investigating the coupling into a waveguide, we need to consider the scattering by a half-plane of rather complicated incident fields. While the problem of a plane-wave diffraction by a half plane has been extensively analyzed since Sommerfeld's solution in 1896, the diffraction of a more general incident field has only recently been examined. The first treatment of an incident field other than a plane wave was by Carslaw in 1899 who considered the very special case of an incident field due to an isotropic line source. More recent work with the isotropic line field can be found in Born and Wolf [8], and in the book by Clemmow [11], who examined the problem through the use of a plane-wave spectrum representation. A high frequency or asymptotic solution to this problem and of a more general line source field was studied by Boersma and Lee employing the U.A.T. formalism [6], [7]. The first rigorous and extensive study of the case of an arbitrary incident field scattered by a half-plane was done by Rahmat-Samii and Mittra [26], and their approach, labeled the Spectral Theory of Diffraction, is outlined below.

We start by examining in more detail the expression for the scattered field of an incident plane wave as given by Equations (II.22) and (II.24).

Both E and H waves can be conveniently considered by letting

$$\varepsilon = \begin{cases} -1 & \text{E wave} \\ +1 & \text{H wave} \end{cases} . \tag{II.25}$$

The "spectral diffraction coefficient" is defined as

$$X(k_z, \alpha) = \frac{2(k + \varepsilon k \cos \Omega)^{1/2}(k + \varepsilon\alpha)^{1/2}}{(\alpha + k \cos \Omega)} \tag{II.26}$$

where the square roots are defined by taking the cut just below the negative real axis in the α plane. The scattered field can therefore be now written as

$$\phi^s(x, z) = \begin{pmatrix} 1 \\ \operatorname{sgn}(x) \end{pmatrix} \frac{1}{2\pi} \int_{-\infty}^{\infty} X(k_z, \alpha) \frac{e^{-\gamma|x|}}{2\gamma} e^{-i\alpha z} \, d\alpha, \quad \text{for} \begin{pmatrix} \text{E wave} \\ \text{H wave} \end{pmatrix} . \tag{II.27}$$

Note that $(e^{-\gamma|x|}/2\gamma)$ is the Fourier transform, with respect to z, of $iH_0^1(k\sqrt{x^2 + z^2})/4$, which is the Green's function for a line source radiating in free space.

Introducing the change of variables $x = \rho \sin \theta$, $z = \rho \cos \theta$ $\alpha = -k \cos \psi$ and $\gamma = -ik \sin \psi$ into (II.27), one arrives at

$$\phi^s(\rho, \theta) = \begin{pmatrix} 1 \\ \operatorname{sgn}(\theta) \end{pmatrix} \frac{i}{4\pi} \int_{\Gamma} \chi(\Omega, \psi) e^{ik\rho \cos (\psi - |\theta|)} \, d\psi \quad . \tag{II.28}$$

In the preceding equation, ψ is the complex angle defined on the path Γ shown in Figure 5, and

$$\chi(\Omega, \psi) = X(k \cos \Omega, -k \cos \psi) = \chi_i(\Omega, \psi) + \varepsilon\chi_r(\Omega, \psi) \tag{II.29}$$

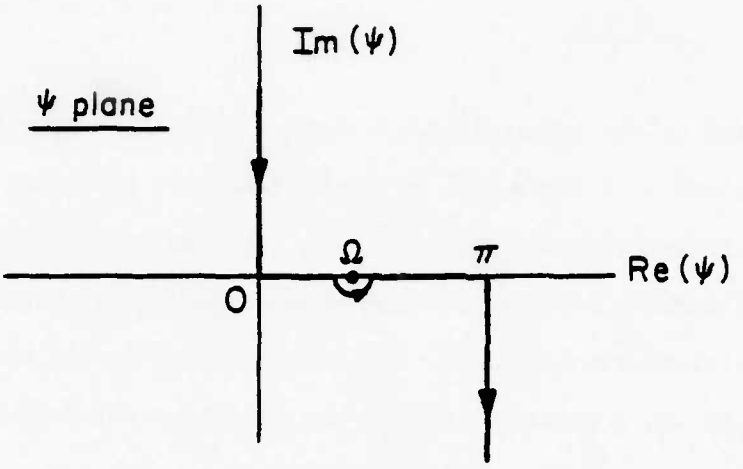

Figure 5. Integration path Γ for integral representation (II.28).

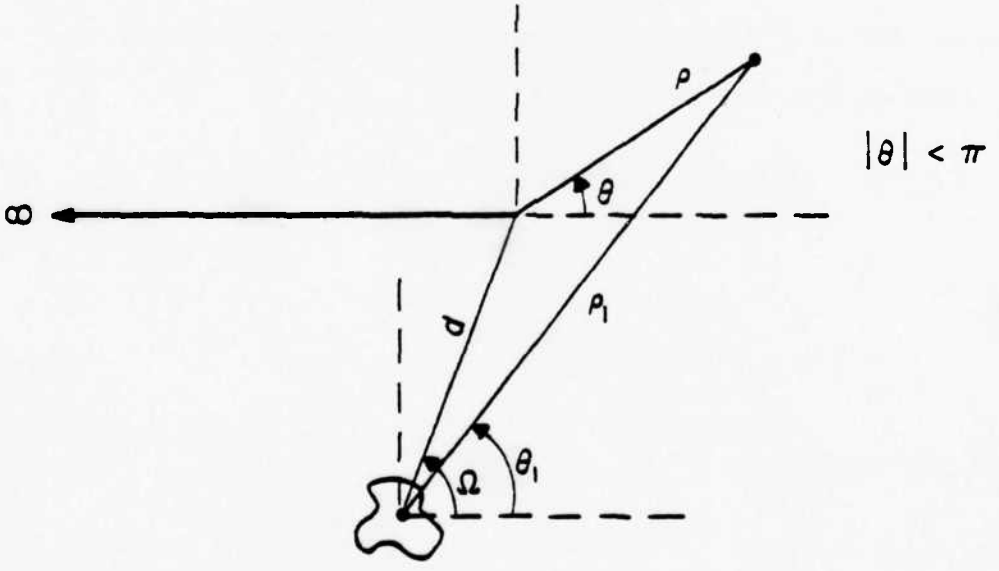

Figure 6. Diffraction of an arbitrary field by a half-plane.

where

$$\chi_{i,r} = \varepsilon \csc\left(\frac{\Omega \mp \psi}{2}\right) \quad . \tag{II.30}$$

Clearly χ_i and χ_r are infinite at $\psi = \Omega$ and at $\psi = -\Omega$, respectively. These two values of ψ correspond to the incident and reflected shadow boundaries appearing in the GTD technique. As a matter of fact, the spectral diffraction coefficient is precisely the angular part of Keller's diffraction coefficient, when ψ is replaced by the observation angle θ. Although χ tends to infinity at the shadow boundaries, the scattered field, as evident in (II.27), does not.

From (II.27) and the fact that $(e^{-\gamma|x|}/2\gamma)$ is the Fourier transform of the Green's function $(iH_0^1(k\rho)/4)$, it follows that $\chi(\Omega, \psi)$ is proportional to the Fourier transform of the induced current on the plate. We may, therefore, define $\chi^{po}(\Omega, \psi)$ as the transform of the physical optics part of the current and write

$$\chi^{po}(\Omega, \psi) = \chi_i^{po}(\Omega, \psi) + \varepsilon\chi_r^{po}(\Omega, \psi) \tag{II.31}$$

where

$$\chi_{i,r}^{po} = \mp \operatorname{ctn}\left(\frac{\Omega \mp \psi}{2}\right) \quad . \tag{II.32}$$

Then χ^f, defined by

$$\chi^f(\Omega, \psi) = \chi(\Omega, \psi) - \chi^{po}(\Omega, \psi) \quad , \tag{II.33}$$

is bounded everywhere and could be called the spectral fringe diffraction coefficient. It is used in scalar aperture diffraction.

Consider again the scattered field in (II.27). This spectral integral can be exactly expressed in terms of the Fresnel integral, viz.,

$$\phi^s(\rho, \theta) = -e^{ik\rho\cos(\Omega-\theta)}F(-\xi^i) + \varepsilon e^{ik\rho\cos(\Omega+\theta)}F(\xi^r) \tag{II.34}$$

where the Fresnel integral is

$$F(x) = \frac{e^{-\pi/4}}{\sqrt{\pi}} \int_x^\infty e^{it^2}\, dt \tag{II.35}$$

and

$$\xi^{i,r} = \mp\sqrt{2k\rho}\, \sin\left(\frac{\Omega \mp \theta}{2}\right) \quad . \tag{II.36}$$

So far in this development, we have tacitly assumed that Ω is real. However, using the argument of analytic continuation one can show that if the angle of incidence is a complex number ω, Equation (II.34) is still a valid solution but with Ω replaced by the complex ω in (II.34) and (II.36).

With the solution for a plane wave of complex incident angle available, the case of an arbitrary incident field on a half plane as shown in Figure 6 can now be examined. We assume the incident field can be placed in a spectral representation as

$$\phi^i(\rho_1, \theta_1) = \frac{i}{4\pi} \int_{\Gamma'} P(\omega) e^{ik\rho_1 \cos(\omega - |\theta_1|)}\, d\omega \tag{II.37}$$

where $\rho_1 = 0$ denotes the phase center of the incident field and the path Γ' is the same as the path Γ but where Γ' accounts for any singularities in $P(\omega)$. Expressing ϕ^i now in terms of the coordinates attached to the plate

$$\phi^i(\rho, \theta) = \frac{i}{4\pi} \int_{\Gamma'} [P(\omega)e^{ikdcos\ (\omega-\Omega)}]e^{ik\rho\ cos(\omega-\theta)}d\omega \qquad (II.38)$$

when $\rho \sin \phi > -d \sin \Omega$. The incident field is then a spectrum of plane waves incident at a complex angle ω with a weight, or spectrum density, given by the term in the brackets. Since (II.34) is the solution for a plane wave incidence, even with a complex angle of incidence, by superposition the scattered field due to an arbitrary incident field is

$$\phi^s(\rho, \theta) = \frac{1}{4\pi i} \int_{\Gamma'} [P(\omega)e^{ikdcos(\omega-\Omega)}]\{e^{ik\rho cos(\omega-\theta)}F(-\xi^i)$$

$$- \varepsilon e^{ik\rho cos(\omega+\theta)}F(\xi^r)\}d\omega \qquad (II.39)$$

where F is the Fresnel function of a complex argument, discussed in Appendix A, and $\xi^{i,r}$ are complex valued and again given by (II.36) with Ω replaced by ω. We make use of (II.39) in Chapter IV.

C. Uniform Asymptotic Theory of Diffraction (UAT)

Except for a few canonical geometries commonly found in textbooks, closed-form solutions for Maxwell's equations are not known. Several asymptotic or high frequency techniques have therefore been devised that enable one to study the scattering process locally, thereby making good use of the canonical solutions. One of these high frequency theories, the Uniform Asymptotic Theory of Diffraction (UAT), proposed by Ahlawalia, Lewis and Boersma [1], is based on the form of the scattered field in Equation (II.34). The UAT is one, and the most successful, of several high frequency or asymptotic theories that attempt to overcome the singularity of the diffracted field as formulated by the GTD [7]. For the canonical problem of an incident plane wave on a half-plane (Figure 7), all asymptotic solutions reduce to the one in (II.34). But for a more complex situation, such as a line source field incident

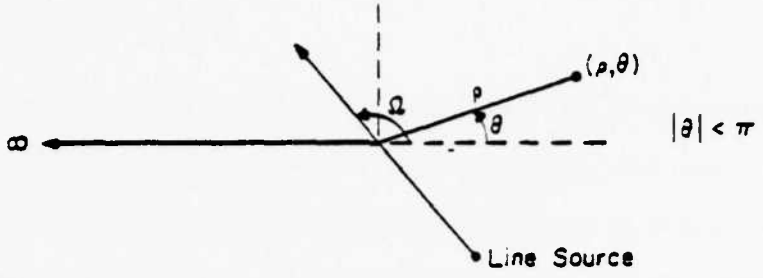

Figure 7. Diffraction of a line source field by a half-plane.

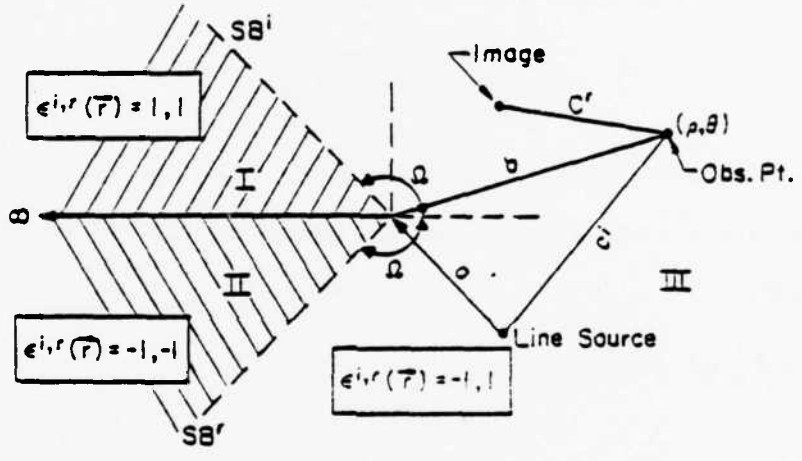

Figure 8. Shadow Indicator. SB^i and SB^r are the shadow boundaries.

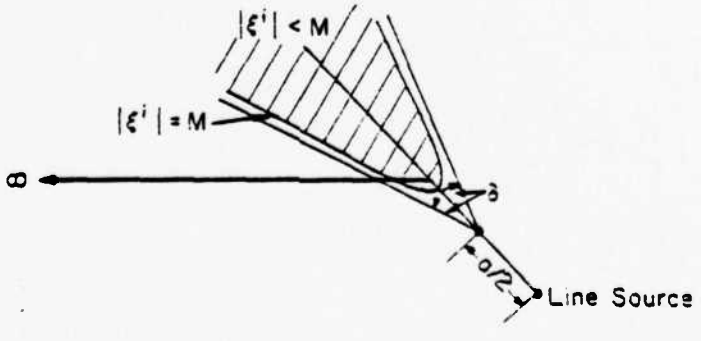

Figure 9. Line of constant detour defined in (II.52).

on a half-plane, it has been shown [7] that the UAT, which provides a systematic way for obtaining the higher-order terms in the asymptotic expansion, gives these terms accurately, whereas the other methods do not. Furthermore, the UAT has been successfully applied to problems with a patterned incident field and for more complicated geometries of the scatterer [12], [26].

The Uniform Asymptotic Theory requires that the incident field be a ray field, that is, $\phi^i(r)$ can be expressed as

$$\phi^i(\vec{r}) = e^{iks(\vec{r})}[\vec{A}(\vec{r}) + \sum_{n=1}^{\infty} (ik)^{-n}\vec{A}_n(\vec{r})] \qquad \text{(II.40)}$$

where s(r) is the eikonal and the A's are amplitude vectors. Neglecting in (II.40) the k^{-1} and higher terms and requiring that ϕ^i satisfy Helmholtz's equation,

$$(\nabla^2 + k^2)\phi^i = 0 \quad , \qquad \text{(II.41)}$$

we have

$$k^2(1 - (\nabla s)^2)\vec{A} + ik(\vec{A}\nabla^2 s + 2\nabla s \cdot \nabla\vec{A}) + \nabla\vec{A} = 0 \quad . \qquad \text{(II.42)}$$

From Equation (II.42), the following conditions are derived:

$$|\nabla s|^2 = 1 \qquad \text{(II.43a)}$$

$$2\nabla s \cdot \nabla\vec{A} + (\nabla^2 s)\vec{A} = 0 \quad , \qquad \text{(II.43b)}$$

and from Gauss' Law

$$\nabla s \cdot \vec{A} = 0 \quad . \qquad \text{(II.43c)}$$

Also from (II.42), we must have

$$\nabla \vec{A} = 0 \tag{II.44}$$

or very close to it. This last condition obviously does not hold at a caustic or at other points where the field variation is great.

If the incident field is indeed a ray field and satisfies the previous conditions, then the solution to the scattering problem shown in Figure 7 is given by UAT as

$$\phi^t(\vec{r}) = \phi^G + \phi^d + O(k^{-3/2}) \tag{II.45}$$

where $\phi^d(r)$ is called the diffracted field and is given by

$$\phi^d(\vec{r}) = \phi^i(\vec{r} = 0) D(\Omega, \theta)\, g(kr) \tag{II.46}$$

where

$$g(kr) = \frac{e^{ik(r+\pi/4)}}{\sqrt{8\pi kr}} \tag{II.47}$$

$$\text{and } D = \frac{4 \cos\left(\frac{1}{2}\Omega\right) \sin\left(\frac{1}{2}\theta\right)}{\cos \Omega - \cos \theta} \quad \text{for H waves}$$

$$= \frac{4 \sin\left(\frac{1}{2}\Omega\right) \cos\left(\frac{1}{2}\theta\right)}{\cos \Omega - \cos \theta} \quad \text{for E waves} \quad . \tag{II.48}$$

The angles are illustrated in Figure 7. Note that at the lines $\theta = \pm \Omega$ the diffraction coefficient D becomes infinite and the diffracted field diverges. These lines are called the incident and reflected shadow boundaries.

The first term in (II.45), $\phi^G(r)$, which represents a modification of the geometrical optics field, is given by

$$\phi^G(\vec{r}) = [F(\xi^i) - \hat{F}(\xi^i)]\phi^i(\vec{r}) + [F(\xi^r) - \hat{F}(\xi^r)]\phi^r(\vec{r}) \quad . \tag{II.49}$$

For large ξ, the Fresnel function has an asymptotic expansion given by

$$F(\xi) = \Theta(-\xi) + \hat{F}(\xi) + O(\xi^{-3}) \quad |\xi| \to \infty \tag{II.50}$$

where $\Theta(x)$ is the unit step function, $\phi^r(r)$ is the field radiated in free space by the image source of $\phi^i(r)$, and

$$\hat{F}(\xi) = \frac{1}{2\xi\sqrt{\pi}} e^{i(\xi^2+\pi/4)} \quad . \tag{II.51}$$

The term $\xi^{i,r}$ is called the detour parameter of the incident (reflected) field and is a measure of the phase difference between the incident (reflected) and diffracted fields. Specifically (refer to Figure 8),

$$\xi^{i,r}(\vec{r}) = \varepsilon^{i,r} \left|\sqrt{k(a + b - c^{i,r})}\right| \tag{II.52}$$

where $\xi^{i,r}(r)$ is the "shadow indicator" and is defined as

$$\varepsilon^{i,r}(\vec{r}) = \begin{cases} +1 \text{ if } \vec{r} \text{ is in the geometrical shadow of } \phi^{i,r} \\ -1 \text{ if } \vec{r} \text{ is in the geometrical lit region of } \phi^{i,r} \end{cases} . \tag{II.53}$$

Observe that:

(a) If $\xi^{i,r}$ is large, that is, if we are away from the shadow boundaries, ϕ^G reduces to ϕ^g, the geometrical optics field. The total field is then given by

$$\phi^t(\vec{r}) = \phi^g(\vec{r}) + \phi^d(\vec{r}) \quad . \tag{II.54}$$

This form of the solution is known as the GTD (Geometrical Theory of Diffraction) field.

(b) If we are on the shadow boundaries, $\xi^{i,r}$ becomes zero and $\hat{F}(\xi^{i,r})$ diverges. However, recall that on the shadow boundaries the diffraction coefficient diverges as well. It is easy to show that the singularities of $\hat{F}(\xi^{i,r})$ and $D(\Omega,\theta)$ cancel, making the total field well-behaved. It is in this sense that the UAT is "uniform."

To find the region in space where ϕ^G approaches ϕ^g, we seek to find the locus of points such that

$$|\xi^{i,r}| = M \tag{II.55}$$

where M is some constant large enough so that the $O(\xi^{-3})$ term in Equation (II.50) can be ignored. The locus of points satisfying (II.55) is obviously a hyperbola with one focus at the source (image) and the other at the edge. The asymptotes of the hyperbola form an angle 2δ, where (see Figure 9)

$$\delta = 4 \sin^{-1}\sqrt{(M/\ 2ka)} \quad . \tag{II.56}$$

For M = 2, the difference between ϕ^G and ϕ^g is approximately 2%. For M = 1, it is approximately 10%. Note that for small M, that is, in the "transition region," the field in (II.45) is not a ray field.

Finally, we note in connection with the UAT that if the line source in Figure 7 gives rise to a patterned field, or if higher-order terms are desired, (II.40) through (II.44) provide the machinery for doing so.

III. SOLUTIONS OF CANONICAL PROBLEMS

In order to gain insight into our study of coupling into a parallel plate guide with an arbitrary stagger "ℓ" (Figure 1), the case of the unstaggered waveguide ($\ell = 0$) is examined in some detail. This canonical problem, which has an exact closed-form solution, also provides the necessary test for evaluation of the different staggered waveguide solutions presented in Chapter IV.

Because of the symmetry of the unstaggered guide, we can introduce an electric or magnetic wall halfway through the guide and study the corresponding cases in Figures 10a and 10b. The solutions to the scattering by the two guides in Figures 10a and 10b now correspond to the symmetrical and asymmetrical components of the total scattered field. We, therefore, speak interchangeably of the canonical case as being a guide of zero stagger or one where the stagger ℓ is infinite, the latter case sometimes allowing an easier interpretation of the results and a more natural extension to the case where "ℓ" is finite.

There are, essentially, two approaches to solving the staggered, or equivalently, the infinite staggered case. The first is to apply some function theoretic technique and derive the modal coefficients in the guide with the interactions between the plates accounted for in toto. This approach, using the Wiener-Hopf Method, is illustrated in Sections A and B wherein the "ray-to-mode" conversion formulas and the "modified diffraction coefficient" are presented. In Section C, we look at a ray technique the YKF Method [30], which tries to track the individual interactions between the plates, and present this method's "ray-to-mode" conversion

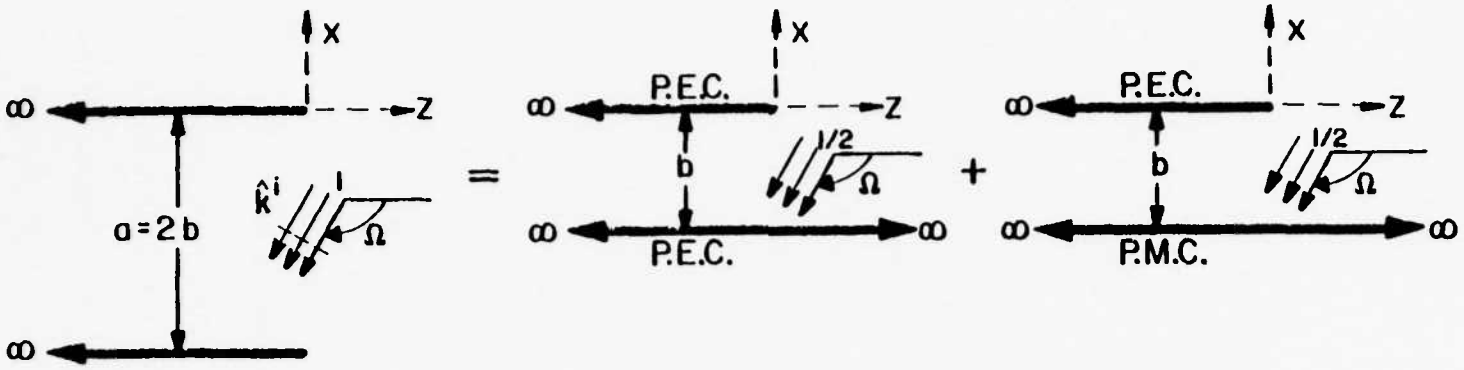

Figures 10a and 10b. Equivalent antisymmetrical and symmetrical problems for an unstaggered guide.

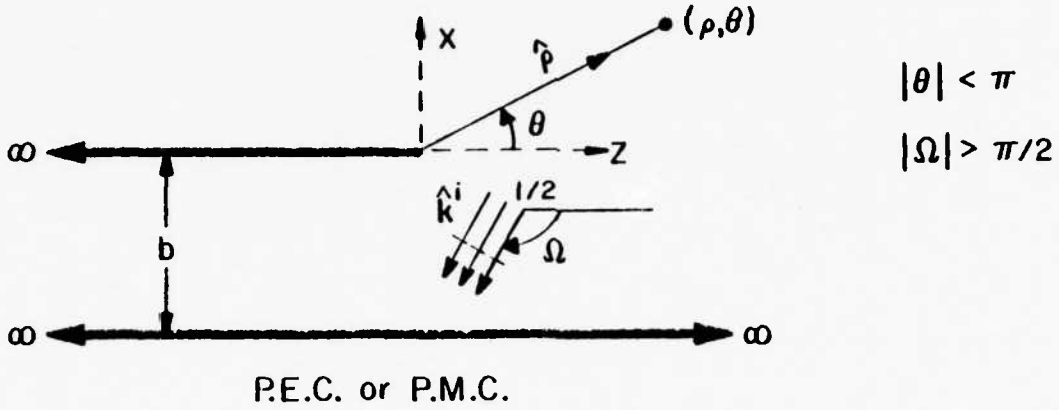

Figure 11. Diffraction of a plane wave by an infinitely staggered guide.

formula. In Section D the different techniques and "ray-to-mode" conversion formulas are discussed with an eye to their possible application in the finite stagger problem.

A. Wiener-Hopf Solution: Unstaggered Guide

The geometry of the guide in question is shown in Figure 11. We examine in some detail the case where the incident field is a plane E-wave. The solution for the H-wave can be found in a manner similar to that of the E-wave and only the final results are given.

First, we make use of the symmetry of the guide and solve the symmetrical and asymmetrical problems separately. For the geometries in Figures 10a and 10b, it is convenient to define the incident field in such a way that the reflection off the electric or magnetic wall is included in the incident field. With this in mind, the incident field is written as

$$\phi^i(x,z) = \frac{1}{2} e^{ikz\cos\Omega}\{e^{ikx\sin\Omega} \mp e^{-ik(x+a)\sin\Omega}\}, \qquad \text{(III.1)}$$

-, + for the electric and magnetic wall, respectively. The scattered field is now defined as

$$\phi^s(\rho,\theta) = \phi^t(\rho,\theta) - \phi^i(\rho,\theta) \quad ; \qquad \text{(III.2)}$$

ρ and θ are shown in Figure 11.

The Wiener-Hopf formulation varies slightly depending on whether $|\Omega| < \pi/2$ or $|\Omega| > \pi/2$. In the application of the Wiener-Hopf technique, it is desirable to have ϕ^s attenuate as $z \to \infty$. From the definition of the scattered field in (III.2), the scattered field will not attenuate in the shadow region if $|\Omega| < \pi/2$. We therefore restrict $|\Omega| > \pi/2$. This constraint can later be removed.

For $|\Omega| > \pi/2$, ϕ^s satisfies Helmholtz's equation

$$\partial_x^2\phi^s + \partial_z^2\phi^s + k^2\phi^s = 0 \qquad \text{(III.3)}$$

where $k = k_1 + ik_2$, $k_1 >> k_2$. Introducing the Fourier Transform

$$\phi^s(x,\alpha) = \frac{1}{\sqrt{2\pi}} \int_{-\infty}^{\infty} \phi^s(x,z)e^{i\alpha z}\, dz \qquad \text{(III.4)}$$

where $\alpha = \sigma + i\tau$ and $\phi^s(x,\alpha)$ is analytic in the region $-k_2 \cos\Omega > \tau > -k_2$, we get

$$\partial_x^2\phi^s(x,\alpha) - \gamma^2\phi^s(x,\alpha) = 0 \qquad \text{(III.5)}$$

where $\gamma = [\alpha^2 - k^2]^{1/2}$ is defined on the upper sheet, shown in Figure 3.

The solution (III.5) satisfying the radiation condition can formally be written as

$$\phi^s(x,\alpha) = \begin{cases} A(\alpha)e^{-\gamma x} & x > 0 \\ B(\alpha)e^{-\gamma x} + C(\alpha)e^{\gamma x} & -b < x < 0 \end{cases} . \qquad \text{(III.6)}$$

From the continuity of $\phi^s(x,\alpha)$ across a PEC (Perfect Electric Conductor) at $x = 0$, one obtains

$$A(\alpha) = B(\alpha) + C(\alpha) \quad . \qquad \text{(III.7)}$$

If the bottom wall is a PEC as well,

$$B(\alpha) = -C(\alpha)e^{-2\gamma b} \quad , \qquad \text{(III.8)}$$

and if a PMC (Perfect Magnetic Conductor) wall

$$B(\alpha) = C(\alpha)e^{-2\gamma b} \qquad \text{(III.8b)}$$

If $J_-(\alpha)$ is defined as

$$J_-(\alpha) = \frac{1}{2}\{\partial_x\phi^s(0^+,\alpha) - \partial_x\phi^s(0^-,\alpha)\} = -\gamma(A - B + C) \quad , \tag{III.9}$$

then from (III.7), (III.8a) and (III.8b) the relationship

$$J_-(\alpha) = \frac{-\gamma}{(1 \mp e^{-2\gamma b})} A(\alpha), \quad \begin{bmatrix} - \\ + \end{bmatrix} = \begin{bmatrix} \text{PEC wall} \\ \text{PMC wall} \end{bmatrix} \quad , \tag{III.10}$$

is obtained. If the boundary condition is applied at $x = 0$, the Wiener-Hopf Equation

$$-\phi^i_-(0,\alpha) + \phi^s_+(0,\alpha) = \frac{-G(\alpha)}{\gamma} J_-(\alpha), \quad -k_2\cos\Omega > \tau > -k_2 \tag{III.11}$$

is constructed, where

$$G(\alpha) = \begin{cases} 1 - e^{-2\gamma b} & \begin{bmatrix} \text{PEC wall} \end{bmatrix} \\ 1 + e^{-2\gamma b} \equiv \tilde{G}(\alpha), & \begin{bmatrix} \text{PMC wall} \end{bmatrix} \end{cases} \tag{III.12}$$

and

$$\phi^i_-(0,\alpha) = \frac{-i(1 \mp e^{-2ikb\sin\Omega})}{2\sqrt{2\pi}\ (\alpha + k\cos\ \Omega)} \qquad t < -k_2\cos\Omega \quad . \tag{III.13}$$

As discussed in Section A, Chapter II, the next step in the Wiener-Hopf process is the factorization of $G(\alpha)/\gamma$. The factorization of γ is obvious, and from Equation (II.4), $G(\alpha)$ factors into $G_+(\alpha)G_-(\alpha)$, where

(a) For $G(\alpha) = 1 - e^{-2\gamma b}$, (PEC wall)

$$G_+(\alpha) = [2b\ \mathrm{sinc}(kb)]^{1/2}\ (\alpha + k)^{1/2}\ e^{-i\pi/4}\ \exp[\frac{i\alpha b}{\pi}(1 - C + \ln\frac{2\pi}{kb} + \frac{i\pi}{2})]$$

$$\exp[\frac{ib}{\pi}\ln(\frac{\alpha - \gamma}{k})]\ \prod_{n=1}^{\infty}\ (1 + \frac{\alpha}{i\gamma_n})\ e^{i\alpha b/n\pi}, \quad \tau > -k_2, \tag{III.14a}$$

(b) For $G(\alpha) = 1 + e^{-2\gamma b} \equiv \tilde{G}(\alpha)$, (PMC wall)

$$\tilde{G}_+(\alpha) = [2\cos(kb)]^{1/2} \exp\left[\frac{i\alpha b}{\pi}\left(1 - C + \ln\left(\frac{\pi}{2kb}\right) + \frac{i\pi}{2}\right)\right]$$

$$\exp\left[\frac{ib\gamma}{\pi}\ln\left(\frac{\alpha - \gamma}{k}\right)\right] \prod_{n=1}^{\infty}\left(1 + \frac{\alpha}{i\gamma_{n-1/2}}\right) e^{i\alpha b/(n-1/2)\pi}, \quad t > -k_2 \tag{III.14b}$$

(c) $$G_-(\alpha) = G_+(-\alpha) \quad . \tag{III.14c}$$

In the above equations C is the Euler's Constant and $i\gamma_n$, $i\gamma_{n-1/2}$ are the zeroes of $(1 - e^{-2\gamma b})$ and $(1 + e^{-2\gamma b})$, respectively, with γ_n given by

$$\gamma_n = \left[\left(\frac{n\pi}{b}\right)^2 - k^2\right]^{1/2} \tag{III.15}$$

with the same branch cuts as in Figure 3. A set of tables and other forms for $G_+(\alpha)$ are presented in Appendix B.

Now decomposing Equation (III.11) and using the edge condition, the scattered field in the transform domain for $-b < x < 0$ is

$$\phi^s(x,\alpha) = \frac{(1 \mp e^{-2ikb\sin\Omega})}{2} \frac{X(k\cos\Omega,\alpha)}{\sqrt{2\pi}} \frac{e^{\gamma x}}{2\gamma}\left\{\frac{1}{G_+(-k\cos\Omega)G_+(-\alpha)}\right\}$$

$$\mp \frac{(1 \mp e^{-2ikb\sin\Omega})}{2} \frac{X(k\cos\Omega,\alpha)}{\sqrt{2\pi}} \frac{e^{-\gamma(x+2b)}}{2\gamma}\left\{\frac{1}{G_+(-k\cos\Omega)G_+(-\alpha)}\right\},$$

$$\begin{pmatrix}-\\+\end{pmatrix} = \begin{matrix}\text{PEC wall}\\\text{PMC wall}\end{matrix} \tag{III.16}$$

where $X(k\cos\Omega,\alpha)$ is the spectral diffraction coefficient defined in (II.26). Comparing Equations (III.16) and (II.27), it is apparent that the spectral representation of the scattered field has the same form as that for the isolated half-plane and its image, but the half-plane solutions are multiplied by the factor in the curly brackets, which accounts for the multiple interactions between the top plate and the PEC or PMC wall. We should note that as

$b \to \infty$, $G_+(\alpha) \to 1$ and, since $\mathrm{Re}(\gamma) > 0$, the reflection term on the right-hand side of (III.16) goes to zero, so that only the half-plane solution remains.

To find the field in the guide, the inverse Fourier Transform of (III.16) is computed. Since the guide is in the region $z < 0$, the integration path may be closed as shown in Figure 12 and the residues evaluated.

In computing these residues one finds that, first, the contribution around the branch cut is zero. Next, the residue at $\alpha = -k \cos \Omega$ gives the negative incident field so that the total field in the guide is fully expressible in terms of its modes, as it must be. Lastly, the poles at $\alpha = i\gamma_n$ give the modes of the guide. Note that $\alpha = i\gamma_0$ gives the TEM mode.

Summarizing the final results, if the field of the guide in Figure 10 is written as

$$\phi^t(x,z) = \sum_{n=0}^{\infty} C_n \sin\left(\frac{n\pi}{a} x\right) e^{-ik_g z} \qquad n = 1,2, \tag{III.17a}$$

where

$$k_g = \left[k_0^2 - \left(\frac{n\pi}{a}\right)^2\right]^{1/2} \quad , \tag{III.17bb}$$

then the modal coefficient C_n is given by

$$C_n = \frac{(1 + e^{i(n+1)\pi} e^{-ika\sin\Omega})}{2ka \cos \phi_n} D(\Omega, \phi_n - \pi) \left\{\frac{G_+(k \cos \phi_n)}{G_+(-k \cos \Omega)}\right\} \tag{III.18}$$

with n even coinciding with the asymmetrical, PEC wall problem in Figure 10a and n odd, $G_+ \equiv \tilde{G}_+$, with the PMC wall problem. $D(\Omega, \phi_n - \pi)$ is the diffraction coefficient given in Equation (II.48) and ϕ_n is defined by

$$\sin \phi_n = \frac{n\pi}{ka} \quad . \tag{III.19}$$

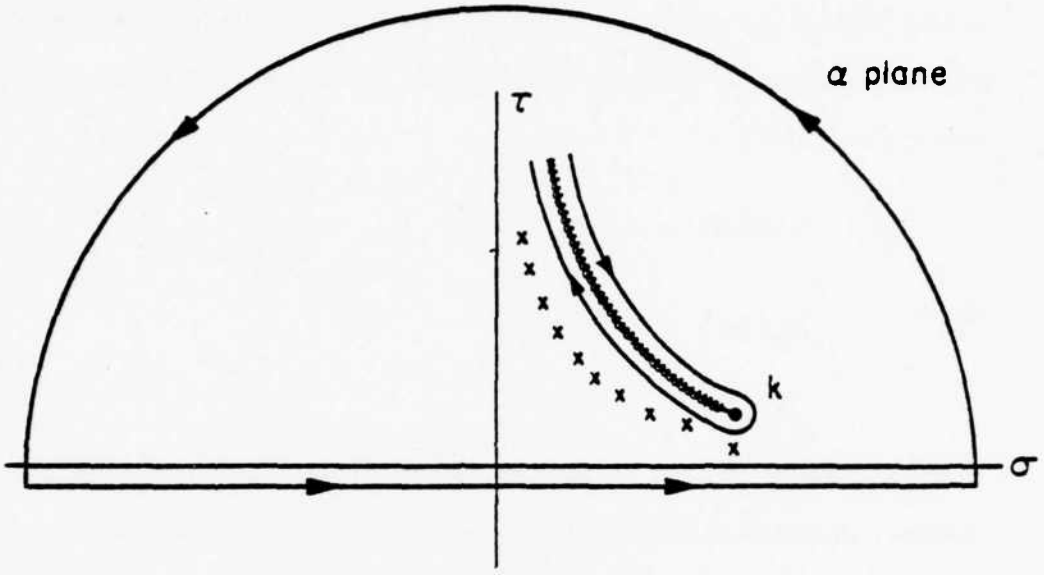

Figure 12. Integration path for the inverse Fourier transform of (III.16), $z < 0$.

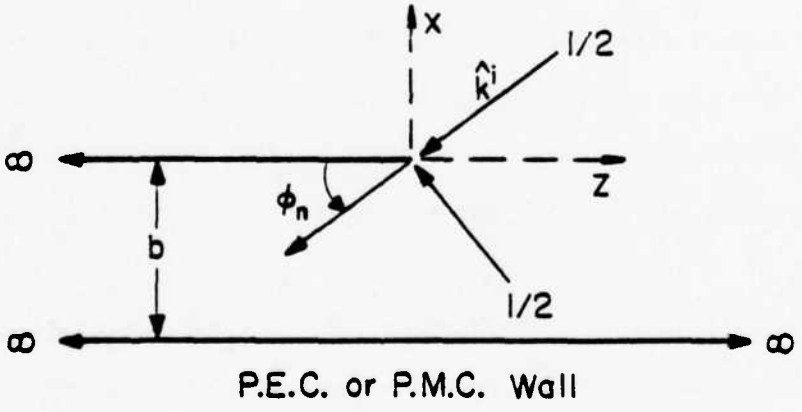

Figure 13. Ray interpretation of the modal coefficient in (III.18).

For $(n\pi/ka) < 1$, that is, for propagating modes we can interpret (III.18) to be the amplitude of the edge diffracted ray in the modal direction of the guide, Figure 13, where $2ka \cos \phi_n$ term serves as a normalization factor. However, instead of just the diffraction coefficient, the "modified diffraction coefficient" [19]

$$\bar{D}(\Omega,\theta) = D(\Omega,\theta) f(\hat{\rho} \cdot \hat{n}) f(-\hat{k}^i \cdot \hat{n}) \tag{III.20a}$$

where

$$f(x) = \begin{cases} G_+(|x|) & x < 0 \\ 1/G_+(x) & x > 0 \end{cases} \tag{III.20b}$$

(see Figure 14) is used to account for the interactions between the plates. Although a ray picture is not totally proper, we say that the nature of this interaction is the reflection-diffraction cycle that takes place along the aperture, as shown in Figure 15. This interpretation is not strictly valid, because after the first reflection off the top plate, the field about the aperture is no longer a ray field and the reflection-diffraction phenomenon cannot really be localized to a point.

To summarize we note that (III.18) is finite even when $D(\Omega, \phi_n - \pi)$ becomes unbounded and also that the derivative of C_n with respect to a is discontinuous at the mode's cutoff point. For an H-wave, the same considerations are used but the diffraction coefficient is that for the H wave.

B. Modified Diffraction Coefficient (MDC): Large Finite Stagger

Having examined in the previous section the unstaggered case, a similar Wiener-Hopf formulation is possible for the finite stagger in Figure 1. This time, however, there is a need to consider an additional unknown, the current on the bottom plate. This in turn leads to a set of coupled Wiener-Hopf equations for the two plate currents which, in general, are not

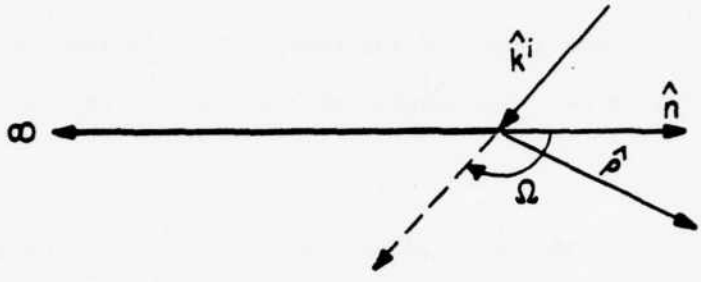

Figure 14. Vectors in the definition of the Modified Diffraction Coefficient.

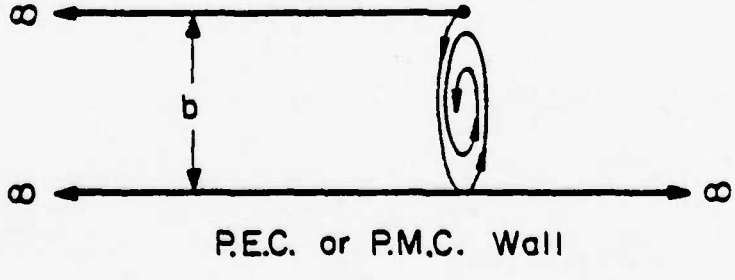

Figure 15. Reflection-diffraction cycle on the guide aperture.

amenable to a solution. But if the diagonal distance "d" is large with respect to the wavelength, asymptotic methods may be employed to decouple the Wiener-Hopf equations, and an approximate solution for the modal coefficients can be obtained. A short presentation leading to the Wiener-Hopf equations is now given and the asymptotic solution for the modal coefficients presented. The details of this section can be found in [19].

We consider again the incident field to be a plane E-wave given by

$$\phi^i(\rho,\theta) = e^{ik\rho\cos(\Omega-\theta)} \quad , \tag{III.21}$$

with the same restriction - $|\Omega| > \pi/2$.

The scattered field is defined as in (III.21), and with the Fourier transform given in (III.4) one again arrives at

$$\partial_x^2\Phi^s(x,\alpha) - \gamma^2\Phi^s(x,\alpha) = 0 \quad . \tag{III.22}$$

The solution to (III.22) is

$$\Phi^s(x,\alpha) = \begin{cases} A(\alpha)e^{-\gamma x} & x > 0 \\ B(\alpha)e^{-\gamma x} + C(\alpha)e^{\gamma x} & -a < x < 0 \\ D(\alpha)e^{+\gamma x} & x < -a \end{cases} \quad . \tag{III.23}$$

Continuity of the E field gives

$$A(\alpha) = B(\alpha) + C(\alpha) \tag{III.24}$$

and

$$B(\alpha)e^{\gamma a} + C(\alpha)e^{-\gamma a} = D(\alpha)e^{-\gamma a} \tag{III.25}$$

The top plate current is again defined as

$$J^T(\alpha) = J_-^T(\alpha) = \frac{1}{2}[\partial_x \phi^s(0^+,\alpha) - \partial_x \phi_-^s(0^-,\alpha)] = \frac{-\gamma}{2}(A - B + C) \quad , \qquad \text{(III.26)}$$

where the superscripts T and B indicate the top and bottom plates, respectively.

Introducing a shifted Fourier transform

$$\tilde{\phi}^s(x,\alpha) = e^{-i\alpha\ell}\, \phi^s(x,\alpha) \quad , \qquad \text{(III.27)}$$

we observe that

$$\tilde{\phi}_-^s(x,\alpha) = \frac{1}{\sqrt{2\pi}} \int_{-\infty}^{\ell} \phi^s(x,\alpha) e^{i\alpha(z-\ell)} dz \qquad \text{(III.28)}$$

is analytic in the region $\tau < -k_2 \cos \Omega$. Then making use of (III.28), the bottom plate current

$$J^B(\alpha) = \frac{1}{2}[\partial_x \phi^s(-a^+,\alpha) - \partial_x \phi^s(-a^-,\alpha)] \qquad \text{(III.29)}$$

can be written as

$$J^B(\alpha) = e^{+i\alpha\ell} \tilde{J}_-^B(\alpha) = -\frac{\gamma}{2}[Be^{\gamma a} - Ce^{-\gamma a} + De^{-\gamma a}] \qquad \text{(III.30)}$$

where $\tilde{J}_-^B(\alpha)$ is analytic in the lower half-plane given by $\tau < -k_2 \cos \Omega$.

Two additional equations are obtained by applying the boundary condition to the top and bottom plates:

$$-\phi_-^i(0,\alpha) + \phi_+^s(0,\alpha) = A(\alpha) \qquad \text{(III.31)}$$

and

$$e^{i\alpha\ell}[-\tilde{\phi}_-^i(-a,\alpha) + \tilde{\phi}_+^s(-a,\alpha)] = D(\alpha)e^{-\gamma a} \quad . \qquad \text{(III.32)}$$

After some manipulation and use of the edge condition, the coupled Wiener-Hopf equations

$$\phi_+^s(0,\alpha) + \frac{1}{\gamma}[J_-^T(\alpha) + e^{-\gamma a}\, e^{i\alpha\ell}\tilde{J}_-^B(\alpha)] - \phi_-^i(0,\alpha) = 0 \qquad \text{(III.33a)}$$

and $$-k_2 \cos\Omega > \tau > -k_2 \, .$$

$$e^{i\alpha\ell}\tilde{\phi}_+^s(-a,\alpha) + \frac{1}{\gamma}[e^{-\gamma a}J_-^T(\alpha) + e^{i\alpha\ell}\tilde{J}_-^B(\alpha)] - e^{i\alpha\ell}\tilde{\phi}_-^i(-a,\alpha) = 0 \qquad \text{(III.33b)}$$

are obtained. It is obvious now that for an arbitrary stagger ℓ the Wiener-Hopf procedure becomes intractable. However, as stated before, an asymptotic evaluation of Equation (III.33) can be made and the field in the waveguide computed to O(1/kd). The details, which can be found in Lee [19], are quite involved and only the final result is now given.

If the field in the guide is given by

$$\phi^t(x,z) = \sum_{n=1}^{\infty} C_n \sin\left(\frac{n\pi}{a}x\right) e^{-ik_g z} \quad , \quad n = 1,2,3 \ldots \qquad \text{(III.34)}$$

$$k_g = [k_0^2 - \left(\frac{n\pi}{a}\right)^2]^{1/2} \quad , \qquad \text{(III.35)}$$

then, with H(A) defined as

$$H(A) = \begin{cases} 1 \text{ if A is true} \\ 0 \text{ if A is false} \end{cases} \qquad \text{(III.36)}$$

the asymptotic solution for C_n for the propagating modes is

$$C_n = \sum_{j=1}^{4} c_n^{(j)} + O(1/kd) \qquad \text{(III.37)}$$

where

$$c_n^{(1)} = \frac{[H(\Omega < -\delta) - e^{-2ika\sin\Omega}\, H(\Omega > \delta - \pi)]}{2ka\cos\phi_n}\left[D(\Omega,\phi_n - \pi)\left\{\frac{G_+(k\cos\phi_n)}{G_+(-k\cos\Omega)}\right\}\right] \tag{III.38a}$$

$$c_n^{(2)} = [H(\phi_n < \delta)e^{ika\cos(\Omega+\delta)}][D(\Omega,\pi - \phi_n)]\left\{\frac{(-1)^n e^{ik\ell\cos\phi_n}}{2ka\cos\phi_n}\right\} \tag{III.38b}$$

$$c_n^{(3)} = \frac{[e^{ika\cos(\Omega+\delta)}g(kd)D(\Omega,\pi - \delta)]}{2ka\cos\phi_n}\left[D(-\delta,\phi_n - \pi)\left\{\frac{G_+(k\cos\phi_n)}{G_+(k\cos\delta)}\right\}\right] \tag{III.38c}$$

and

$$c_n^{(4)} = H(\phi_n < \delta)[H(\Omega < -\delta) - e^{-2ika\sin\Omega}\, H(\Omega > \delta - \pi)][g(kd)D(\Omega,\ \delta - \pi)]$$
$$[D(\pi - \delta,\ \pi - \phi_n)]\left\{\frac{1}{G_+(-k\cos\Omega)G_+(k\cos\delta)}\right\}\left\{\frac{(-1)^n e^{-ik\ell\cos\phi_n}}{2ka\cos\phi_n}\right\} \tag{III.38d}$$

The angle ϕ_n is defined as in Section A and is given by

$$\sin\phi_n = \frac{n\pi}{ka} \quad . \tag{III.39}$$

For propagating modes the four numbers $c_n^{(1)}$ thru $c_n^{(4)}$ can be given the interpretation of different diffracted rays "coupling" into the guide. Consider, for example, $c_n^{(1)}$. We see that $c_n^{(1)}$ is the amplitude of the top edge diffracted ray in the modal direction - the same interpretation that was given in Section A. The functions $H(\cdot)$ in the equation for $c_n^{(1)}$ are present so that a ray "couples" into the guide via the edge diffraction only if that ray hits the edge. The situation is illustrated in Figure 16. We note the presence in (III.38) of the "Modified Diffraction Coefficient," which as in Section A, is said to account for the interaction between the

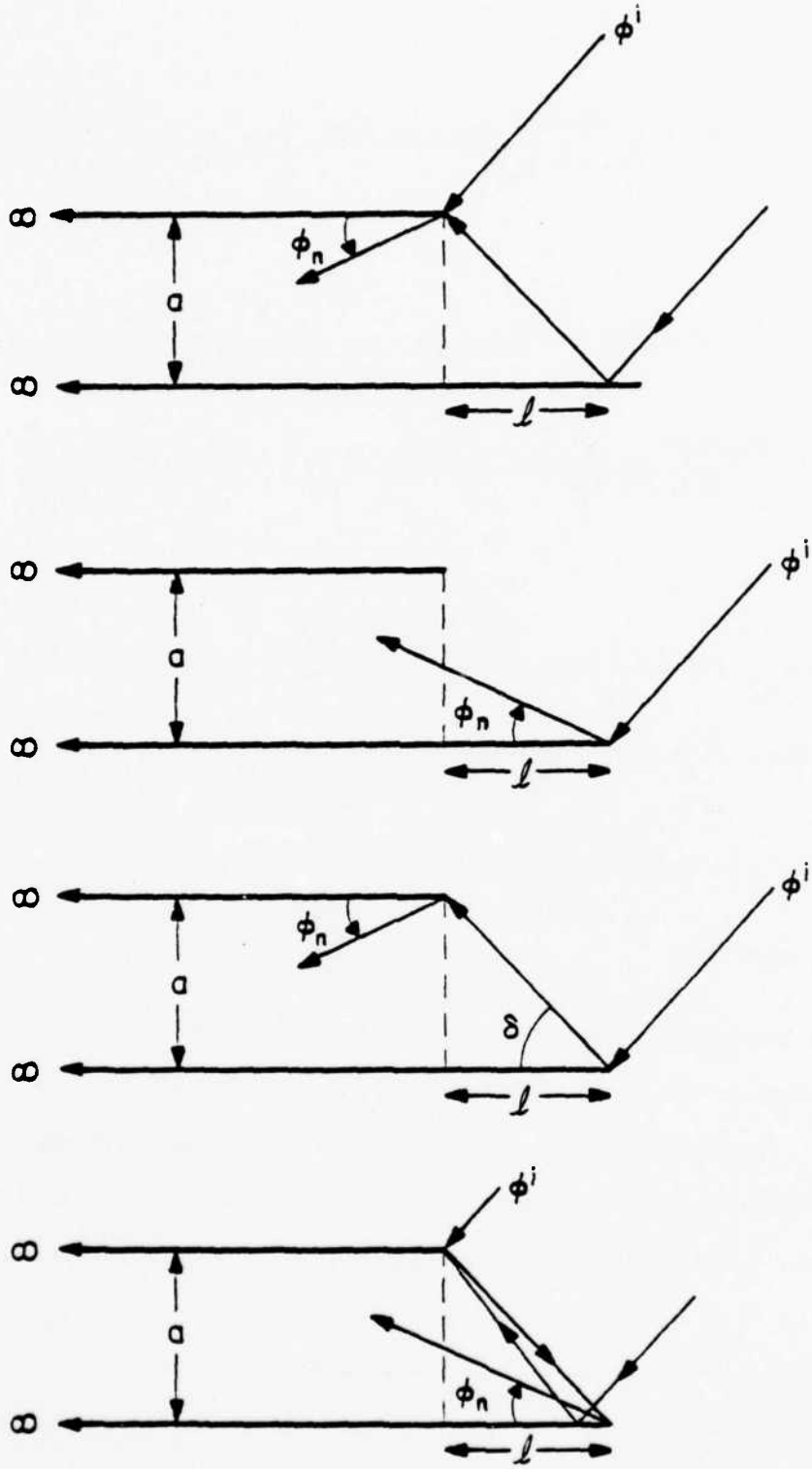

Figure 16. Various rays in the asymptotic problem.

plates along the guide aperture. The interpretation of $c_n^{(2)}$ is similar, but with an extra phase factor, $e^{ik\ell\cos\phi_n}$, present. The diffraction coefficient is now unmodified, as the bottom plate's edge is not on the aperture. The terms $c_n^{(3)}$ and $c_n^{(4)}$ are due to the twice-diffracted diagonal rays, shown in Figure 16. Higher-order interactions along the diagonal are ignored, as this result is only $0(1/kd)$.

In Sections A and B, we have presented the modal coefficients and have associated them with the edge diffraction rays. But the mechanism by which the diffracted rays couple into the guide and the reason for the absence of the incident field in the final solution are not clear. This and other points are discussed in Section C and D.

C. YKF Method

Though the exact solution of the unstaggered case was given in Section A, a ray optics solution to the problem is nonetheless highly desirable. Not only are we provided with another check of the different asymptotic theories, but the use of ray optics and the local nature of ray methods allow for a better physical understanding of how the energy is actually coupled into the guide. The first published work along this line was by Yee and Felsen [30], and in the ray analysis presented below, we often refer to this paper.

C.1. Formulation via ray optics

We start by considering the field in the presence of the unstaggered guide. For exactness, the incident field is an E-polarized line source field, normalized so that its phase center is at (0,0). That is,

$$\phi^i(\rho_s) = \frac{e^{ik(\rho_s - R)}}{\sqrt{\rho_s/R}} \qquad \text{(III.40)}$$

where ρ_s is the distance from the source, as in Figure 17. The advantage of using a line source in our formulation becomes evident later.

If R is large enough, we have in essence a plane wave. Using Equation (II.45), the total field outside the guide may be written as

$$\phi^t = [F(\xi_1^i) - \hat{F}(\xi_1^i) + F(\xi_2^i) - \hat{F}(\xi_2^i) - 1]\phi^i$$

$$- [F(\xi_1^r) - \hat{F}(\xi_1^r)]\phi_1^r - [F(\xi_2^r) - \hat{F}(\xi_2^r)]\phi_2^r$$

$$+ (\phi_1^d + \phi_1^{int}) + (\phi_2^d + \phi_2^{int}) \quad . \tag{III.41}$$

In the above equation, the subscripts 1 and 2 refer to the plates as given in Figure 17, $\xi_{1,2}^{i,r}$ are the detour parameters, $\phi_{1,2}^d$ are the diffracted fields that would exist if the plates were infinitely far apart, and $\phi_{1,2}^{int}$ are the terms due to the interaction between plates 1 and 2.

We call the GO and diffracted fields, without any interaction, the "primary field." The $-\phi^i$ term in the first bracket in (III.41) is present so that the incident field is not counted twice. We should emphasize that Equation (III.41) is only for the region outside the guide. To find the field inside, the guiding action of the waveguide, that is, the reflections of the field, as schematically indicated in Figure 18, must be considered. Once we have done so, and the far field inside the guide is known, the model coefficients are computed by simply Fourier decomposing the field over the aperture A. That is

$$C_n = \frac{2}{a} \int_{-a}^{a} \phi^t (x,z) \sin(k\sin\phi_n x) e^{ikz\cos\phi_n} dx \tag{III.42}$$

We have illustrated this procedure by first considering the diffracted fields ϕ_1^d and ϕ_2^d.

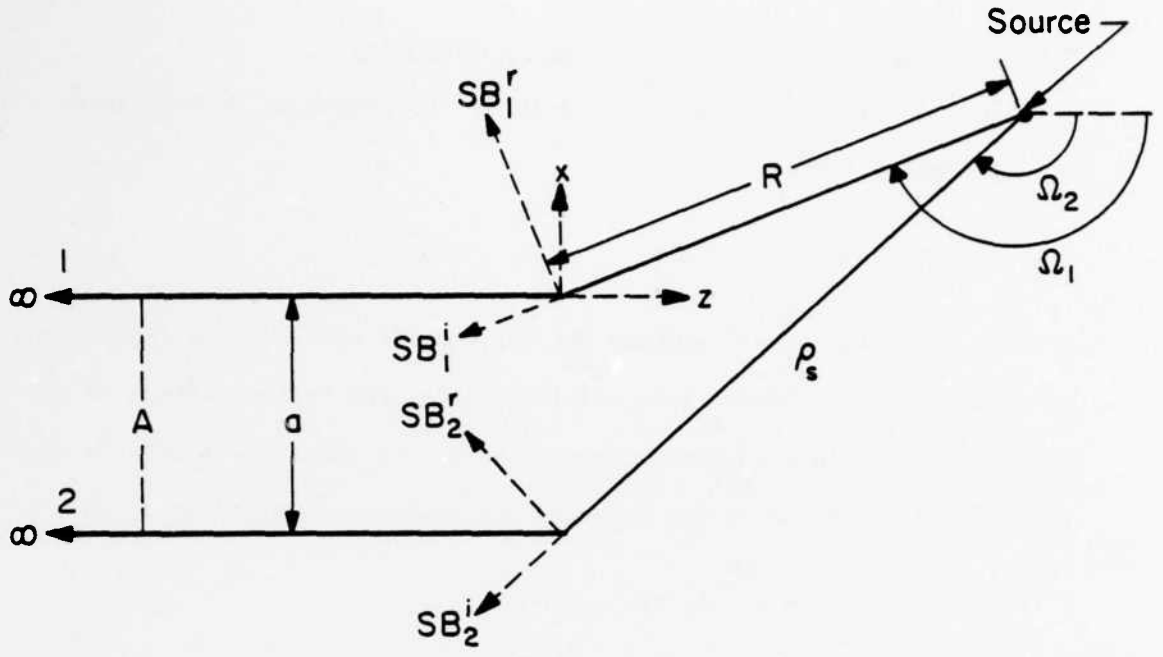

Figure 17. Diffraction of a line source field by an unstaggered parallel-plate guide.

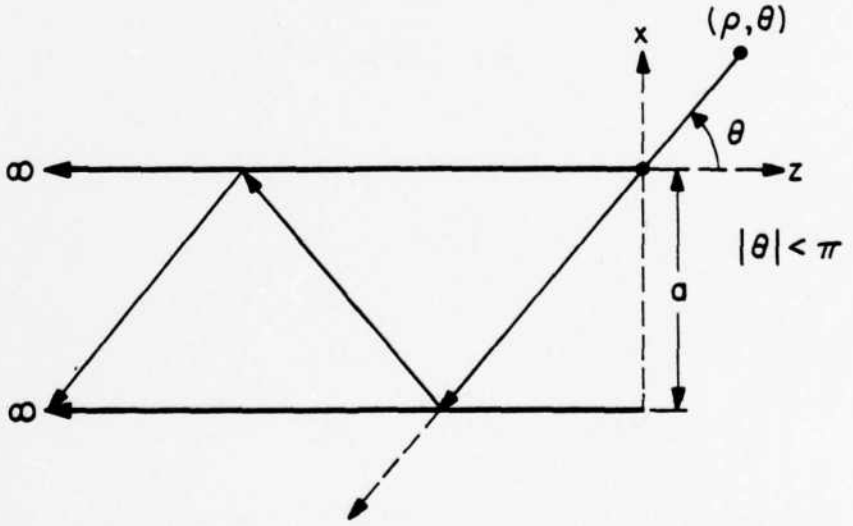

Figure 18. Reflections of a diffracted ray in the guide.

C.2. Primary field: Diffracted field contribution

Consider the line source at x = 0, z = 0, producing in free space the diffracted field

$$\phi_1^d = \phi^i(0,\ 0)D(\Omega,\theta)g(k\rho); \tag{III.43}$$

g and D are defined in Equations (II.47) and (II.48). If one ignores any diffraction by the lower plate and just traces the reflected rays in the guide, the far field in the guide excited by the edge line source is the same as that produced by the infinite set of images located at z = 0,

$$x = 2aj \qquad j = 0, \pm 1, \pm 2 \quad . \tag{III.44}$$

That is, for $z < 0$, $-a < x < 0$, the edge line source gives rise to a far field given by the field of an infinite linear array centered at the edge and spaced 2a apart, (see Figure 19), with the array's field given by

$$\hat{\phi}_1^d = \phi^i(0,0) \sum_{j=-\infty}^{\infty} D(\Omega,\theta_j)g(k\rho_j) \tag{III.45}$$

where

$$\rho_j = [(x - 2aj)^2 + z^2]^{1/2}$$

and

$$\theta_j = \tan^{-1}[(x - 2aj)/z] \quad , \quad |\theta_j| < \pi \ .$$

Note that since $D(\Omega, -\theta_j) = -D(\Omega, \theta_j)$ the array is antisymmetrical. With the modes as given in (III.17), the contribution to the modal coefficient from ϕ_1^d is

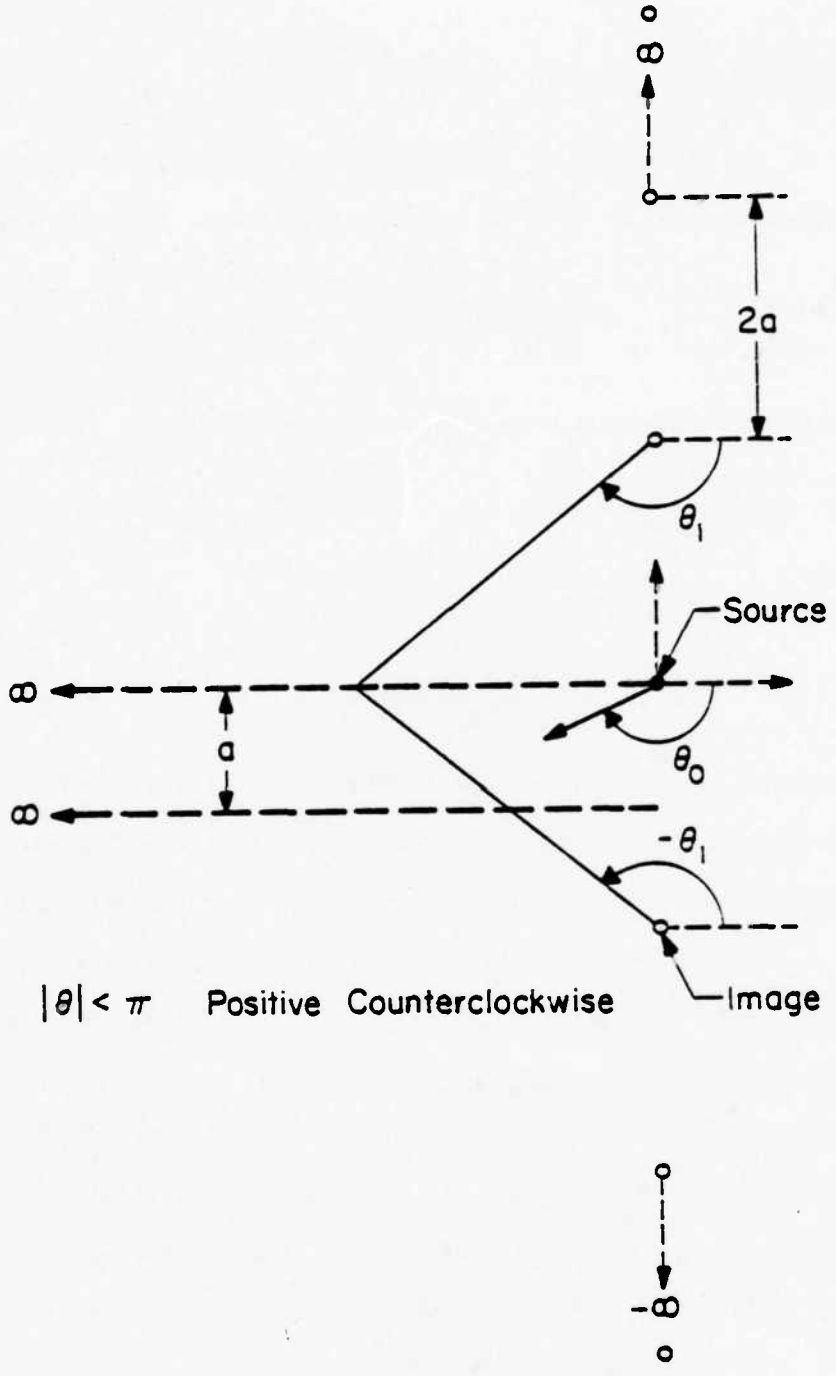

Figure 19. Array of diffraction image sources.

$$c_n^{p'} = \frac{1}{a}\int_{-a}^{a} \hat{\phi}_1^d(x,z)\, \sin(k \sin \phi_n x) e^{ikz\cos\phi_n}\, dx \qquad \text{(III.46)}$$

with $z >> 0$. If the change of variables $t = x - 2aj$ is introduced, the integration-summation in (III.46) becomes an infinite integral and

$$c_n^{p'} = \left(\frac{\phi^i(0,0)e^{i\pi/4}}{a\sqrt{8\pi k}}\right)\int_{-\infty}^{\infty} \frac{D(\Omega,\theta(t))}{\sqrt{\rho(t)}}\, e^{ik\rho(t)}\, \sin(k \sin \phi_n t) e^{ikz\cos\phi_n}\, dt. \qquad \text{(III.47)}$$

If the integral is evaluated asymptotically, we obtain

$$c_n^{p'} \sim \frac{\phi^i(0,0)D(\Omega,\ \phi_n - \pi)}{2ka\cos\phi_n} \quad . \qquad \text{(III.48)}$$

Likewise, for the line source at $x = -a$, we get

$$c_n^{p'} = e^{i(n+1)\pi}\phi^i(0,\ -a)\, \frac{D(\Omega,\ \phi_n - \pi)}{2ka\cos\phi_n} \quad . \qquad \text{(III.49)}$$

Adding (III.49) to (III.48), we see that the part of the modal coefficient due to diffraction is the same as the total, exact modal coefficient in (III.18) except for the factor in (III.18) which accounts for the interaction between the plates. Note that the results derived here are only valid for the propagating modes, whereas (III.18) applies to the evanescent modes as well.

C.3. Primary field: GO field contribution

With the interpretation just given for Equation (III.18), it appears that the geometrical optics field plays no role in the final solution. To see why, we set up the problem as before. First, looking at (III.41) and Figure 17, it is evident that for the region in the waveguide it is sufficient to consider the geometrical optics field given by

$$\phi^G = \tilde{F}(\xi_1^i)\phi^i - \tilde{F}(\xi_2^r)\phi_2^r \quad , \tag{III.50}$$

where, for convenience

$$\tilde{F}(x) \triangleq F(x) - \hat{F}(x) \quad . \tag{III.51}$$

That is, the field is that of two line sources, one with a pattern given by $\tilde{F}(\xi_1^i)$ and the other with a pattern $-\tilde{F}(\xi_2^r)$, where from Figure 20

$$\xi_1^i = \varepsilon_1^i(\theta_0^i)\left|\sqrt{k(a_0^i + b_0^i - c_0^i)}\right| \tag{III.52a}$$

$$\varepsilon_1^i(\theta_0^i) = \begin{cases} +1 & \theta_0^i < \Omega_1 \\ -1 & \theta_0^i > \Omega_1 \end{cases} \tag{III.52b}$$

$$\xi_2^r = \varepsilon_2^r(\theta_0^r)\left|\sqrt{k(a_0^r + b_0^r - c_0^r}\right| \tag{III.52c}$$

$$\varepsilon_2^r(\theta_0^r) = \begin{cases} +1 & \theta_0^r < |\Omega_2| \\ -1 & \theta_0^r > |\Omega_2| \end{cases} \quad . \tag{III.52d}$$

Note that θ_0^i and θ_0^r are of opposite sign.

We first examine the source $\tilde{F}(\xi_1^i)$ and look at its array of images for the field in the waveguide. This is shown in Figure 21. The source is at $z = -R\cos(\Omega_1)$, $x = R\sin(|\Omega_1|)$; the images are located at $z_j = -R\cos(\Omega_1)$, $x_j = \pm R\sin(|\Omega_1|) + 2aj$, $j = \pm 1, \pm 2, \ldots$. Observe that for $x < 0$ the pattern is $-\tilde{F}(\xi_1^i(-\theta_j^i))$ because the bottom images account for an odd number of reflections. This array is allowed to radiate in free space with the detour parameters given by (III.52a) and (III.52b), the subscript on the variables going from 0 to j.

A similar array for the source $-\tilde{F}(\xi_2^r)$, located at $z = R\cos(\Omega_1)$, $x = -R\sin(|\Omega_1|) - 2a$, is shown in Figure 22. Again,

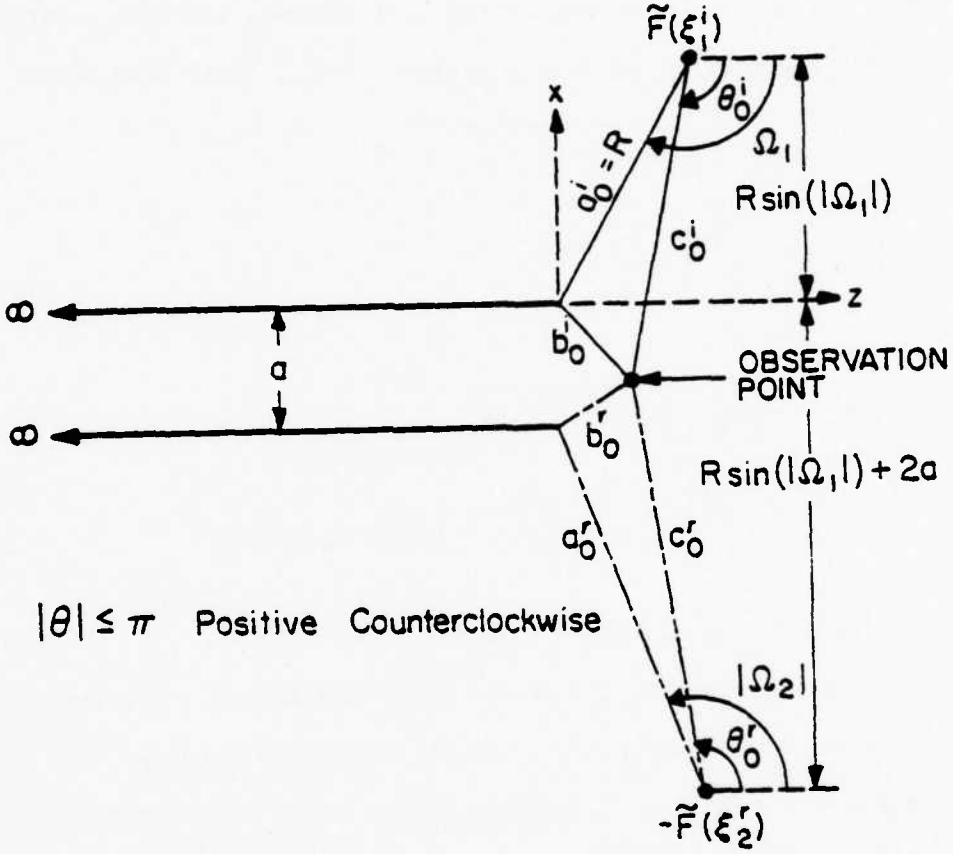

Figure 20. UAT, geometrical optics field sources in (III.50).

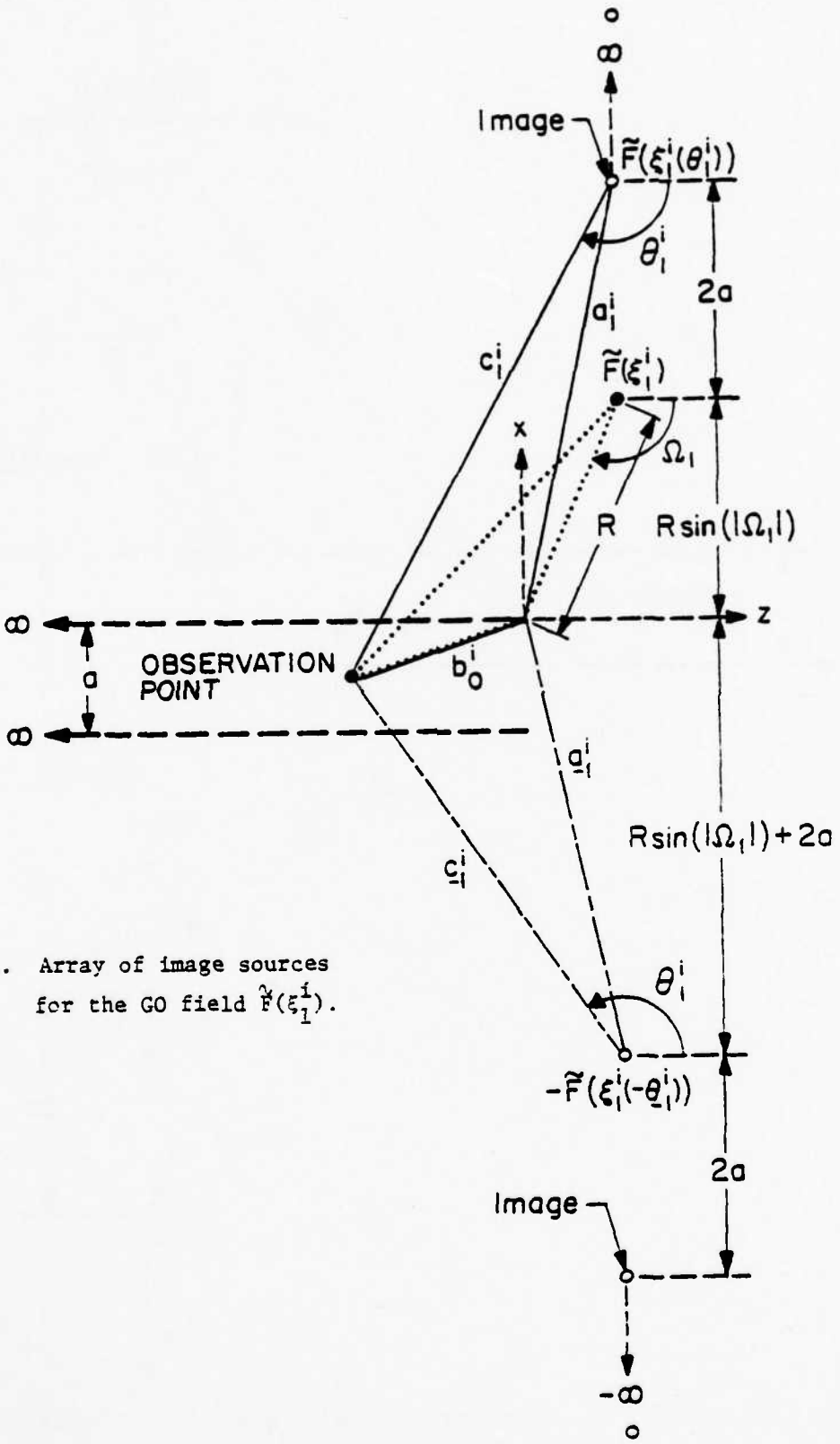

Figure 21. Array of image sources for the GO field $\tilde{F}(\xi_1^i)$.

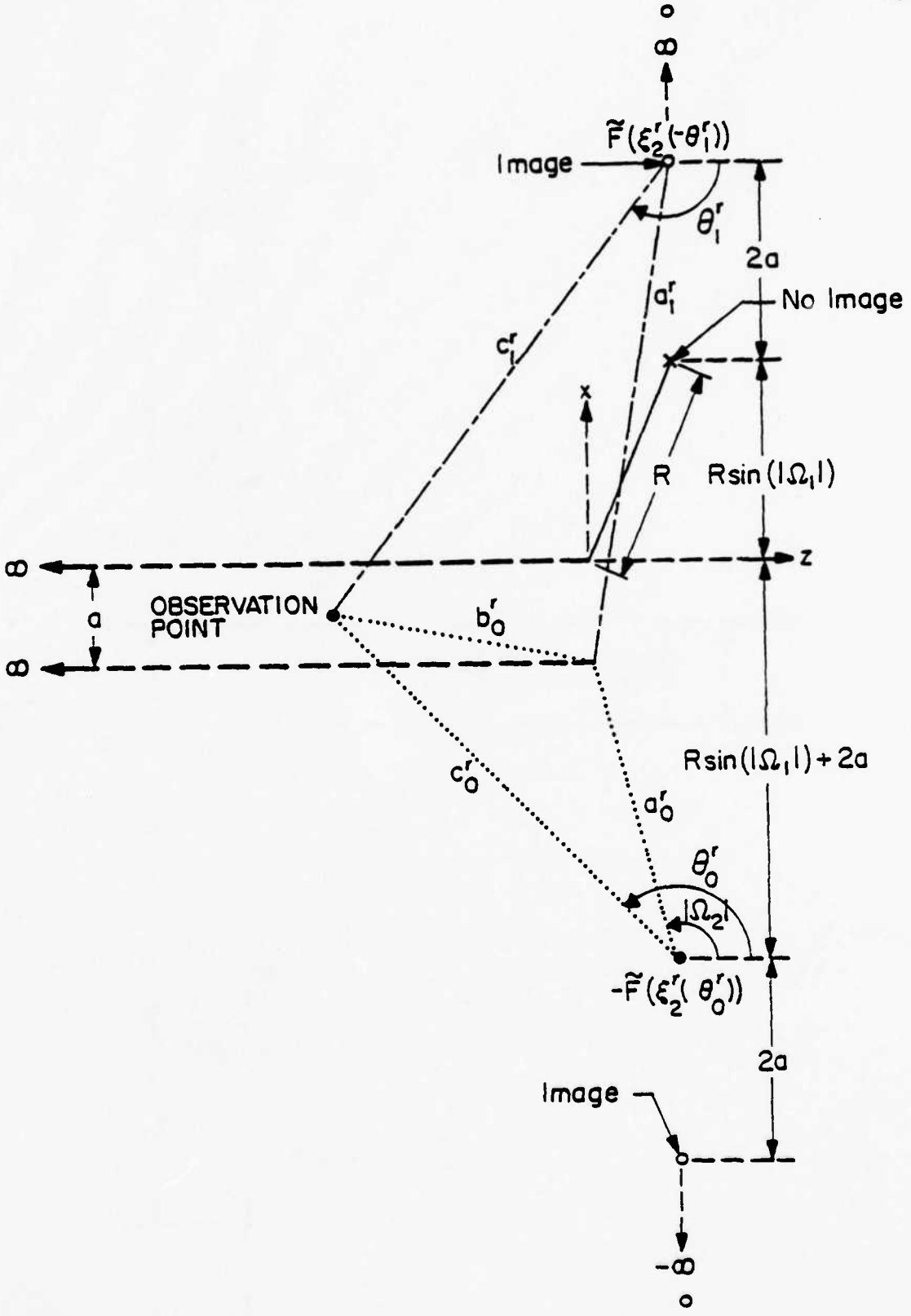

Figure 22. Array of image sources for the GO field $\tilde{F}(\xi_2^i)$. Note absence of a source at x = R sin(|Ω|).

note the change of sign for $x > 0$ and also that now there is no image at $x = R \sin(|\Omega_1|)$. As before, the detour parameters are calculated from (III.52c) and (III.52d).

Now we let R be large but still finite. It immediately follows that $\Omega_1 \simeq \Omega_2$. Furthermore, if we let the observation point recede deep into the waveguide, that is, $|z| \to \infty$, both ξ_1 and ξ_2 become large, but as can be seen from (III.52), are of opposite sign. The addition then of the fields in Figure 21 and 22 leaves the field from the source at $z = R\cos(\Omega_1)$, $x = R\sin(|\Omega_1|)$, radiating in free space. But since ξ_1^i is now large and the observation point is deep inside the waveguide, in the shadow region, we conclude that the GO field deep in the guide is zero.

The fact that neither Equation (III.18) or (III.48) shows the GO field should not, however, be taken to mean that only the diffracted field is needed when considering the primary field contribution. We can, instead of looking into the far field of the guide, find c_n^p by integrating the primary field over the guide aperture at $z = 0$. That is,

$$c_n^p = \frac{2}{a}\int_{-a}^{0}\left[(F(\xi_1^i) + F(\xi_2^i) - 1)\phi^i - F(\xi_1^r)\phi_1^r - F(\xi_2^r)\phi_2^r\right]\Big|_{z=0}\sin\left(\frac{n\pi}{a}x\right)dx \tag{III.53}$$

where we used (II.34) to express the primary field. If, however, instead of the full expression in (III.53) we were to use the diffracted fields only and calculate c_n^p by

$$c_n^{p'} = \frac{2}{a}\int_{-a}^{0}\left[\phi_1^d + \phi_2^d\right]\Big|_{z=0}\sin\left(\frac{n\pi}{a}x\right)dx \quad , \tag{III.54}$$

c_n^p would be greatly underestimated. This can be seen in Figure 23, where for a typical case, we compare the magnitudes of c_1^p as calculated from (III.48)

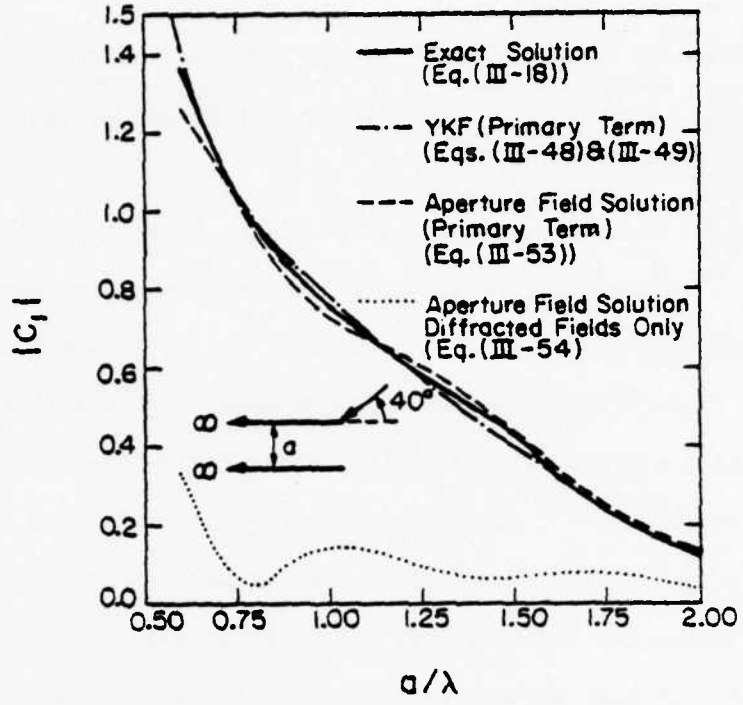

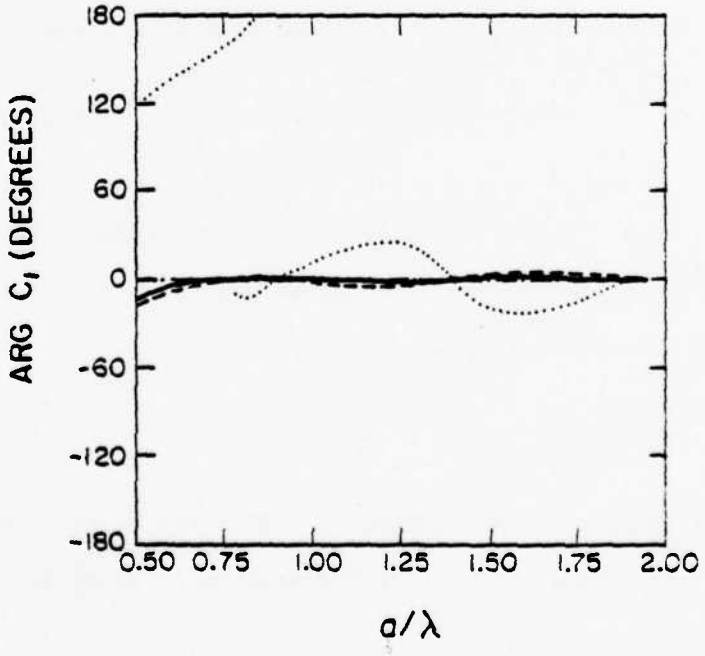

Figure 23. Magnitude and phase of the TE_{10} modal coefficient.

and (III.49), (III.53) and (III.54). We also observe that the asymptotic solution breaks down near cut-off.

The answer, then, to the question of whether one should include the GO field is dependent on where the observation point is. If one is examining the aperture field, the GO field must be included. If one is studying the far field, the GO field drops out, hence, the appearance of only the diffraction coefficient. But this does not mean that only the knowledge of the diffracted field is sufficient to find c_n^p. It is sufficient only if the integration is done in the far field.

C.4. Primary field: Aperture field method

Equation (III.53) suggests another way of computing the primary contribution - find and integrate the primary field over the aperture. This approach has several important advantages. First, by not looking down the guide, there's no need to track the reflections which, as just seen, can lead to complicated forms. And, although analytic expressions such as (III.48) and (III.49) cannot be found, the aperture field integral can be easily and very accurately numerically integrated, as its limits are from -a to 0. Furthermore, though Figure 23 seems to indicate little reason for choosing the aperture field method over the asymptotic solution, the aperture field method is superior in that Equation (III.53) contains no singularities and hence the procedure is easily extended to the staggered case. Additional details on the aperture field method are discussed in Chapter IV.

C.5. Multiple scattering

The solutions in Equations (III.48), (III.49) and (III.53) are based on the assumption that each plate in the guide is excited by the incident field alone. In fact, each plate is also excited by the fields scattered off the other plate so that the effects of multiple scattering must be considered. In the exact solution, this effect has been accounted for in toto by the use of the Modified Diffraction Coefficient (MDC). The ray optics solution, on the other hand, given by Yee and Felsen [30], attempts to keep track of each of the interactions. This is now briefly outlined and the limitations of the technique discussed.

Consider for example the field scattered off the top plate, as in Figure 24. We denote the scattered field off plate 1 after (m + 1) scatterings by $\phi^s_{1,m}$, likewise for plate 2 by $\phi^s_{2,m}$. To find the scattering of $\phi^s_{1,0}$ by plate 2, the YKF solution proceeds as follows. First, assume that the initial scattered field $\phi^s_{1,0}$ near the lower edge is well-approximated by the diffracted field. Next, approximate this first diffracted field by an isotropic line source field, its strength given by $D(\Omega, \pi/2)$. As this field scatters off plate 2, the resultant scattered field near the aperture, denoted by $\phi^s_{2,1}$, is

$$\phi^s_{2,1} = D(\Omega, \pi/2)\{g(ka)D(\pi/2,\theta_2)g(k\rho_2) - [F(\xi^r_1) - \hat{F}(\xi^r_2)]g(k\rho_r)\}. \quad \text{(III.55)}$$

As we again consider the scattering of $\phi^s_{2,1}$ off plate 1 to obtain $\phi^s_{1,1}$, we observe that the top edge and, indeed, the entire aperture lies on the reflected shadow boundary of $\phi^s_{2,1}$. However, note that even on the shadow boundary $\phi^s_{2,1}$ is finite and is equal to $\frac{1}{2}D(\Omega, \pi/2)g(k\rho_r)$.

To find the scattered field $\phi^s_{1,1}$, again the approximation is made that $\phi^s_{2,1}$ is an isotropic line source field of strength $\frac{1}{2}D(\Omega, \pi/2)$ and the entire procedure repeated to find the next higher-order scattering. When this

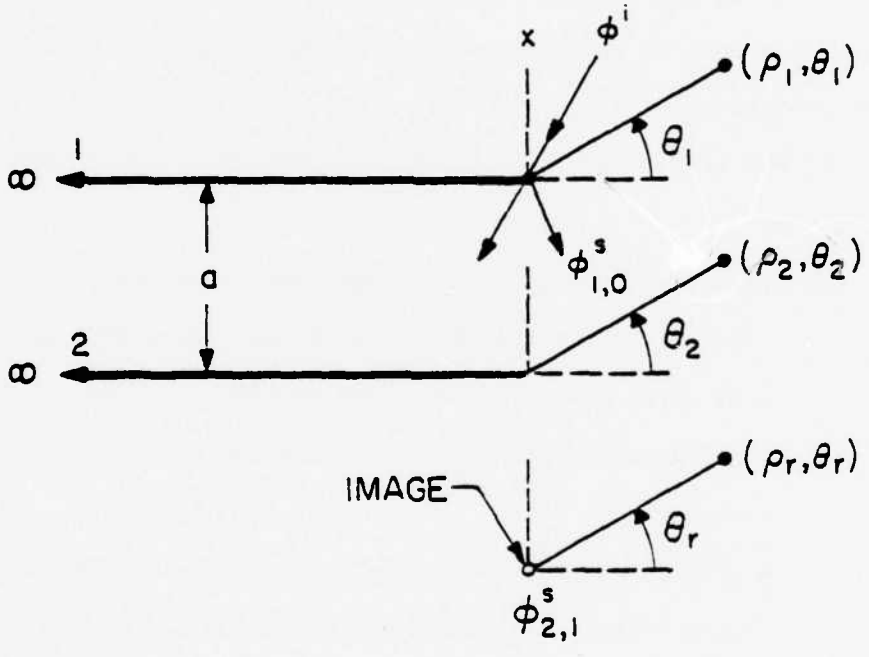

Figure 24. Multiple scattering between the plates.

is all done, the modal coefficient due to the interactions is

$$c_n^{int} = D(\Omega, \pi/2)[\phi^i(0,0) + e^{i(n+1)\pi}\phi^i(0, -a)] \frac{D(\frac{\pi}{2}, \phi_n - \pi)}{4ka \cos \phi_n} \times \sum_{m=1}^{\infty} \left(\frac{e^{ima}}{\sqrt{m}\ (2)^{m-1}} \right). \tag{III.56}$$

That is, the multiply diffracted fields are reduced by one-half upon each diffraction and the coupling of these fields computed as in Section C.2. An interesting comparison of (III.56) with the asymptotic expansion of the exact solution, made by Bowman [9], shows that (III.56) would tend to underestimate c_n^{int}.

The YKF method for the interactions then makes use of three basic assumptions:

(a) On opposite plates, the primary scattered field is well-approximated by the diffracted field. This will be true if a is large and ϕ_n is not close to $\pi/2$.

(b) The diffracted fields are approximated by an isotropic line source field.

(c) A greater approximation than the isotropy of the diffracted fields is that ray fields are used at all. Equation (III.55) clearly shows that after the first interactions the edges lie in the transition region of the interacting fields, where a ray picture of any kind is inappropriate. Furthermore, near cutoff, that is, $\phi_n \to \pi/2$, the ray picture becomes even more confusing. In Chapter IV, the interactions are partially taken into account in a more exact manner.

D. Summary and Conclusions

D.1. Exact and asymptotic Wiener-Hopf solution (MDC)

In Section A an exact solution for the modal coefficients of an unstaggered parallel-plate guide was found. The expression, given in

Equation (III.18), shows that the modal coefficients are proportional to the amplitude of the diffraction coefficient in the modal direction, multiplied by a factor which accounts for the interaction between the plates. This then leads to the introduction of the Modified Diffraction Coefficient (MDC) in Equation (III.20). Note that, generally speaking, the MDC will not give a ray field since it is a function of k, indicating that the interaction is of a complicated, nonray-like nature.

In Section B, an asymptotic solution valid for large "ℓ" was introduced in Equation (III.38). We note again the use of the MDC, but now also the presence of singularities in Equations (III.38c) and (III.38d) as $\delta \to \phi_n$. These singularities arise from the assumptions of the asymptotic evaluations and may in principle be removed [1], though this would lead to exceedingly complex forms.

Taking into account the inherent limitations of the asymptotic solution, when can Equation (III.38) be expected to give good results? "When "ℓ" is large enough so that the lower edge is outside the transition region centered about the aperture, as shown in Figure 25." This transition region is the region in which the interactions between the plates take place, as outside of this region we have ray fields which only produce specular reflections. When the lower edge falls out of this region, the use of the MDC to account for the interactions is justified. Simple calculations show "ℓ" would have to be greater than a wavelength, for example, when $a = .55\ \lambda$, $\ell > 1.1\ \lambda$. When $a = 1.2\ \lambda$, the minimum "ℓ" increases to $\ell > 1.4\ \lambda$.

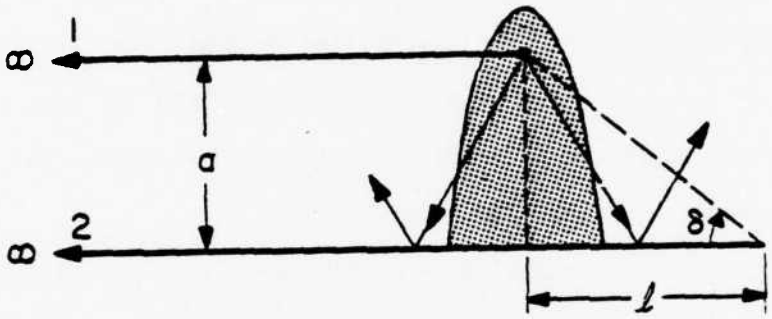

Figure 25. Transition region of the interactions along the aperture.

D.2. YKF and aperture field method

In Section C, a ray optics solution for the unstaggered guide was presented. It was shown that the primary field's contribution to the modal coefficient was through the diffracted fields only, the GO field being absent because a far-field evaluation was involved. It was also seen that because the guide was unstaggered the singularities in the diffraction coefficient cancelled. An equivalent formulation for the primary field's contribution, an aperture field method, was given, and shown to be preferable in many ways. The YKF method for the interactions was discussed and its shortcomings pointed out, namely, the presence of a singularity near cutoff, and the use of ray fields in the transition region.

D.3. Extension to the staggered case

For "ℓ" > 0 the results in Section B have an obvious and immediate application. However, as pointed out the MDC has several shortfalls. First, for the MDC to be successfully applied, the stagger must be large - greater than one wavelength. Second, the terms which give the first interaction along the diagonal, Equations (III.38c) and (III.38d), are singular as $\delta \to \pi - \Omega$ and are discontinuous due to the presence of the function H( ). The YKF method has similar problems; a singularity when $\delta \to \pi - \Omega$, the need for "ℓ" to be large so that the interaction rays are indeed rays on the opposite plates, and, in addition, the primary field term is singular when $\phi_n \to \pi/2$. A comparison between the MDC, the YKF, and the more rigorous Aperture Field Method for a staggered guide is given in Section D, Chapter IV.

IV. STAGGERED GUIDE

We examine now the staggered wave guide, $\ell \neq 0$, in Figure 1. As in Chapter III we only study the E-wave problem in detail and show how to apply the method to an H-wave case. In Section A we find the plane wave primary field contribution to the modal coefficient and make use of the Aperture Field Method introduced in Chapter III. In Section B interactions between the plates are considered and the Spectral Theory of Diffraction is utilized to exactly solve for the first interaction. Data are presented in Sections C and D and the cylindrical wave problem is examined in Section E. Finally, we note that, although in this chapter we are solely interested in the propagating modes, the same methods may also be used for the evanescent modes.

Rather than dealing with C_n, the modal coefficient of the n^{th} propagating mode, we use P_n, the power transmission coefficient, defined as the ratio of the mode power to the source power incident on the aperture, projected in the direction of the waveguide, i.e.,

$$P_n = \frac{|C_n|^2 \cos \phi_n}{2|\cos(\Omega)|} \quad , \tag{IV.1}$$

as illustrated in Figure 26. The same definition is used when $\Omega > 0$, though in this case, P_n has less physical meaning. Observe that because of the way P_n is defined it is possible for it to be greater than one. We define the phase shift of the mode as the phase of C_n minus the incident field's phase at the center of the aperture, $(-a/2,0)$. That is,

$$\text{Phase Shift} = \arg C_1 - \arg \phi^i(-\frac{a}{2}, 0). \tag{IV.2}$$

A. Primary Contribution (Plane Wave): Aperture Field

The primary contribution to the modal coefficient is found by the Fourier decomposition of the primary field over the guide aperture, as

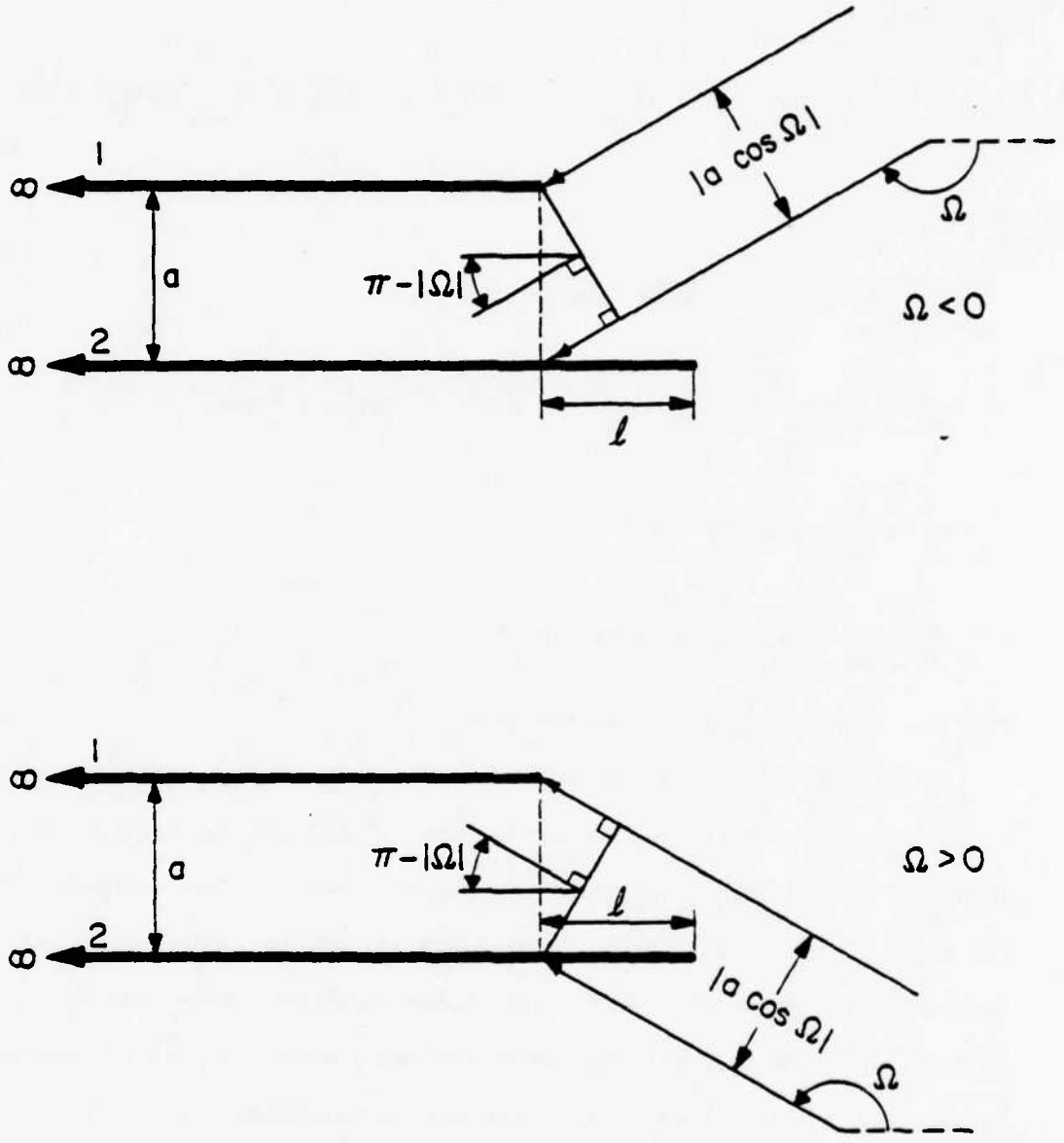

Figure 26. Geometry in the definition of P_n (IV.2).

in Equation (III.53). But now, for any $\ell \geq 0$, we have for the primary field contribution

$$C_n^p = \frac{2}{a}\int_{-a}^{0}\left[(F(-\xi_1^i) + F(\xi_1^r))\phi^i - F(\xi_1^r)\phi_1^r - F(\xi_2^r)\phi_2^r\right]\Big|_{z=0}\sin\left(\frac{n\pi}{a}x\right)dx \tag{IV.3}$$

where

$$\xi_1^{i,r}(x,0) = \varepsilon_1^{i,r}\left|\sqrt{2k|x|}\,\sin\left(\frac{\Omega}{2} \pm \frac{\pi}{2}\right)\right|$$

$$\xi_2^{i,r}(x,0) = \varepsilon_2^{i,r}\left|\sqrt{2k[(a+x)^2 + \ell^2]^{1/2}}\,\cos\left(\frac{\Omega}{2} \pm \frac{1}{2}\tan^{-1}\left(\frac{a+x}{\ell}\right)\right)\right|$$

$$\phi_1^r(x,0) = \exp[-kx\sin\Omega]$$

$$\phi_2^r(x,0) = \exp[-ik(x+2a)\sin\Omega] \quad .$$

When $\ell = 0$, (IV.3) reduces to (III.53).

In Figures 27 and 28, we show for $\ell = 0$ some typical comparisons of P_n and the phase shift, as calculated from (IV.3), and the same parameters obtained from the exact solution. We see that (IV.3) gives accurate results, the error in P_n is kept under 10% or $\pm$ 0.8 dB, and the phase shift less than 10°. The greatest errors occur at the onset of a mode when P_n is most sensitive to small changes in the aperture field. As a/λ increases, the agreement with the exact solution becomes excellent.

B. First Interaction (Plane Wave)

The fields on the aperture due to the first interaction can be solved for exactly using STD. The scattered field of the first interactions can be written as

$$\phi^{int} = \phi_{1,1}^s + \phi_{2,1}^s \tag{IV.4}$$

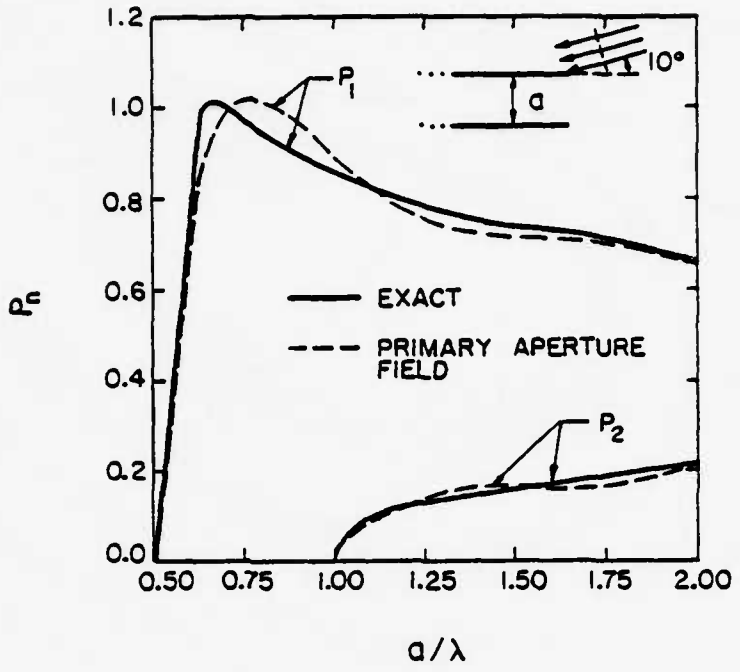

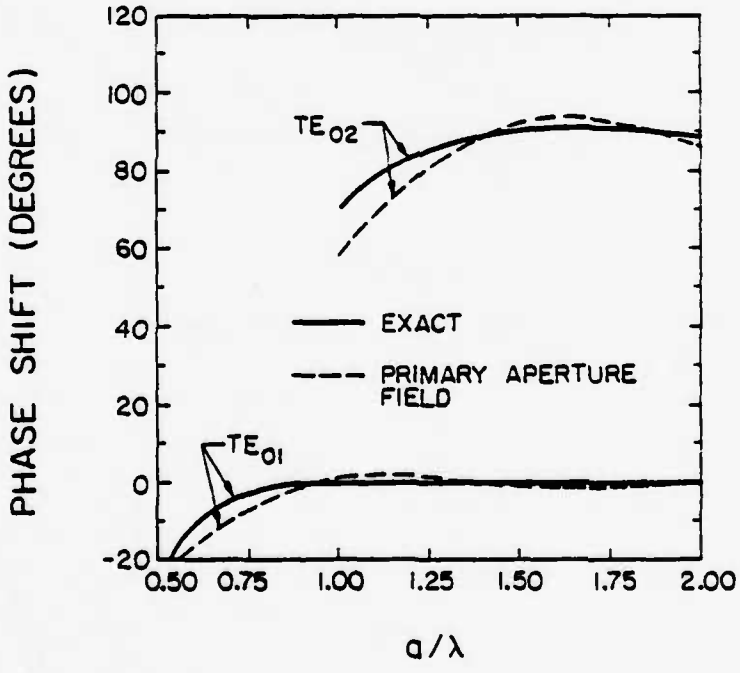

Figure 27. Power transmission coefficient and the phase shift of C_n. $\Omega = -170°$.

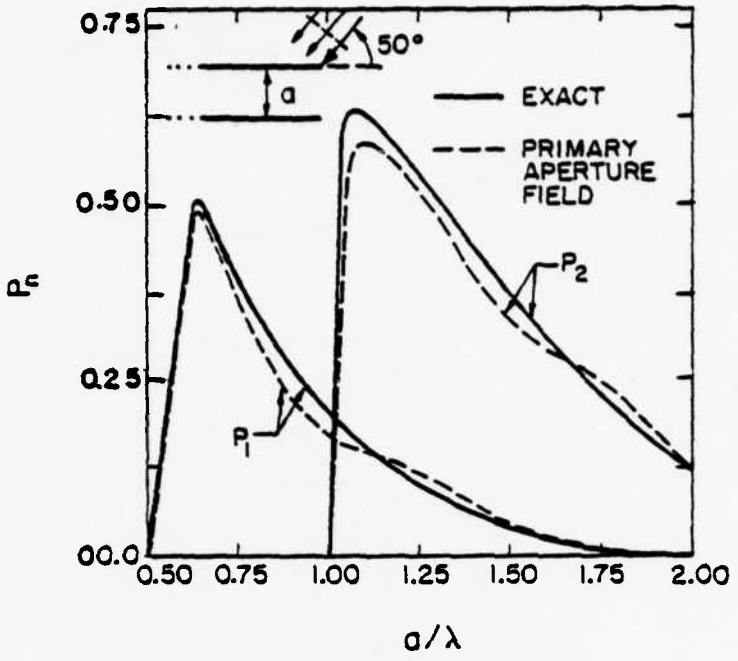

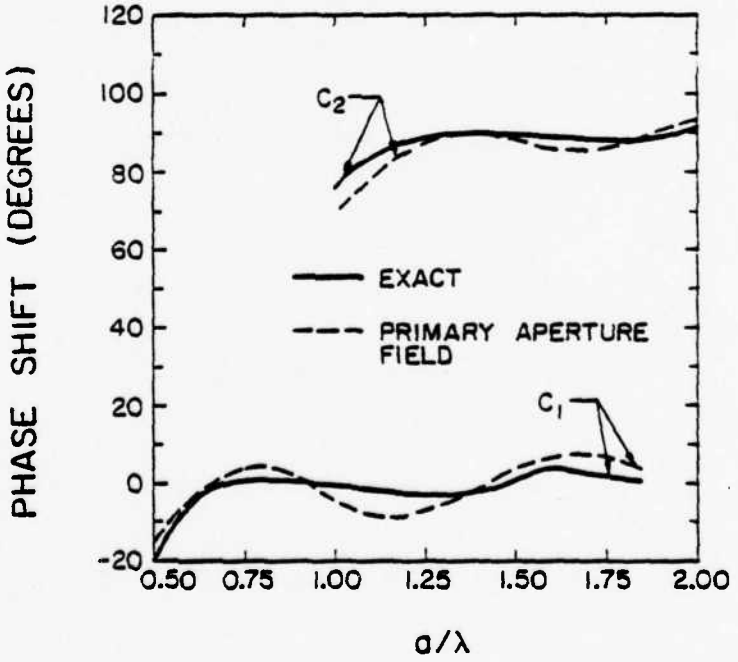

Figure 28. Power transmission coefficient and the phase shift of C_n, $\Omega = -130°$.

where, following the notation in Section C, Chapter III, $\phi^s_{1,1}$ is the field scattered off plate 1 when the incident field is $\phi^s_{2,0}$, and $\phi^s_{2,1}$ is the field scattered off plate 2 when the incident field is $\phi^s_{1,0}$. The scattered fields $\phi^s_{1,0}$ and $\phi^s_{2,0}$ are the primary scattered fields off plates 1 and 2, respectively, as indicated in Figure 29. From Equation (II.28) the primary scattered fields may be written as

$$\phi^s_{1(2),1} = \frac{i}{4\pi}\int_\Gamma \chi(\Omega,\psi)e^{ik\rho_{1(2)}\cos(\psi-|\theta_{1(2)}|)}d\psi \qquad \text{(IV.5)}$$

where (ρ_1,θ_1), (ρ_2,θ_2), and $|\theta| < \pi$ are the cylindrical coordinates attached to the edges of plates 1 and 2, respectively, and Γ is the path in Figure 5. Note that Equation (II.28) applies when $\Omega > 0$. For $\Omega < 0$ we use the fact that $\phi^s(-|\Omega|,\theta)$ equals $\phi^s(|\Omega|,-\theta)$, which for an E-wave is the same as $\phi^s(|\Omega|,\theta)$.

Next, using superposition, as in (II.39), we obtain the expressions for $\phi^s_{1,1}$ and $\phi^s_{2,1}$

$$\phi^s_{1,1} = \frac{\phi^i(-a,\ell)}{4\pi i}\int_\Gamma \chi(|\Omega|,\psi)e^{-ikd\cos(\psi+\delta)}\Big\{F(-\xi^i_1)e^{ik\rho_1\cos(\psi-\theta_1)} + F(\xi^r_1)e^{ik\rho_1\cos(\psi+\theta_1)}\Big\}d\psi\,, \quad x > -a \qquad \text{(IV.6)}$$

where

$$\xi^{i,r}_1 = \mp\sqrt{2k\rho_1}\sin\left(\frac{\psi \mp \theta_1}{2}\right)$$

and

$$\phi^s_{2,1} = \frac{1}{4\pi i}\int_\Gamma \chi(|\Omega|,\psi)e^{ikd\cos(\psi-\delta)}\Big\{F(-\xi^i_2)e^{ik\rho_2\cos(\psi+\theta_2)} + F(\xi^r_2)\,e^{ik\rho_2\cos(\psi-\theta_2)}\Big\}d\psi\,, \quad x > -a \qquad \text{(IV.7)}$$

where

$$\xi^{i,r}_2 = \mp\sqrt{2k\rho_2}\sin\left(\frac{\psi \mp \theta_2}{2}\right)\,.$$

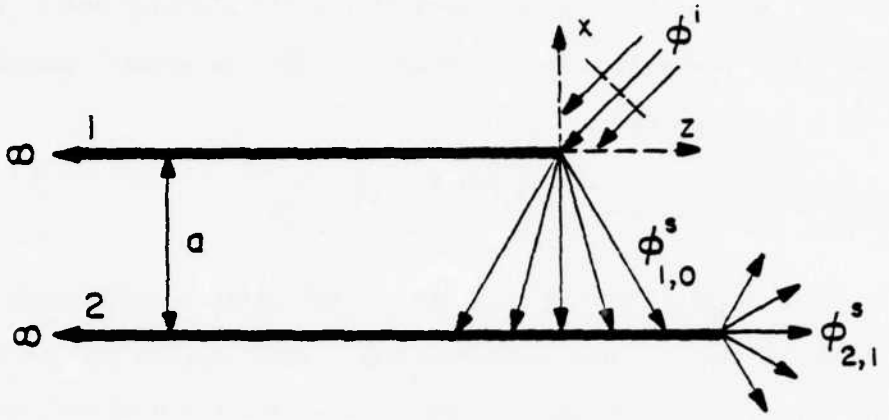

(a)

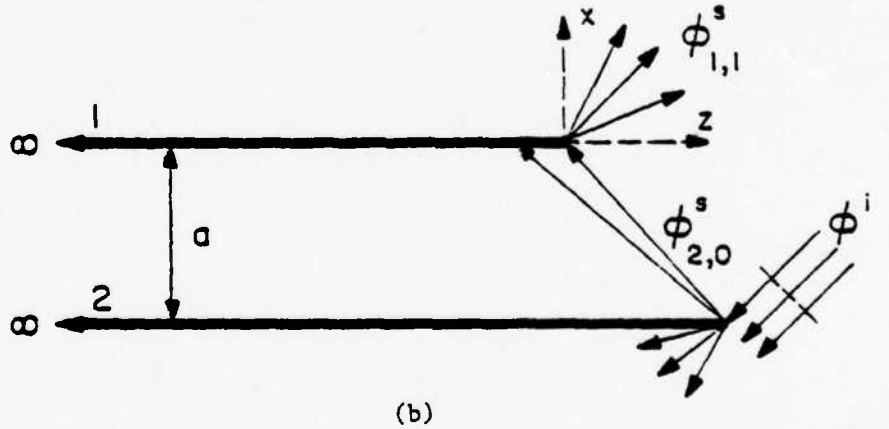

(b)

Figures 29a and 29b. First interaction between the plates.

The part of the modal coefficient due to these field terms is

$$c_n^{int} = \frac{2}{a} \int_{-a}^{0} (\phi_{1,1}^s(x,0) + \phi_{2,1}^s(x,0)) \sin\left(\frac{n\pi}{a} x\right) dx \quad . \tag{IV.8}$$

The evaluation of (IV.6) and (IV.7) is simplified by noting that for any spectral component in (IV.5) the incident shadow boundary is always outside the guide so that $F(-\xi_1^i)$ and $F(-\xi_2^i)$ may be ignored. Further simplification is possible by deforming the path Γ into a steepest descent path by the transformations

$$-ikd \cos(\psi + \delta) = ikd - kdt^2 \tag{IV.9}$$

for the integral in (IV.5), and

$$ikd \cos(\psi - \delta) = ikd - kdt^2 \tag{IV.10}$$

for the integral in (IV.7). The saddle points associated with the transformations (IV.9) and (IV.10) are $\pi - \delta$ and δ, respectively, and the residues to be considered are from the poles at $\psi = \pm\Omega$, respectively. Using then the steepest descent path transformations and the program for complex Fresnel functions in Appendix A, c_n^{int} can be computed with any of the standard quadrature methods.

The effects of the first interaction are examined for the test case $\ell = 0$. The same examples as in Figures 27 and 28 are now presented in Figures 30 and 31 but with the first interaction included. We see that the maximum error in P_n has been reduced by a factor of two to under 0.3 dB, and under 5° for the phase shift. Also the convergence to the exact solution as a/λ increases is more rapid, with the agreement already

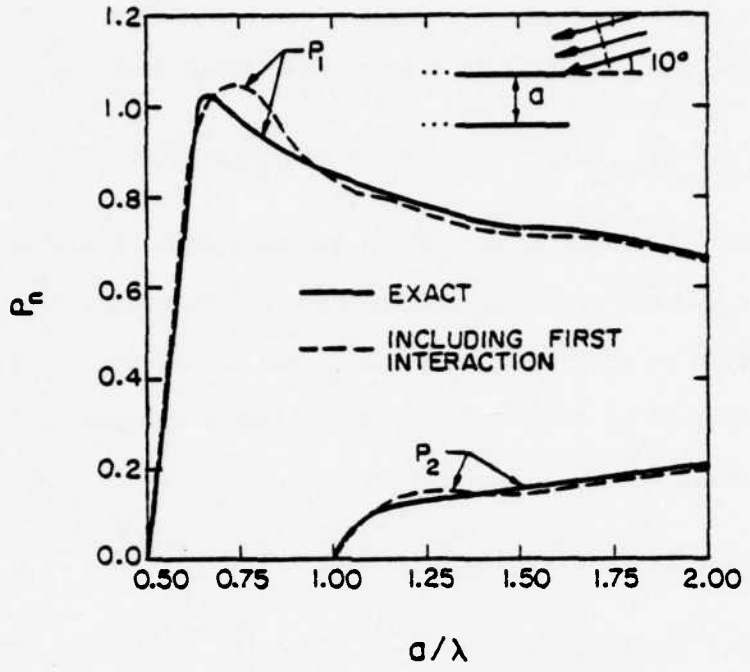

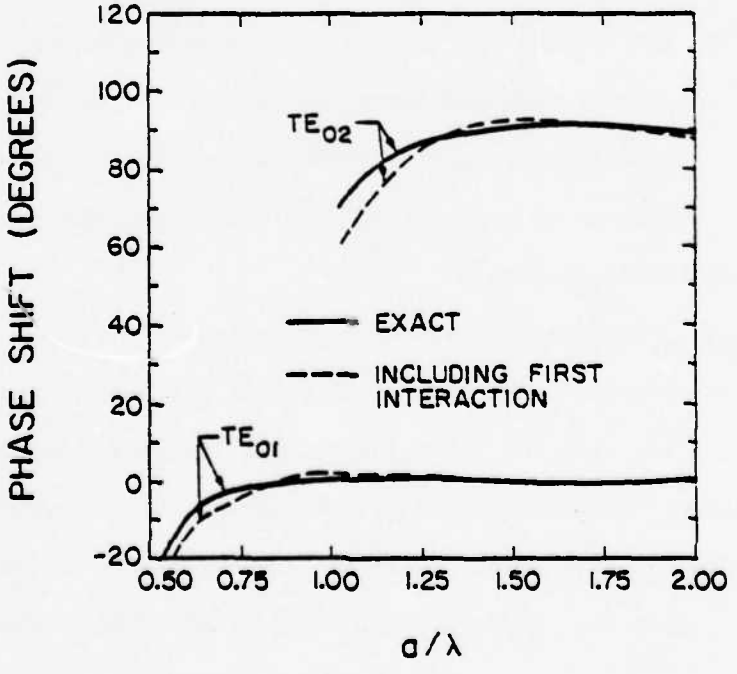

Figure 30. Power transmission coefficient and the phase shift of C_n, $\Omega = -170°$. First interaction included.

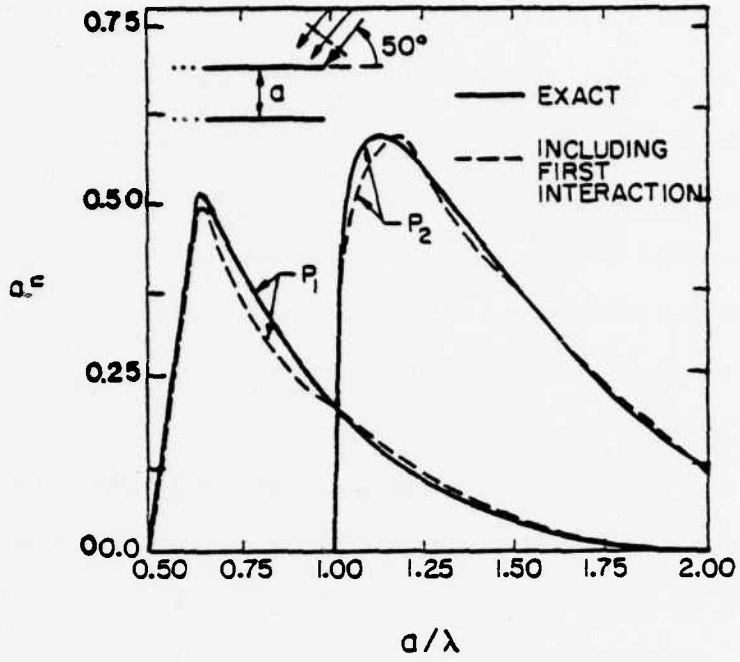

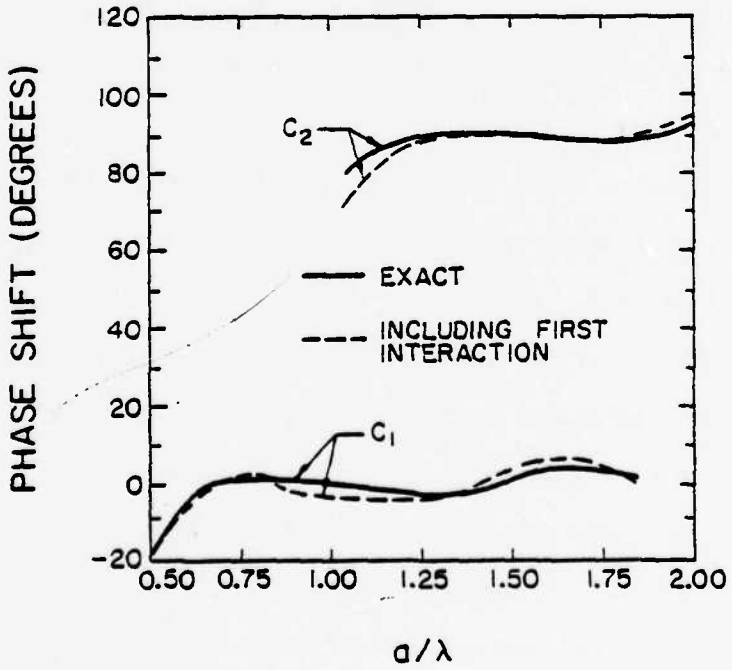

Figure 31. Power transmission coefficient and the phase shift of C_n, $\Omega = -130°$. First interaction included.

excellent for $a/\lambda \simeq 0.6$. Higher-order interactions are hereafter ignored as an exact formulation of them, possibly via an integral equation, would little improve accuracy and any approximate technique would have an error at least as large as the error present now. We emphasize that the formulations here for the primary and interaction terms are equally valid for any "ℓ" and the same order of accuracy is expected as that for $\ell = 0$.

C. Numerical Results

We study the staggered guide making use of (IV.3) and (IV.8). Figures 32 thru 38 present for different angles of incidence Ω the power transmission coefficient and the phase shift for $a = 0.7\ \lambda$, $0.8\ \lambda$, and $0.9\ \lambda$ as a function of the stagger distance "ℓ." These cases, $0.5\ \lambda < a < 1\ \lambda$, are of particular interest as guides in the dominant mode are often used as the elements in lens antennas [28] and in other antenna systems [14]. Furthermore, it is for $0.5\ \lambda < a < 1\ \lambda$ that a more exact analysis is needed; for plate spacing this small asymptotic, high frequency methods cannot be expected to give very good results.

Figure 32 presents data for $\Omega = 180°$, that is, the wave vector is parallel to the guide aperture. As ℓ/λ increases, we see P_1 gradually decreasing, falling at $\ell = 1\ \lambda$ by about 3 dB. This is because the scattered field on the aperture is, essentially, the diffracted field from the edges of the two plates. As one of the edges moves away from the aperture, the scattered field on the aperture becomes reduced. However, as $|\Omega|$ decreases and the wave vector tends to parallelism with the aperture, several different effects can be discerned. First, for $\ell = 0$, P_1 decreases as $|\Omega|$ decreases. This is because as $|\Omega|$ decreases from 180°, the wave number $k \sin \Omega$ increases in magnitude, which results in a more rapid phase variation of the incident field on the aperture. In turn, this implies less power coupling into the fundamental mode.

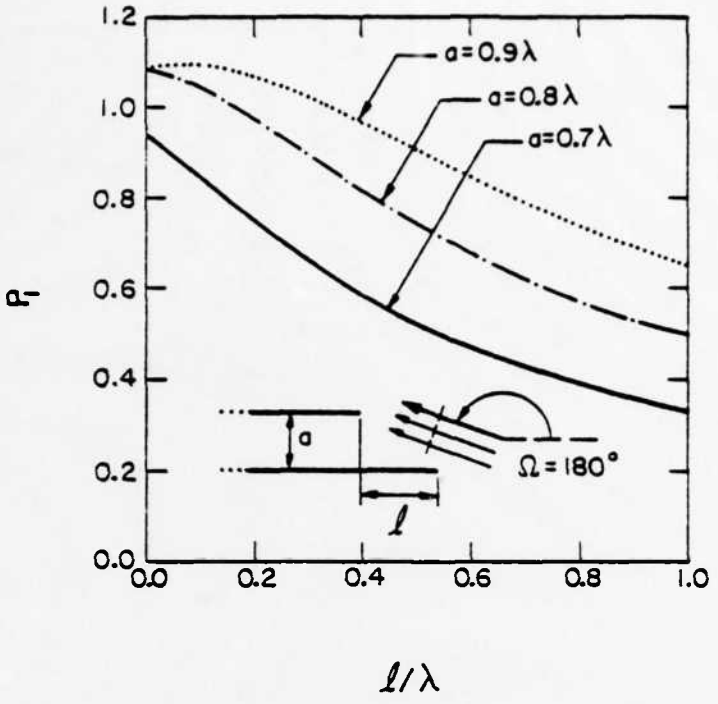

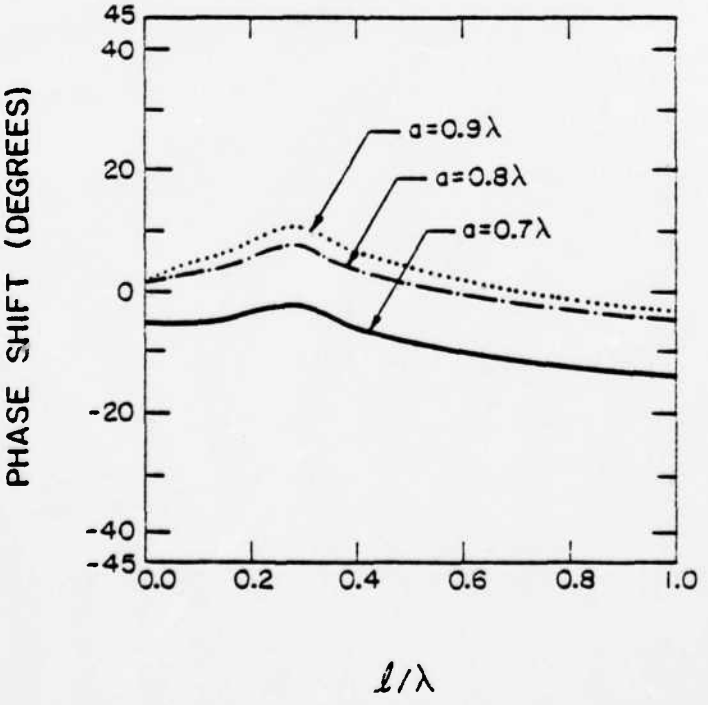

Figure 32. Power transmission coefficient and the phase shift of C_1, $\Omega = 180°$.

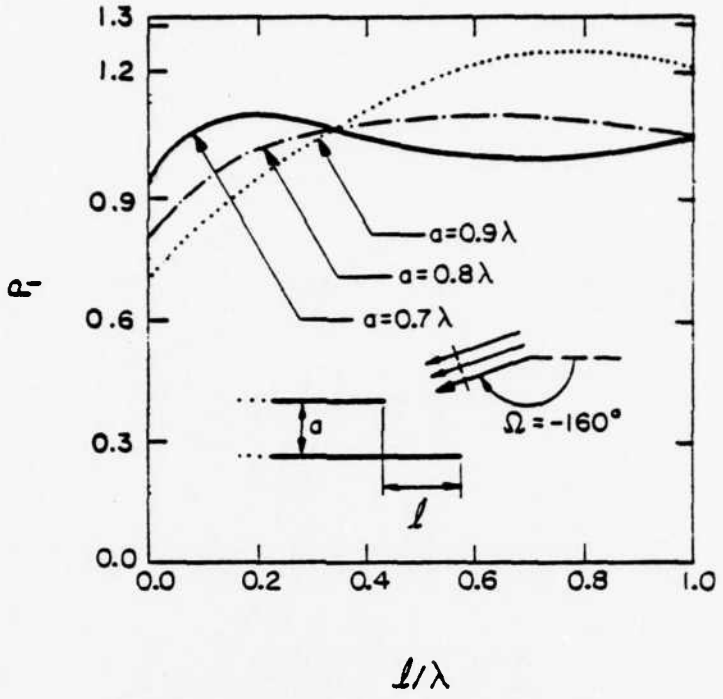

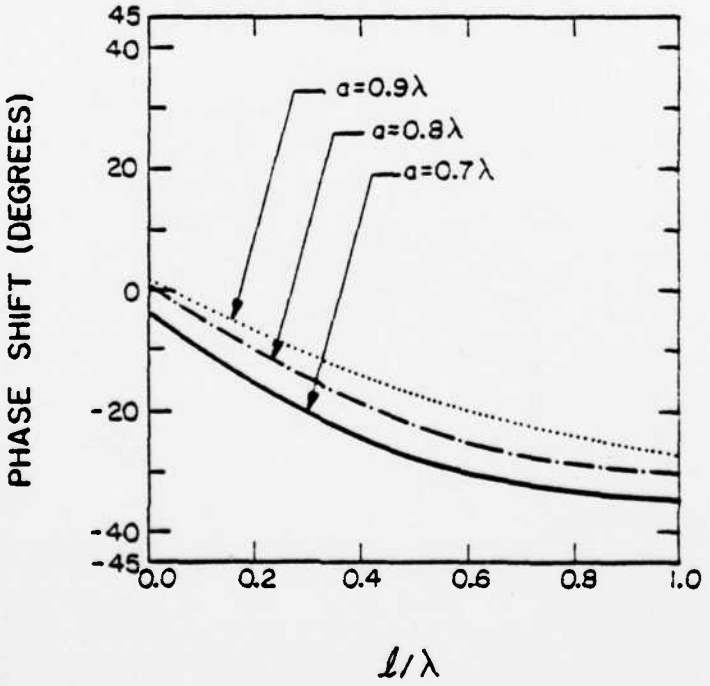

Figure 33. Power transmission coefficient and the phase shift of C_1, $\Omega = -160°$.

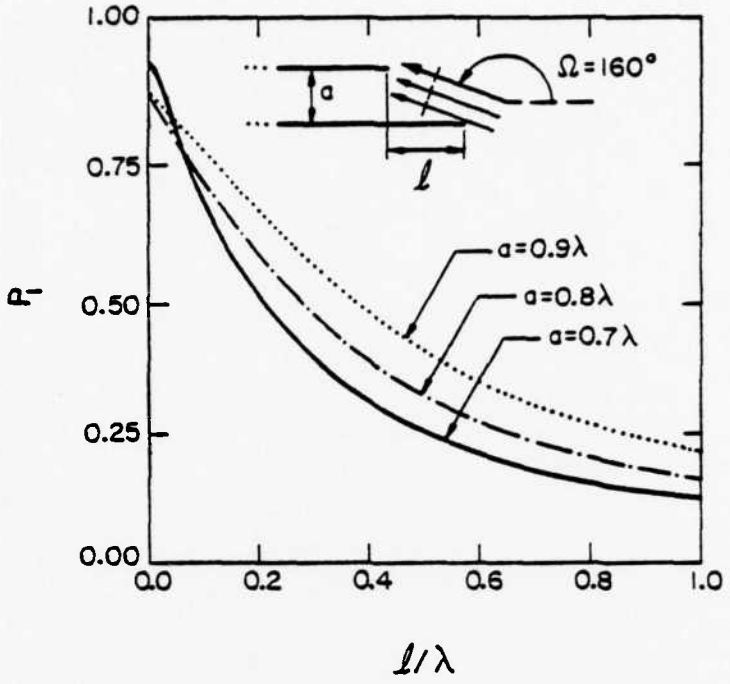

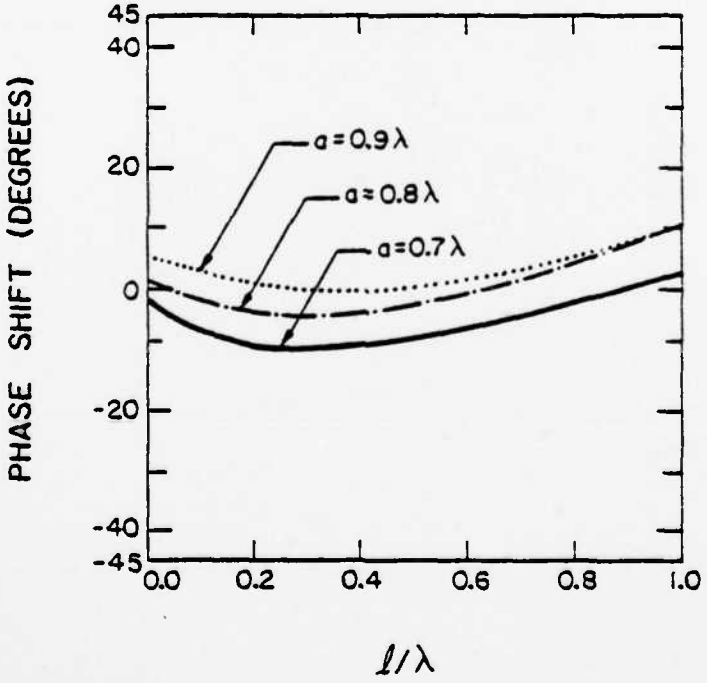

Figure 34. Power transmission coefficient and the phase shift of C_1, $\Omega = 160°$.

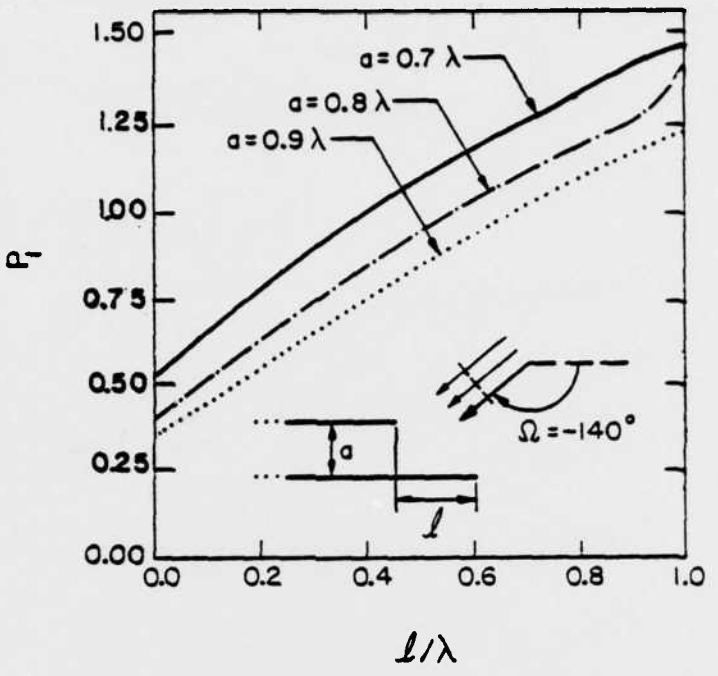

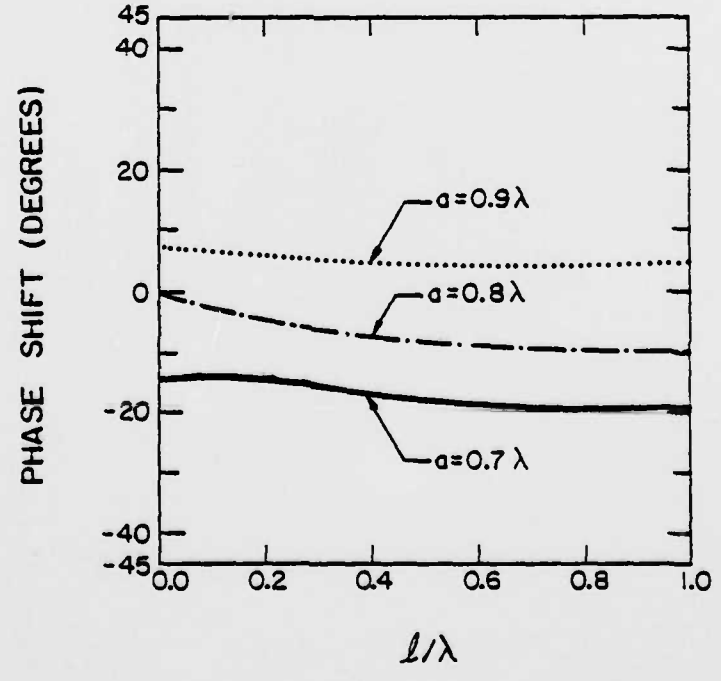

Figure 35. Power transmission coefficient and the phase shift of C_1, $\Omega = -140°$.

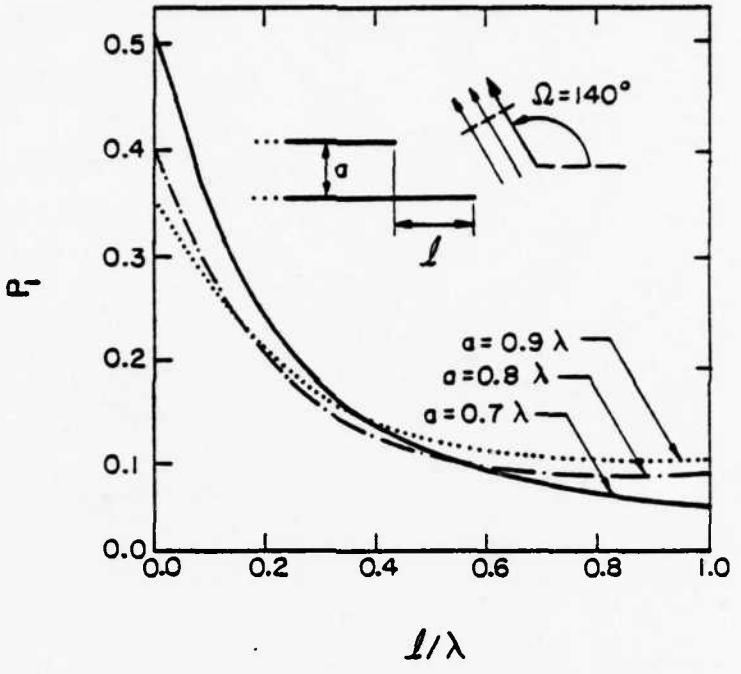

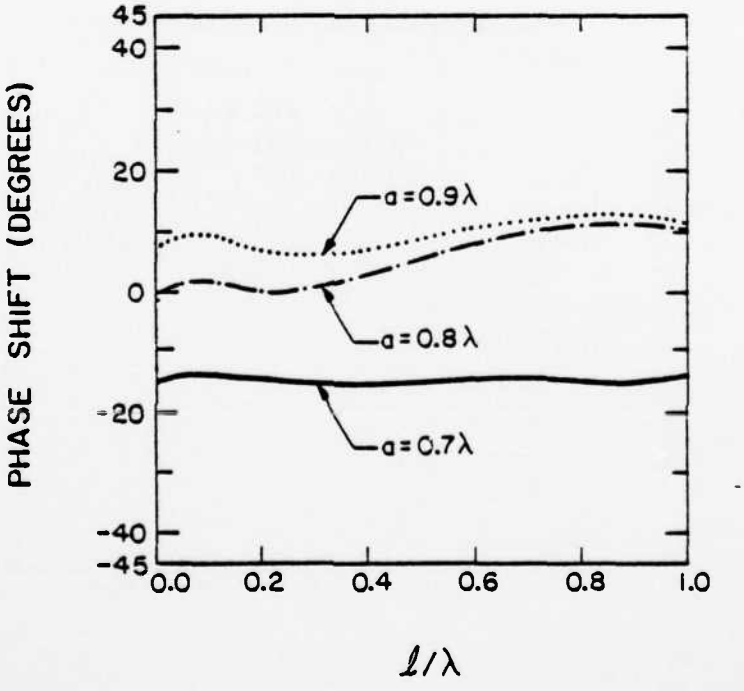

Figure 36. Power transmission coefficient and the phase shift of C_1. Ω = 140°.

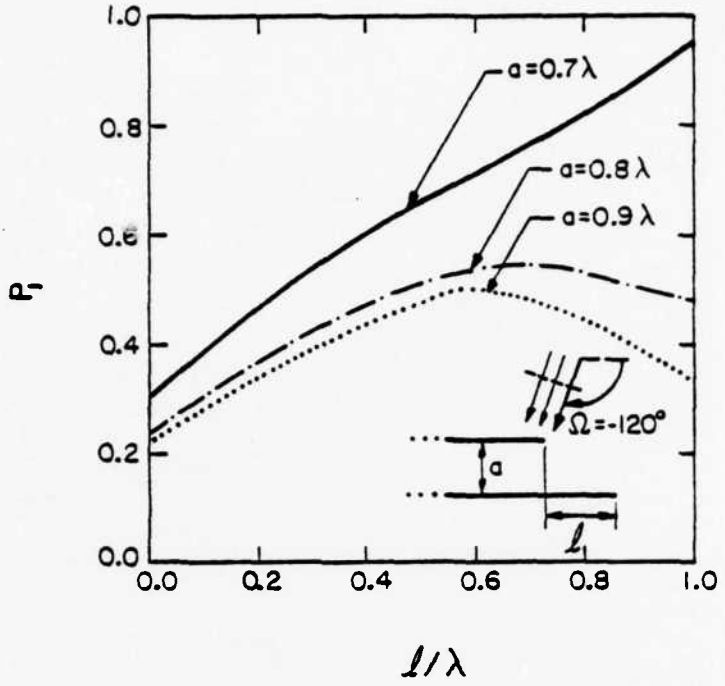

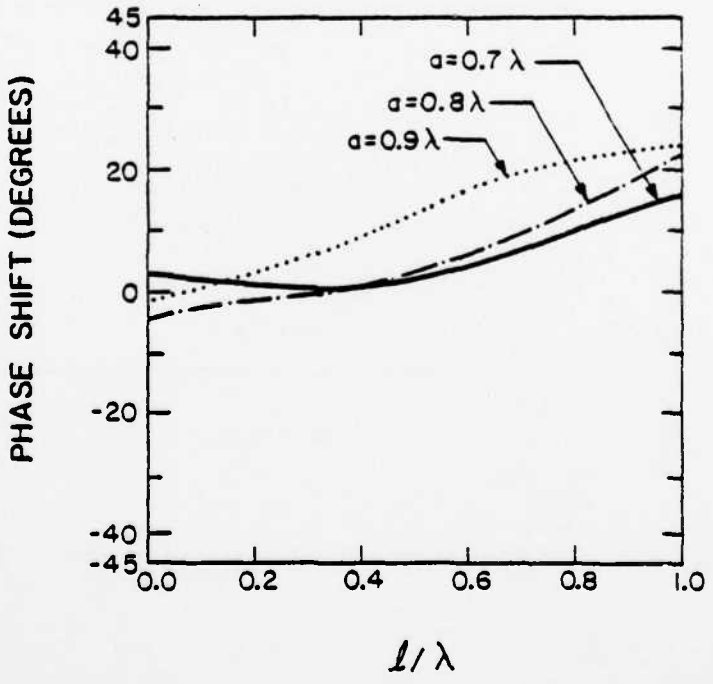

Figure 37. Power transmission coefficient and the phase shift of C_1, $\Omega = -120°$.

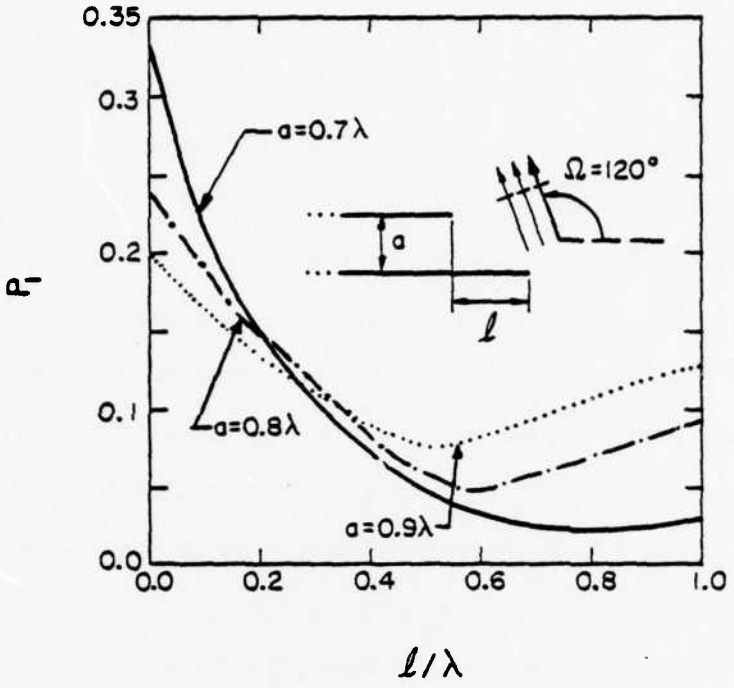

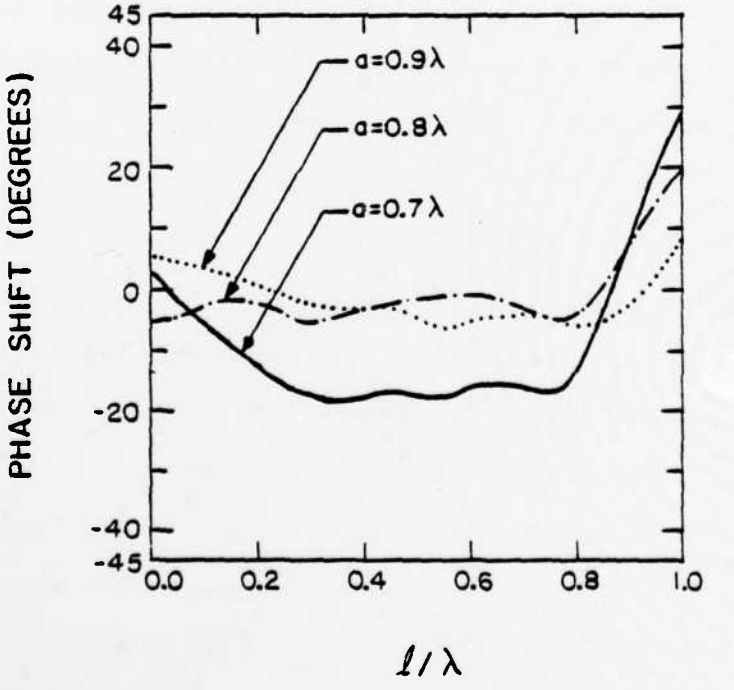

Figure 38. Power transmission coefficient and the phase shift of C_1, $\Omega = 120°$.

Second, for $\Omega < 0$, that is, the wave incident from above, as $|\Omega|$ decreases and ℓ/λ increases, we see more power in the dominant mode. Although the diffracted field on the aperture from the bottom plate decreases, more energy is now channelled into the guide by the stagger via reflection. On the other hand, for $\Omega > 0$, less field appears on the aperture as the stagger now acts to block out the incident field. For $|\Omega|$ close to 90°, however, this pattern breaks down. The behavior of P_1 and the phase shift becomes more erratic as the entire aperture now lies in the transition region of the incident and reflected fields. Note that as $|\Omega| \to 90°$ the projected aperture goes to zero and hence, from (IV.1), P_1 goes to infinity.

Perhaps the most interesting result is the phase shift behavior. Except for $|\Omega|$ close to 90°, we see that the phase shift is very weakly dependent on "ℓ," and is less than 20°. One could essentially compute the phase shift for $\ell = 0$, for which an exact solution is available, and use the result for $\ell \neq 0$. Tables that can be used to compute the phase shift for $\ell = 0$ are provided in Appendix B. It is because of this very weak behavior of the phase shift with "ℓ" that simple phase front designs for waveguide lens antennas are successful [28].

D. Comparison of the Aperture Field, MDC and YKF Method

We now compare the aperture field method, the MDC method as given by Equation (III.38), and the YKF method. The YKF formulation for the staggered guide is the same as the MDC formulation in (III.38), but instead of the G_+ functions, Equation (III.56) is used for the interactions along the aperture. The results are shown in Figures 39 and 40. We observe that for small and moderate "ℓ" the MDC and YKF methods fail. This is because they include the interaction rays along the diagonal which, as ℓ

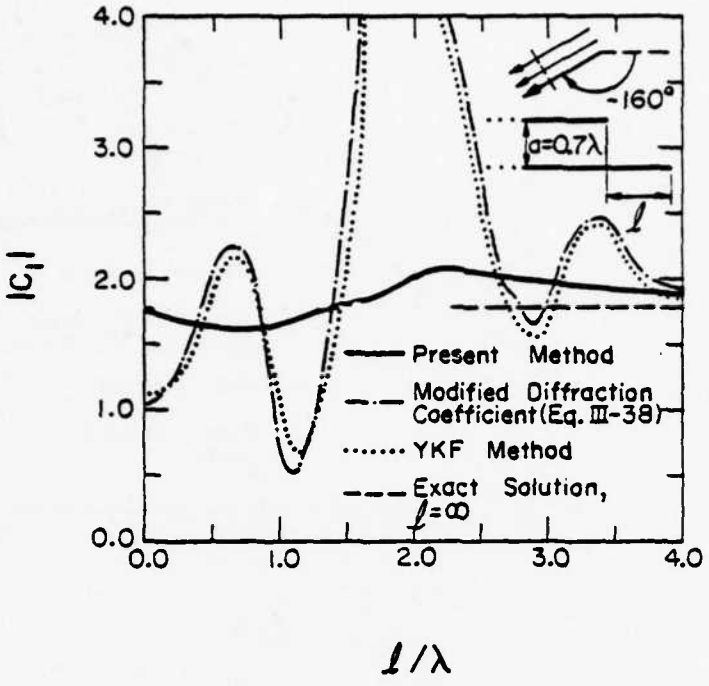

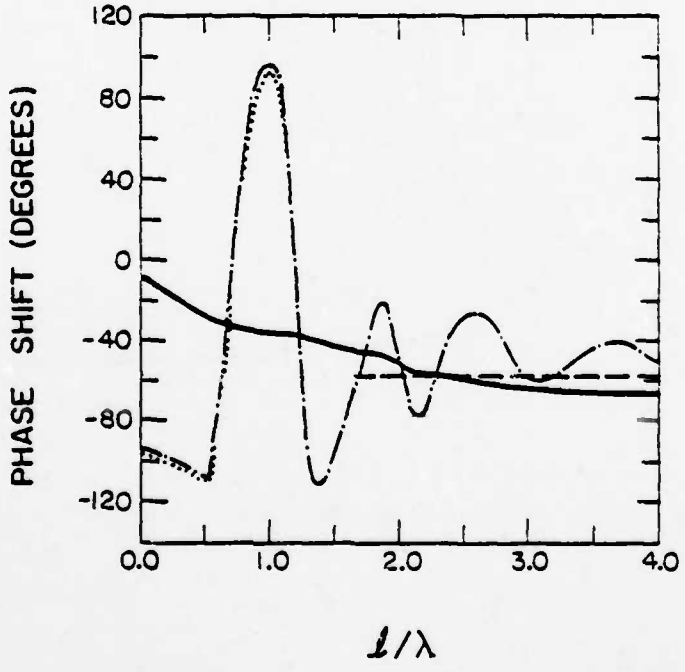

Figure 39. Magnitude and phase shift of C_1, $\theta = -160°$.

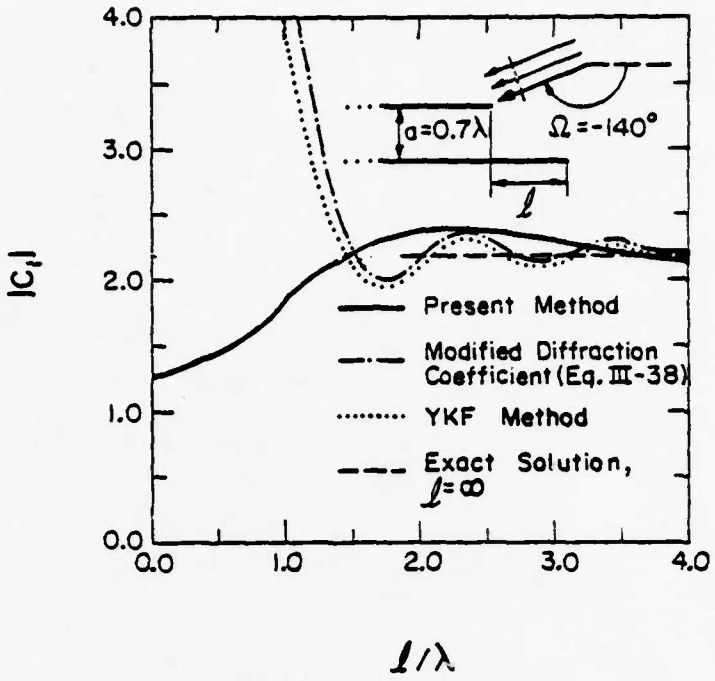

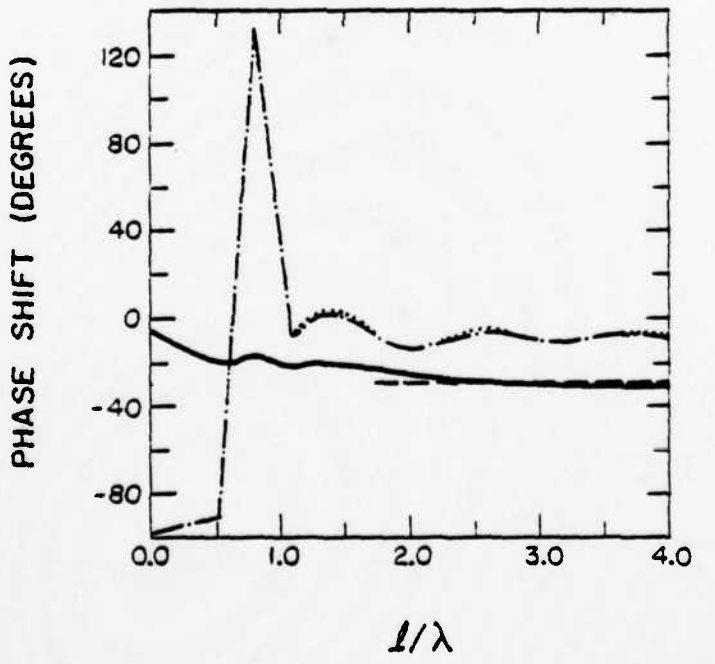

Figure 40. Magnitude and phase shift of C_1, $\Omega = -140°$.

approaches zero must be somehow removed, as they are not present in the canonical solution for $\ell = 0$. We observe in the figures the singularity at $\delta = \pi - |\Omega|$, something not present in the aperture field method. As ℓ increases all the methods approach the proper solution. It would appear from Figures 39 and 40 that if one is away from the singularity at $\delta = \pi - |\Omega|$, the MDC and YKF methods give good results for $\ell > 2\lambda$.

E. Incident Wave-Source Field

An advantage of the aperture field method is that it allows one to consider incident fields other than a plane wave. As an example we consider the problem of an incident line-source field, the geometry of which is given in Figure 17. The guide is unstaggered and the source coordinates are $(R \cos \Omega_1, R \sin|\Omega_1|)$, where R is now a finite number of wavelengths. The problem of finding the primary field contribution to the modal coefficient can be attacked in one of two ways. One could proceed in the manner of the YKF solution, as in Section C, Chapter III, but in this case an additional singularity is introduced in Equations (III.48) and (III.49) when Ω_1 or Ω_2 equals $\phi_n - \pi$. We recall that for an incident plane-wave the singularities in (III.48) and (III.49) cancelled out whereas for a line-source field they do not.

On the other hand, the aperture field method is simple. Though an exact solution to the problem of scattering of a line-source field is available [8], we prefer to use the asymptotic solution given in [7]. We begin by expanding the line-source field in an asymptotic series. Since we utilize the primary fields only our results will be accurate up to $0(k^{-3/2})$, and hence only the $k^{-1/2}$ term in the incident field expansion is retained. A higher order of accuracy can be obtained by first taking the plane-wave spectrum of the incident field and for each plane-wave component computing

the interactions between the plates as in Equations (IV.6) and (IV.7). This, however, would prove to be too laborious. With the incident field then given by (III.40) the primary field on the aperture is

$$\phi^t = \phi_1^G + \phi_2^G + \phi_1^d + \phi_2^d + 0(k^{-3/2}) \qquad \text{(IV.11)}$$

where ϕ^G and ϕ^d are given in Equations (II.46) through (II.53). Plots of the amplitude and phase shift for C_1 are given in Figures 41 and 42.

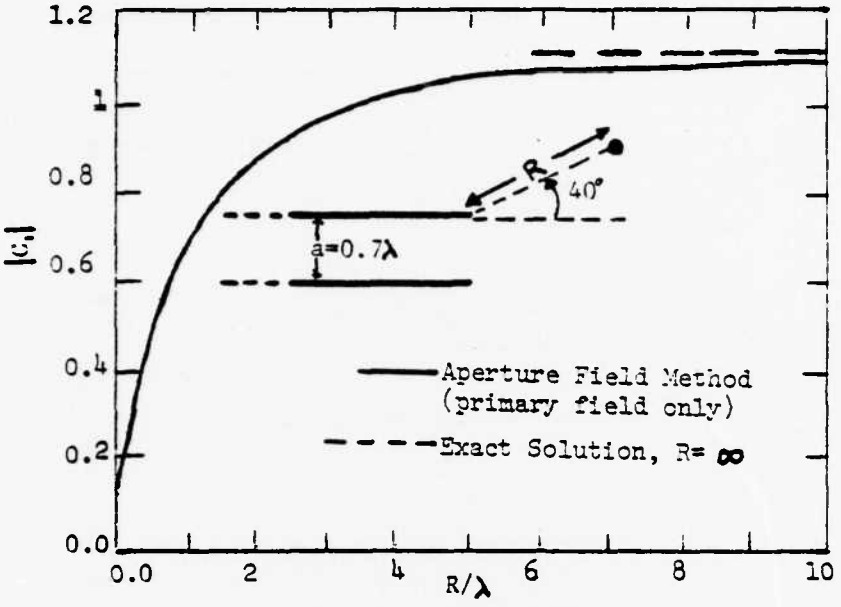

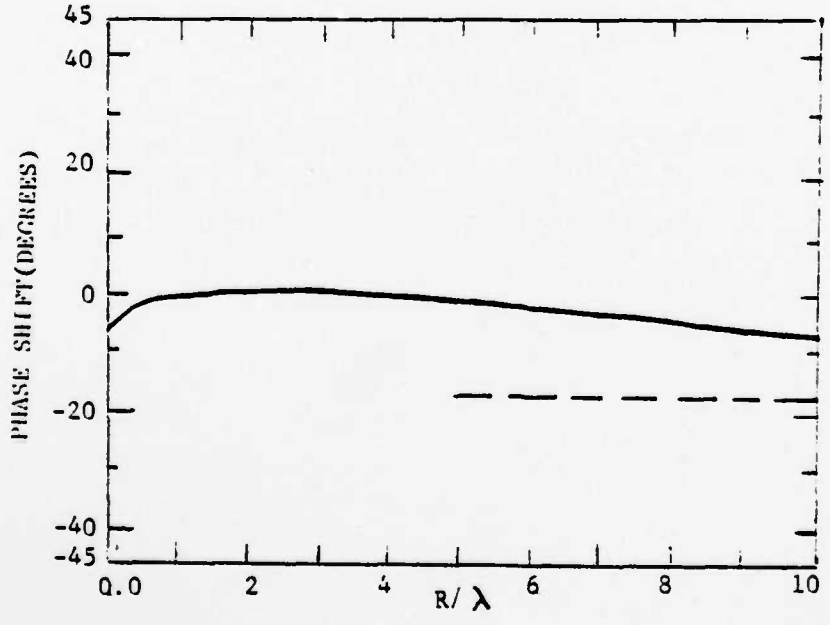

Figure 41. Magnitude and phase shift of C_1 vs. R, $\Omega_1 = -140°$, $\ell = 0$

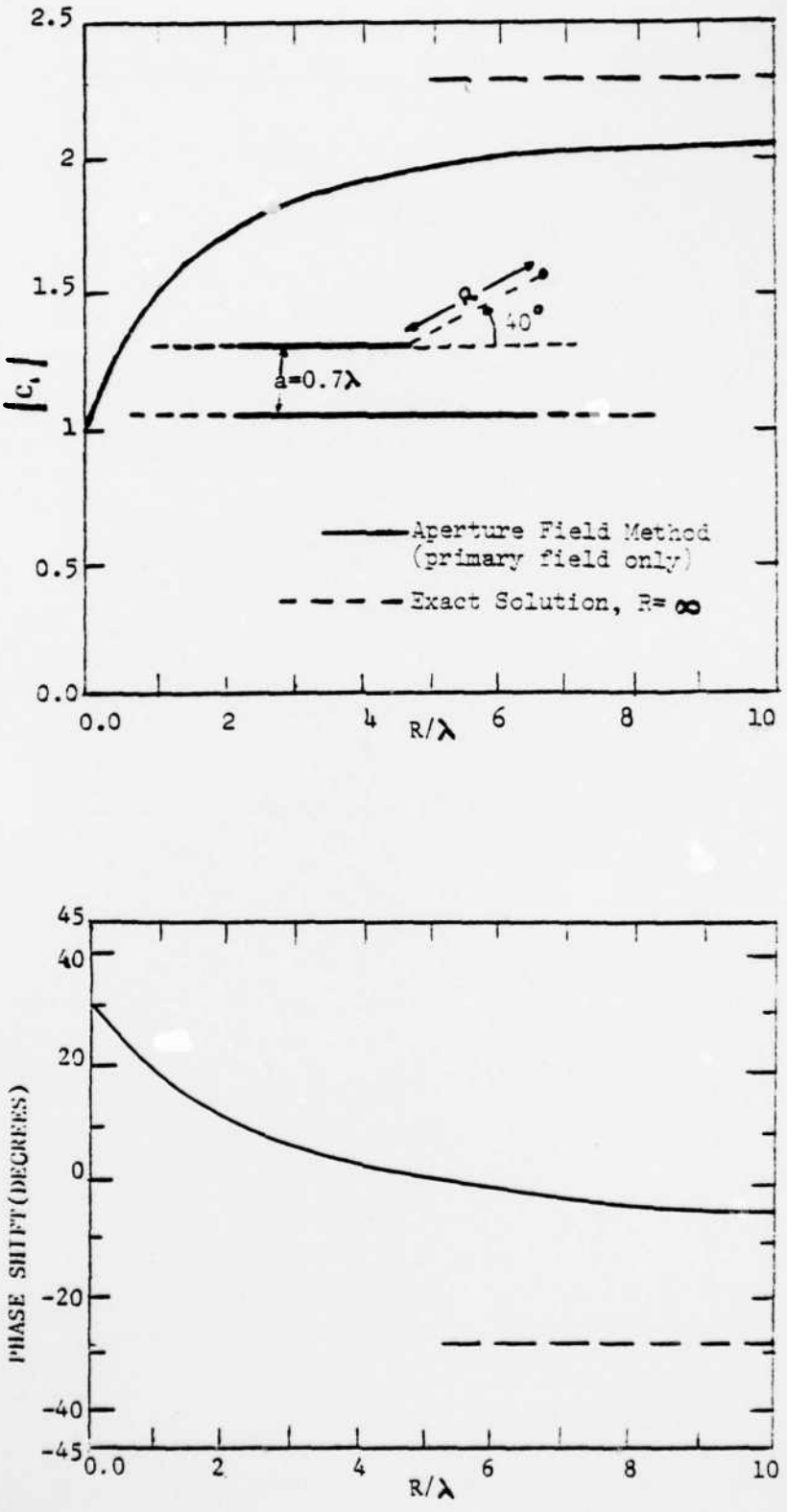

Figure 42. Magnitude and phase shift of C_1 vs. R, $\theta_1 = -140$, $\lambda = \infty$.

AD-A128 181 DIFFRACTION BY PARALLEL PLATES WITH APPLICATION TO LENS ANTENNAS(U) ILLINOIS UNIV AT URBANA ELECTROMAGNETICS LAB L GRUN ET AL. SEP 80 UIEM-80-7 NSF-ENG77-20820

2/2

UNCLASSIFIED F/G 9/5 NL

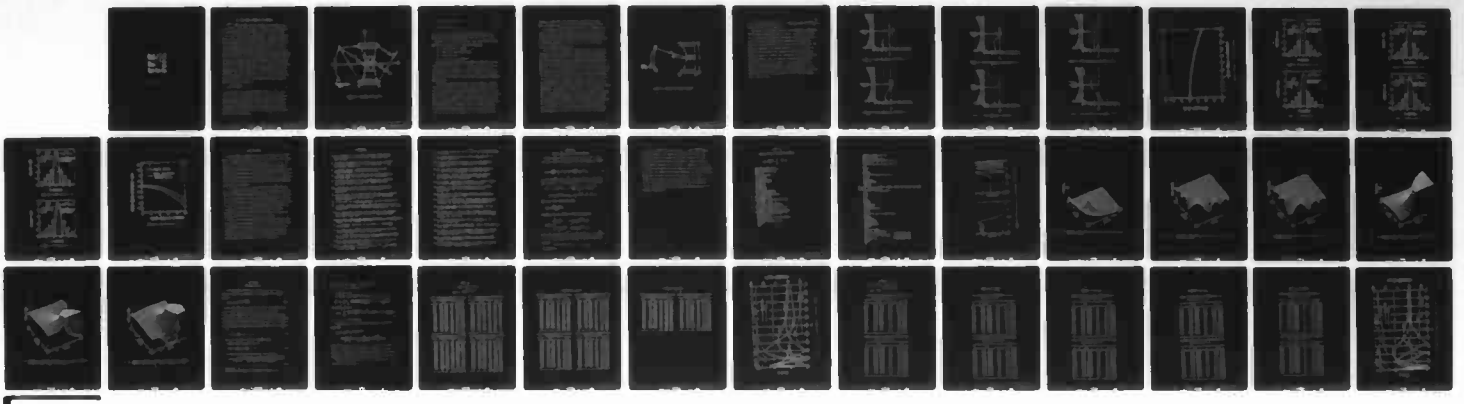

END

DATE FILMED

6-83

DTIC

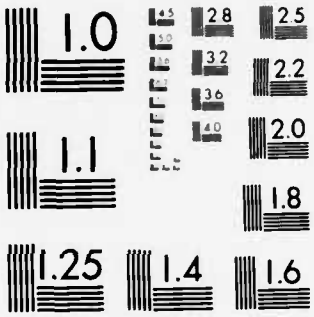

V. APPLICATION: WAVEGUIDE LENS ANTENNAS

From the onset of radio, optical techniques have been applied to meet the needs of microwave communications. The simplest and most fundamental of these problems has been the collimation of microwave energy from a point source. It was readily recognized that, as in optics, the solution was a standard lens built of dielectric material. These lenses, however, were heavy and were quickly discarded in favor of reflectors. But in 1944, Kock [18] suggested that a metal guide supporting modes can be used as a refracting medium, with its index of refraction given by λ/λ_g, where λ_g is the guide wavelength. This opened the possibility of significantly reducing weight and cost, and because of the less stringent manufacturing tolerance, the lens began to compete with other antenna designs. In 1950, Ruze [28] showed that a "constrained" lens, that is, a lens operating in the dominant TE_{10} mode, can be used for wide-angle scanning applications. Such a two-dimensional lens is shown in Figure 43. The guides are aligned along the contours Σ_1 and Σ_2 with the edges parallel to the E vector so that only the TE_{10} mode propagates. Thus, if the plate surfaces are space a apart we can define a refractive index n as

$$n = \sqrt{1 - (\lambda/2a)^2} \quad , \tag{V.1}$$

and then the phase shift through any guide of length t is $2\pi nt/\lambda$. Note that in contrast to natural dielectrics n is less than one. In analogy to dielectric lenses, the design of the waveguide lens is then obtained via standard phase-path length analysis. Figure 43 shows that for a feed at a focal point offset α degrees from the z axis and the main beam in the same direction, the three electrical path lengths FPQN, FOO'N', and FP'Q' are set equal and the equations

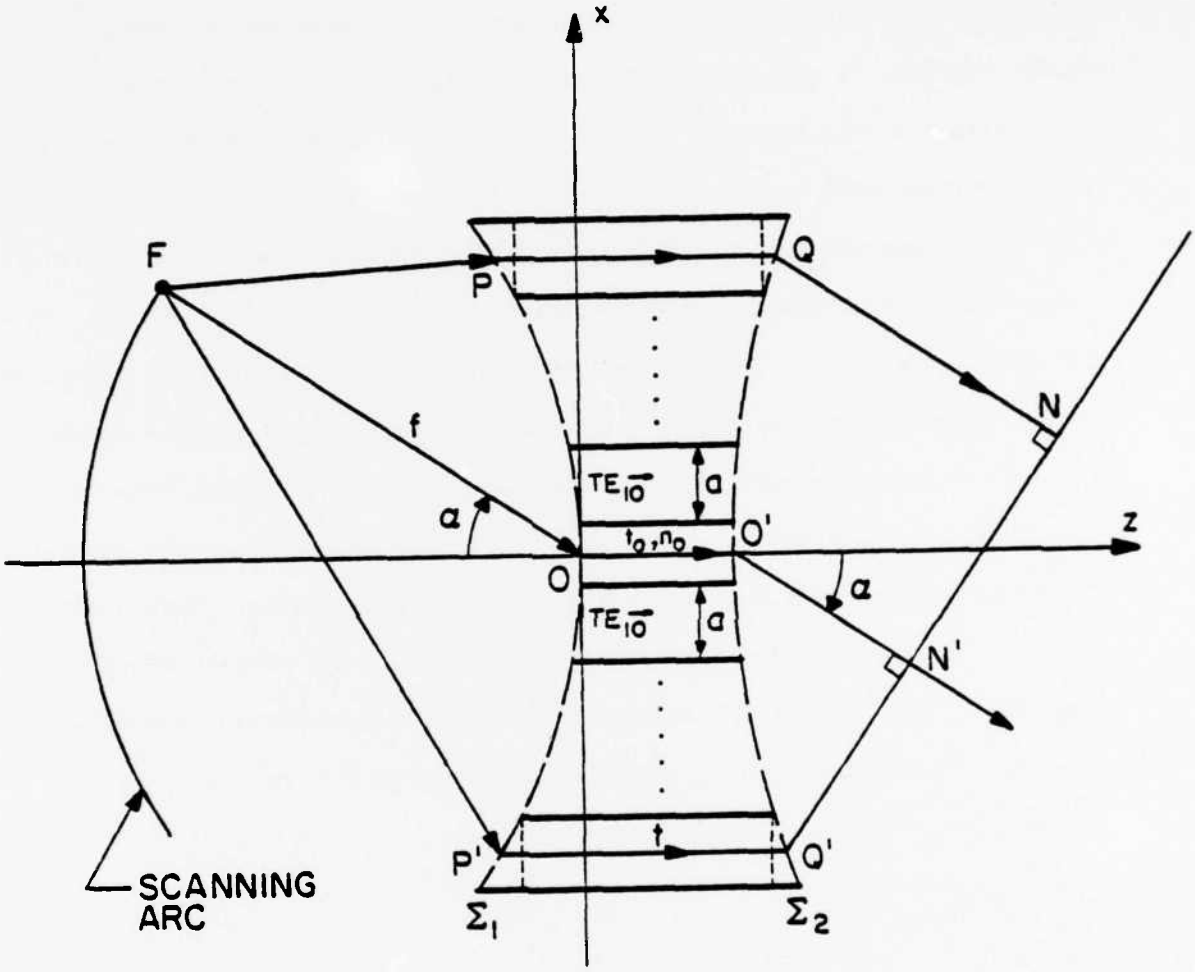

Figure 43. Wide-angle scanning lens.

$$z^2 + 2zf \cos \alpha + x^2 \cos^2 \alpha = 0 \qquad (V.2)$$

and

$$n_0 t_0 + nt + (t - t_0 + z) \cos \alpha = 0 \qquad (V.3)$$

are obtained. Equation (V.2) gives the profile of the first surface Σ_1. This is an ellipse with its major axis perpendicular to the lens axis.

Equation (V.3) is one relation between n and t and a second arbitrary relation can be chosen. Some of the commonly chosen are

(a) a lens of constant thickness

(b) a lens with a plane second surface

(c) a third focal point

(d) a constant refractive index.

There are two main features that distinguish the metal-plate lens from a dielectric lens. First, since $n < 1$, Σ_1 and Σ_2 are concave. Second, the rays in the lens are "constrained." By this it is meant that the rays in the lens always travel parallel to the z axis, regardless of the angle of incidence. It is this property that gives these lenses such good wide-angle scanning ability.

The standard design just outlined has a basic limitation. It models the region of any waveguide by a medium with index of refraction n, given by (V.1), and does not consider the actual physical structure and the scattering off the plates. It assumes that the phase shift at Σ_1 and Σ_2 is zero or very small, but more fundamentally, the design is incomplete as it cannot predict the amplitude distribution in the lens. Note that because the lens is "constrained," Snell's Law cannot be used to give even a qualitative idea of what the amplitude distribution is. What is typically done, as in a recent design by Dion and Ricardi [13], is to assume that the power

transmission coefficient at the interface of any guide is simply one. With the methods in this paper the amplitude distribution can be found.

As an example, we study the scanner in Figure 44. We choose Σ_2 to be a plane, and ignoring interactions between Σ_1 and Σ_2 and any interactions between the guides, we apply the methods of this chapter to each guide in the lens. The principles of operation of this lens are well-known [28], and the pertinent parameters are: $f = 14\ \lambda$, $d_0 = 3.5\ \lambda$, $n_0 = 0.8$, $\alpha = 18°$, $f/D = 0.95$, and number of guides = 21.

Since we have already shown that the phase shift at Σ_1 is minimal, we concentrate on the power transmission. Since the distance from the feed to any waveguide is much greater than the width of the guide, we approximate the field at each guide by a plane wave and examine the power transmission coefficient at each guide as the feed sweeps along the focal arc shown in Figure 44. The use of a plane wave allows us to include the first interaction when computing the power transmission coefficients. These power transmission coefficients are shown in Figures 45 thru 50 for six different scan angles. We observe that for small scan angles the amplitude distribution in the lens is nearly symmetrical and, except near the edges, has an additional taper of approximately 1 dB. As the scan angle increases, the distribution now becomes asymmetrical. The staggers in the lower half of the lens channel more power into the guides and those on top act to block out some of the incident field. For scan angles approaching α, the amplitude distribution becomes increasingly flat near the center of the lens with variation of approximately 2 dB near the edges. We also note that as the scan angle increases less power is coupled into the lens. This is shown in Figure 51 where we plot the efficiency at Σ_1, the ratio of the power in the lens to the incident

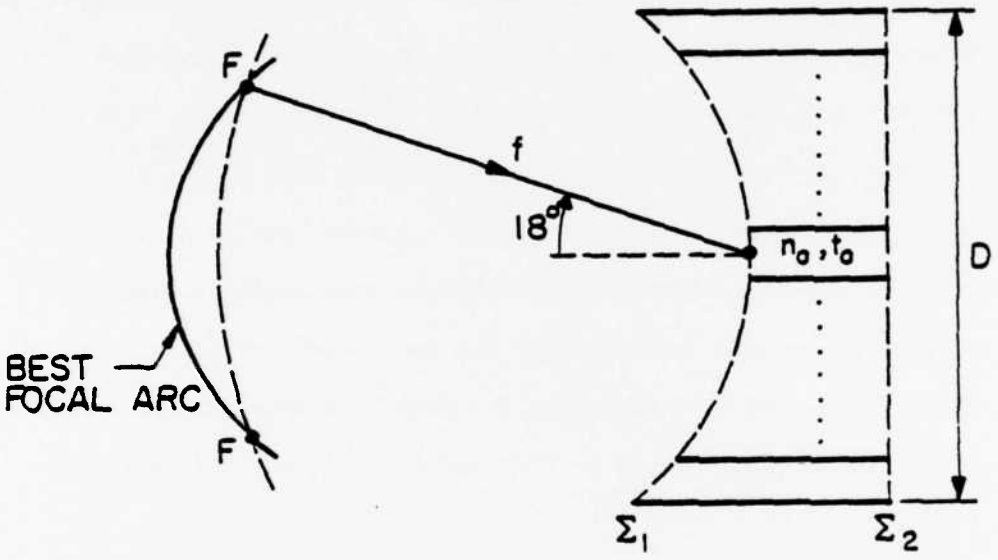

Figure 44. Straight face scanning antenna.

power, as a function of scan angle. For the scan angle $\alpha = 18°$, the efficiency is down by 0.7 dB from its maximum at $\beta = 0$.

The effects on the secondary pattern of a non-uniform power transmission thru the lens are examined in Figures 52 thru 58 . We compare the H-plane far field pattern with the amplitude distribution calculated by the methods in this thesis with the pattern given by assuming a power transmission coefficient of one through each guide, as done by Dion and Ricardi [13]. Each pattern is normalized by the maximum intensity computed by our method. We observe that the nonuniform power transmission distributions in Figures 52 through 57 result in a side-lobe level approximately 1 dB below that calculated by Dion and Ricardi. Also, the intensity of the main beam is different. The variation of the main beam strength with the scan angle is given in Figure 58. The curves are normalized by the main beam strength at $\beta = 0$, calculated by our method. We note that the main beam strength has a stronger variation than would be predicted by Dion and Ricardi, with the strength down by 1 dB at $\beta \simeq 14°$.

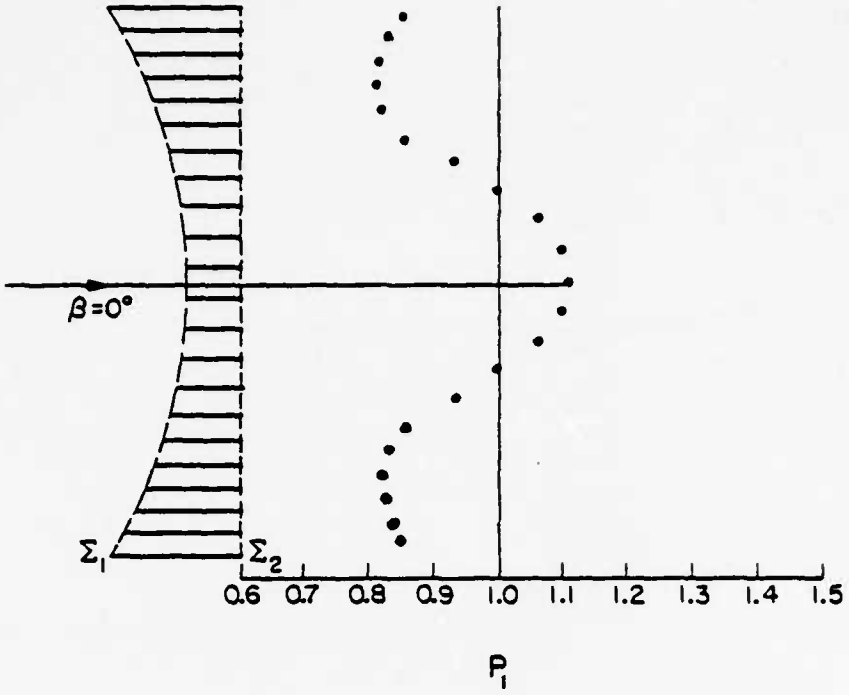

Figure 45. Power transmission coefficients, $\beta = 0°$.

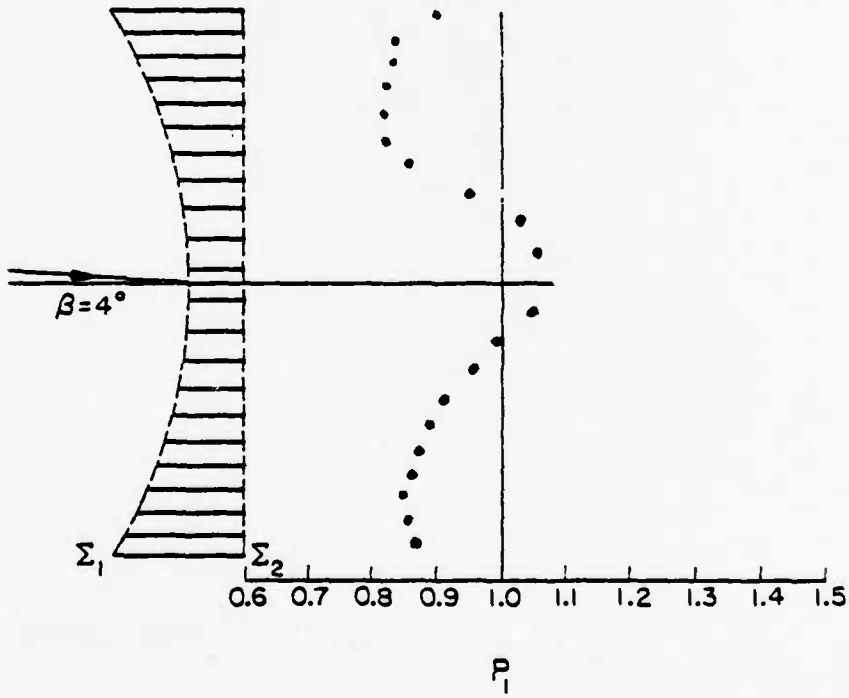

Figure 46. Power transmission coefficients, $\beta = 4°$.

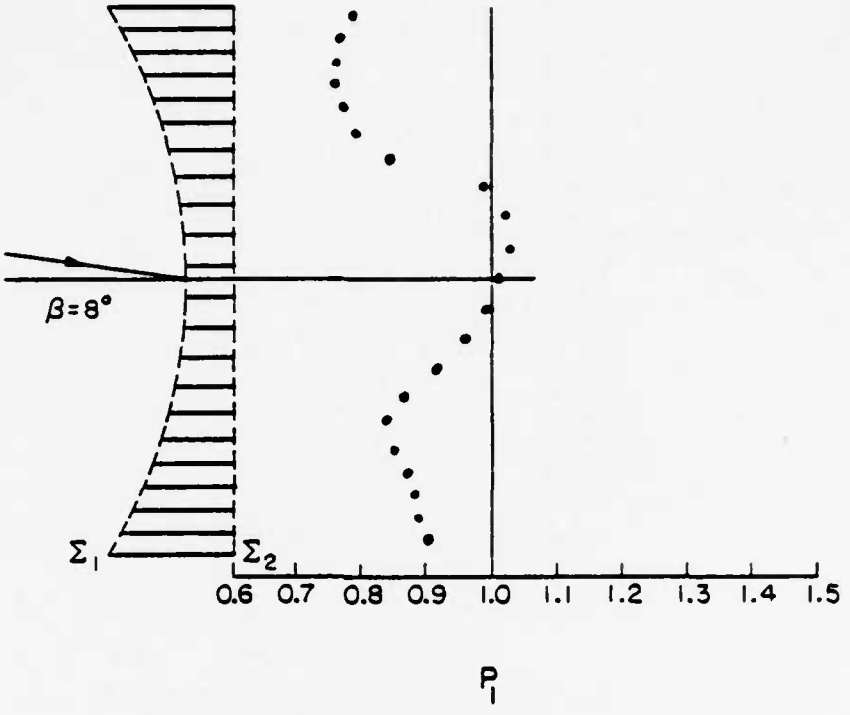

Figure 47. Power transmission coefficients, β = 8°.

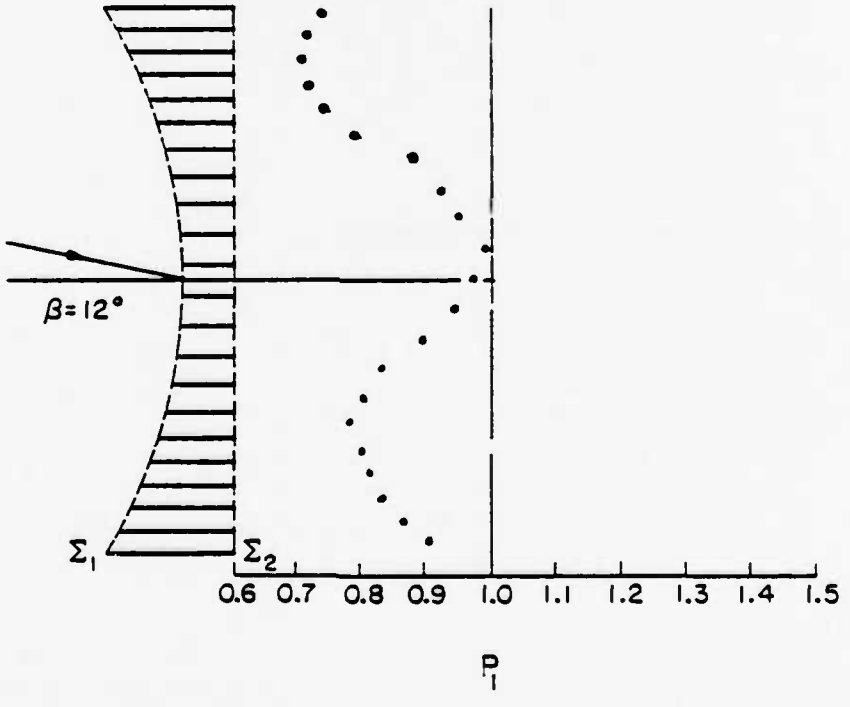

Figure 48. Power transmission coefficients, β = 12°.

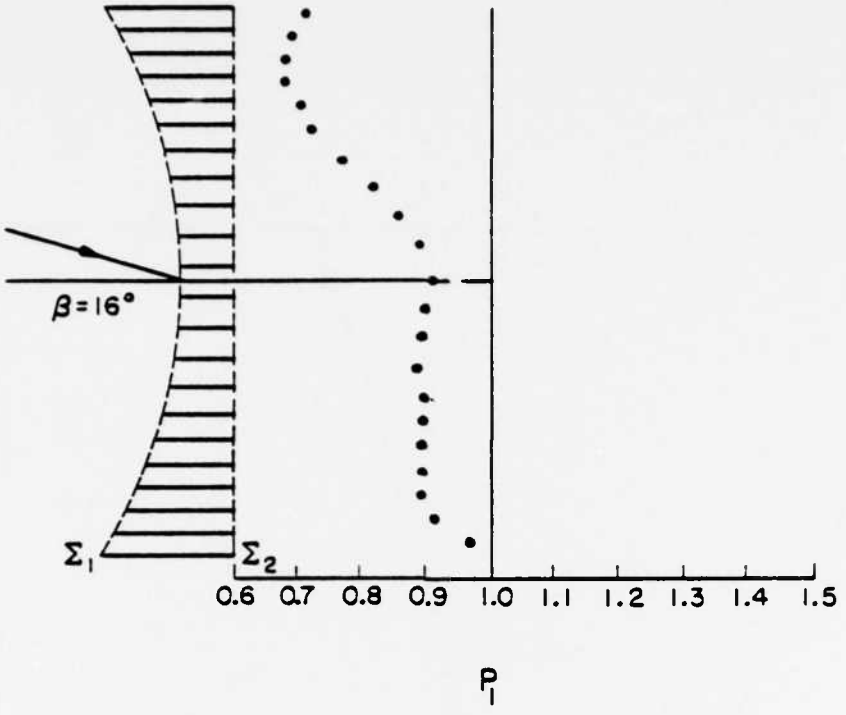

Figure 49. Power transmission coefficients, β = 16°.

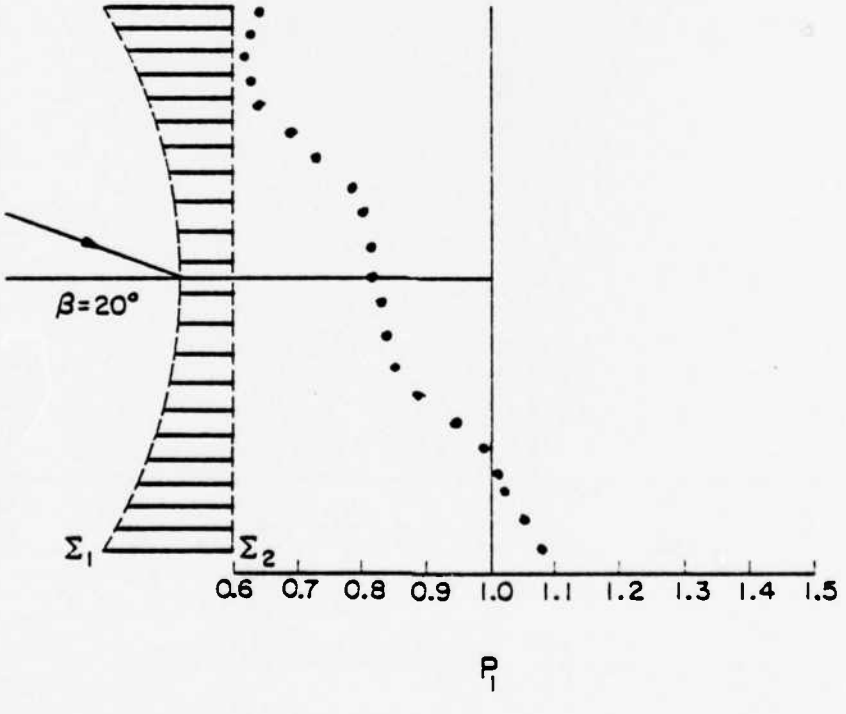

Figure 50. Power transmission coefficients, β = 20°.

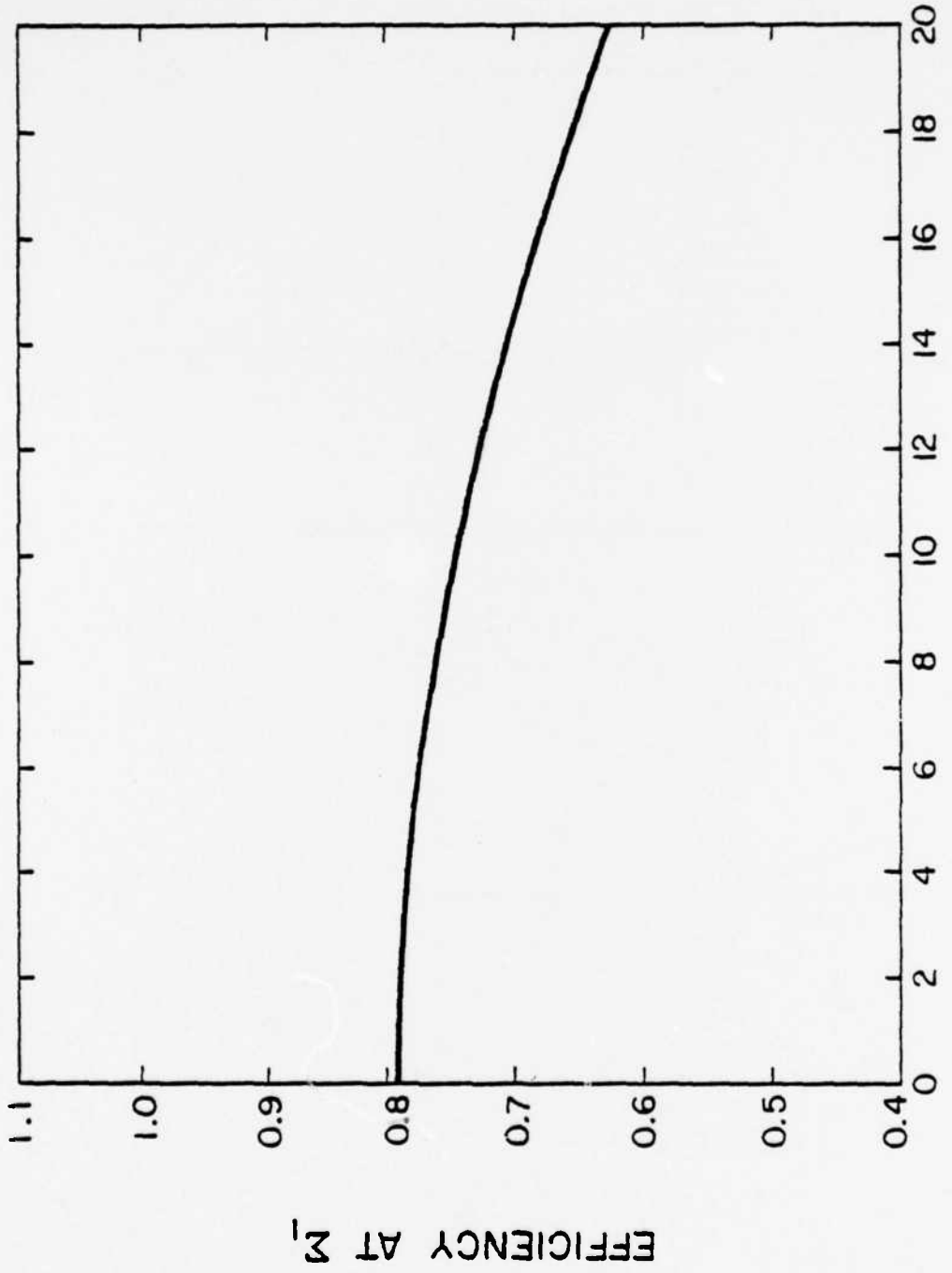

Figure 51. Efficiency at Σ_1 versus scan angle.

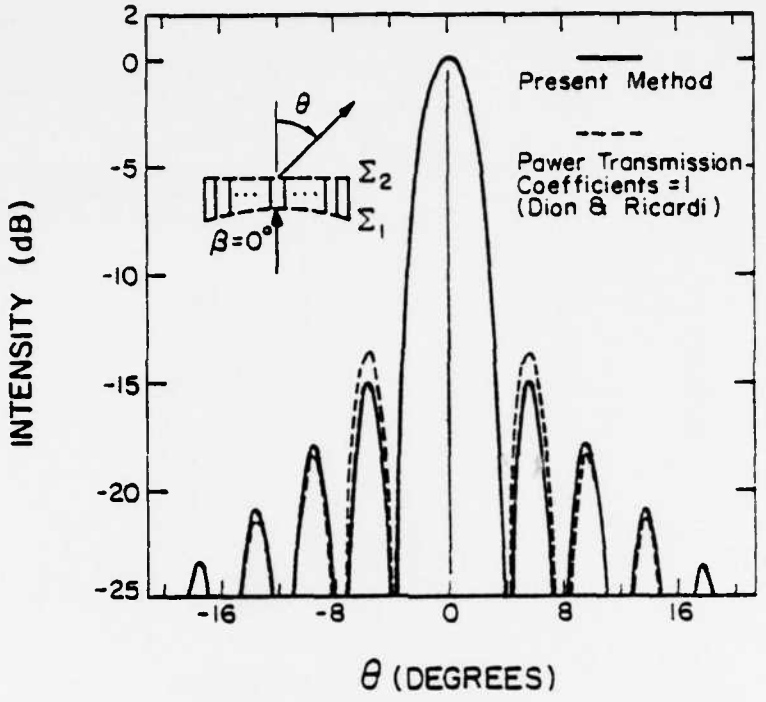

Figure 52. H-plane pattern, β = 0.

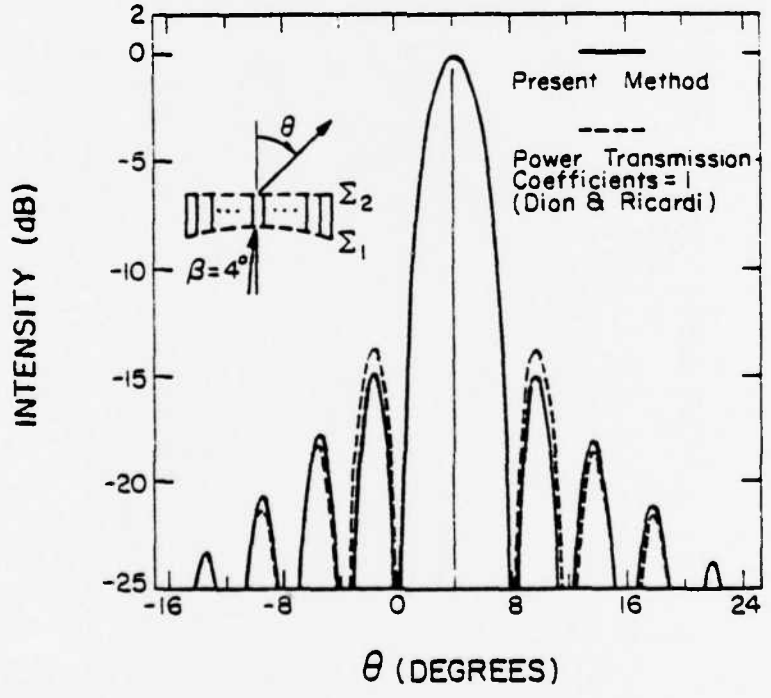

Figure 53. H-plane pattern, β = 4°.

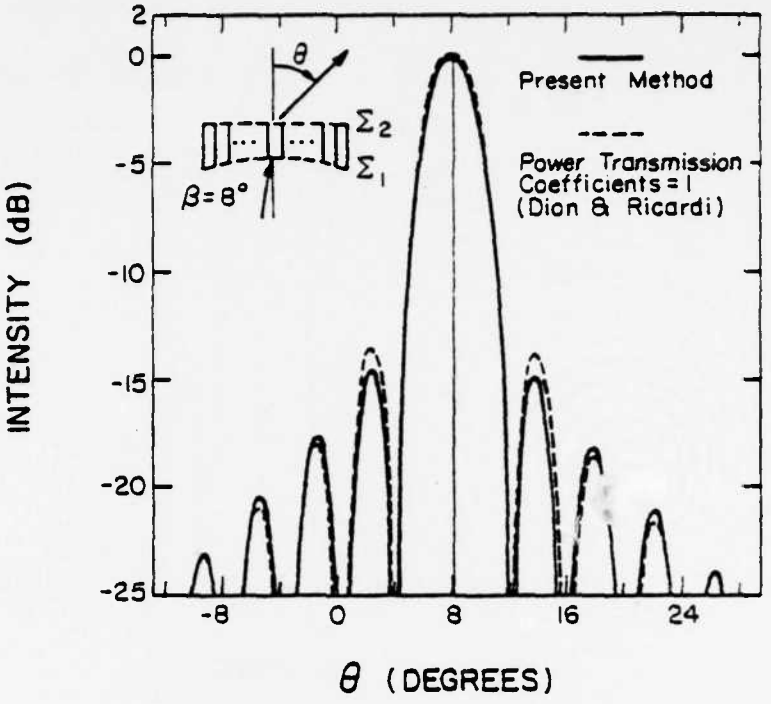

Figure 54. H-plane pattern, $\beta = 8°$.

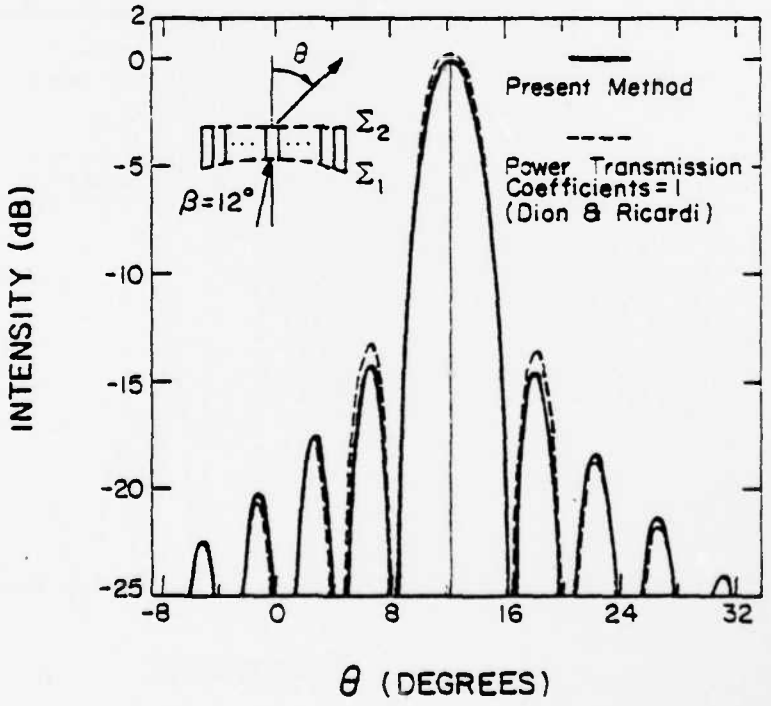

Figure 55. H-plane pattern, $\beta = 12°$.

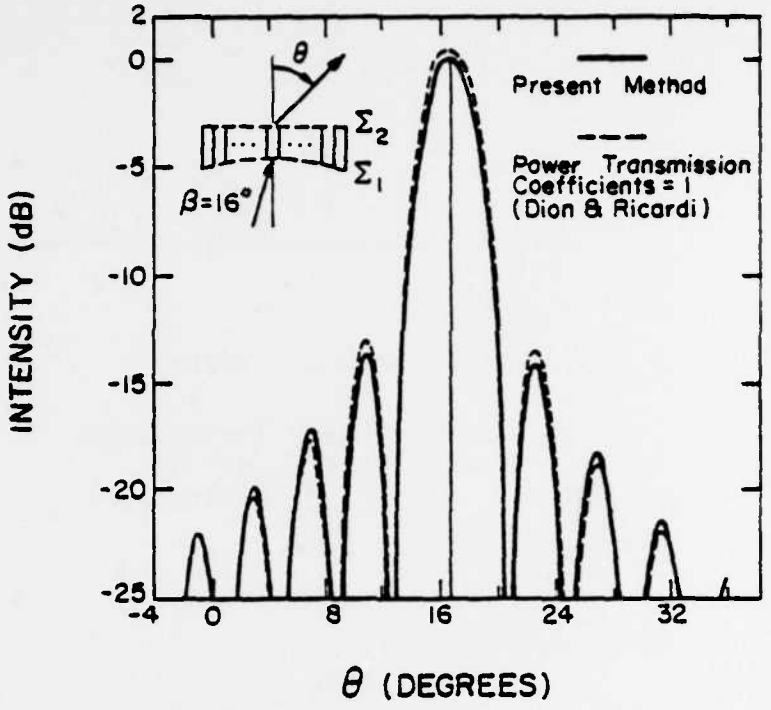

Figure 56. H-plane pattern, β = 16°.

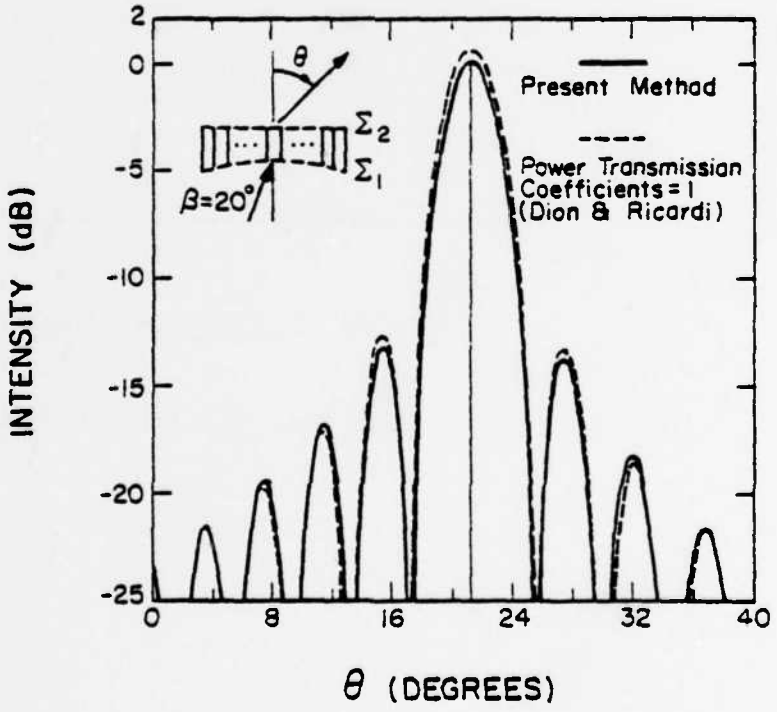

Figure 57. H-plane pattern, β = 20°.

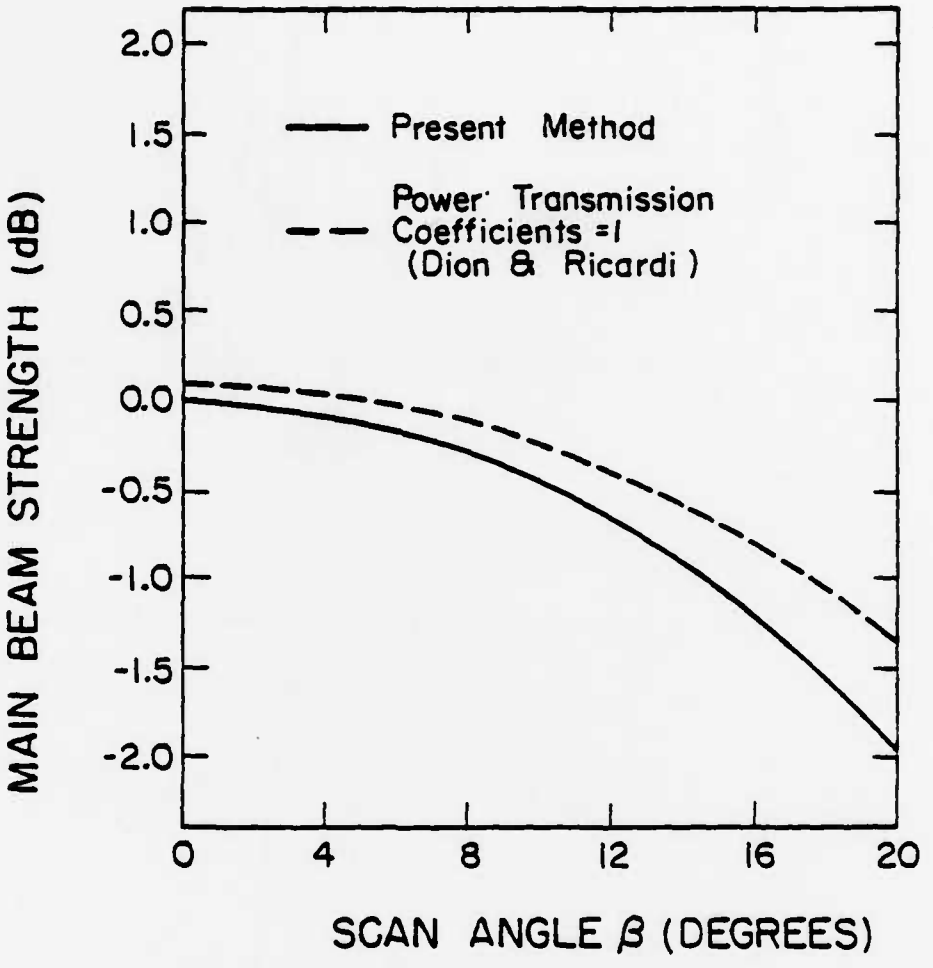

Figure 58. Main beam intensity vs. β.

VI. CONCLUSIONS

In this thesis, we examined the scattering of a plane and cylindrical wave by a staggered parallel-plate wave guide, shown in Figure 1. In particular, we concentrated on the fields in the guide for $0.5\ \lambda < a < 1\ \lambda$. In Chapter II, a quick review of some relevant techniques was given, and in Chapter III, past approaches to scattering by a parallel-plate guide were outlined and critically examined. We concluded in Chapter III that the Aperture Field Method offered the greatest accuracy and flexibility for the problem at hand. The first interaction between the plates was also exactly formulated and solved for in Chapter IV.

In Chapter IV we used the Aperture Field Method to examine the TE_{10} mode in a staggered parallel-plate guide. We gave quantitative results for the power transmission coefficient and showed that the phase shift at the aperture of the guide was very small and weakly dependent on "ℓ." Because of this weak dependence, the phase shift was well-approximated by its value at $\ell = 0$. Tables to aid in this computation are included in Appendix B. In Chapter V, we applied the Aperture Field Method to the study of waveguide lens antennas and showed how the amplitude distribution in the lens may be obtained, something previously not available.

Finally, we noted that, although we have concentrated on the TE_{10} mode and the E-wave, the same methods may be used for the H-wave problem. Also, the same aperture field formulation can be used to find the reflection coefficient for the field incident from inside the guide. One merely expresses the incident field as a sum of two plane waves and for each plane wave makes use of Equations (IV.3), (IV.6) and (IV.7).

REFERENCES

[1] D. S. Ahluwalia, R. M. Lewis, and J. Boersma, "Uniform asymptotic theory of diffraction by a plane screen," SIAM J. Appl. Math., vol. 16, 1968.

[2] J. Boersma, "Ray-optical analysis of reflection in an open-ended parallel-plane waveguide: II. TE case," Proc. IEEE, vol. 62, pp. 1475-1481, November 1974.

[3] J. Boersma, "Analysis of Weinstein's diffraction function," Philip's Res. Repts., vol. 30, pp. 161-170, 1975.

[4] J. Boersma, "Diffraction by two parallel half-planes," Quart. J. Mech. Appl. Math., vol. XXVIII, part 4, pp. 405-425, 1975.

[5] J. Boersma, "Ray-optical analysis of reflection in an open-ended parallel-plane waveguide. I: TM case," SIAM J. Appl. Math., vol. 29, pp. 164-195, July 1975.

[6] J. Boersma and S. W. Lee, "An exact solution for diffraction of a line-source field by a half-plane," J. Math. Phys., vol. 18, February 1977.

[7] J. Boersma and S. W. Lee, "High frequency diffraction of a line-source field by a half plane: Solution by ray techniques," IEEE Trans. Antennas Propagat., vol. AP-25, March 1977.

[8] M. Born and E. Wolf, Principles of Optics. New York: Macmillan, 1964.

[9] J. Bowman, "Comparison of ray theory with exact theory for scattering by an open-ended waveguide," IEEE Trans. Antennas Propagat. , pp. 131-132, January 1970.

[10] J. F. Carlson and A. E. Heins, "The reflection of an electromagnetic plane wave by an infinite set of plates, I*," Quart. Appl. Math., pp. 313-329, January 1947.

[11] P. C. Clemmow, The Plane Wave Spectrum Representation of Electromagnetic Fields. New York: Pergamon Press, 1966.

[12] G. A. Deschamps, "Ray methods in electromagnetics," Proc. IEEE, vol. 60, 1972.

[13] A. R. Dion and L. J. Ricardi, "A variable-coverage satellite antenna system," Proc. IEEE, vol. 59, no. 2, February 1971.

[14] M. J. Ehrlich, "Slot-antenna arrays," in Antenna Engineering Handbook, H. Jasik, Ed. New York: McGraw-Hill, 1961, Ch. 9.

[15] D. S. Jones, "A simplifying technique in the solution of a class of diffraction problems," Quart. J. Math., vol. 2, no. 3, 1952.

[16] D. S. Jones, "Double knife-edge diffraction and ray theory," Quart. J. Mech. Appl. Math., vol. 26, 1973.

[17] J. B. Keller, "Geometrical theory of diffraction," J. Opt. Soc. Amer., vol. 52, 1962.

[18] W. E. Kock, "Path-length microwave lenses," Proc. IRE, vol. 37, pp. 828-836, August 1947.

[19] S. W. Lee, "Ray theory of diffraction by open-ended waveguides. I. Fields in waveguides," J. Math. Phys., pp. 2830-2850, September 1970.

[20] S. W. Lee, "Ray theory of diffraction by open-ended waveguides. II. Applications," J. Math. Phys., pp. 656-664, May 1972.

[21] S. W. Lee and J. Boersma, "Ray-optical analysis of fields on shadow boundaries of two parallel plates," J. Math. Phys., vol. 16, pp. 1746-1764, September 1975.

[22] B. A. Lengyel, "Reflection and transmission at a surface of metal-plate media," J. Appl. Phys., pp. 265-276, March 1951.

[23] J. Meixner, "The behavior of electromagnetic fields at edges," Inst. Math. Res. Rept. EM-72, New York University, NY, December 1954.

[24] R. Mittra and S. W. Lee, Analytical Techniques in the Theory of Guided Waves, Macmillan Co., 1971.

[25] R. Mittra and Y. Rahmat-Samii, "A spectral domain analysis of high frequency diffraction problems" in Electromagnetic Scattering, P. Uslenghi, Ed. New York: Academic Press, 1978, Ch. 4.

[26] B. Noble, Methods Based on the Wiener-Hopf Technique. New York: Pergamon Press, 1958.

[27] R. C. Rudduck and L. L. Tsai, "Aperture reflection coefficient of TEM and TE_{01} mode parallel-plate waveguides," IEEE Trans. Antennas Propagat., vol. AP-16, 1968.

[28] J. Ruze, "Wide angle metal plate optics," Proc. IRE, vol. 38, pp. 53-59, January 1950.

[29] E. C. Titchmarsh, The Theory of Functions. Oxford: Oxford University Press, 1939.

[30] H. Y. Yee, L. B. Felsen and J. B. Keller, "Ray theory of reflection from the open end of a waveguide," SIAM J. Appl. Math., vol. 16, pp. 268-300, March 1968.

[31] L. A. Weinstein, The Theory of Diffraction and the Factorization Method, (Golem, Boulder 1969).

[32] E. A. N. Whitehead, B. A., "The theory of parallel-plate media for microwave lenses," Proc. IEE (London), vol. 98.

APPENDIX A

FRESNEL INTEGRAL WITH COMPLEX ARGUMENTS

In this appendix, some basic properties of the Fresnel integral with complex arguments are presented. The Fresnel integral is defined as

$$F(\xi) = \frac{e^{-i\pi/4}}{\sqrt{\pi}} \int_{\xi}^{\infty} e^{it^2}\, dt = \frac{1}{2} - \frac{e^{-i\pi/4}}{\sqrt{\pi}} \int_{0}^{\xi} e^{it^2}\, dt \tag{A.1}$$

where the integration path in $\int_{\xi}^{\infty}$ is any path that goes to infinity in the first quadrant. The asymptotic expansion of $F(\xi)$ may be shown as

$$F(\xi) \sim \theta[-\mathrm{Re}(\xi e^{-i\pi/4})] + e^{i\xi^2} \frac{e^{i\pi/4}}{2\pi\xi} \sum_{n=0}^{\infty} \Gamma(n + 1/2)(i\xi^2)^{-n}$$

$$= \theta[-\mathrm{Re}(\xi e^{-i\pi/4})] + \hat{F}(\xi) + O(\xi^{-3} e^{i\xi^2}) \quad \text{for} \quad |\xi| \gg 0 \tag{A.2}$$

where θ is the unit step function and

$$\hat{F}(\xi) = \frac{e^{i\xi^2 + i\pi/4}}{2\sqrt{\pi}\,\xi} \quad . \tag{A.3}$$

Furthermore, one can establish the following inequality

$$|F(\xi)| \leq \begin{cases} \frac{1}{2} |e^{i\xi^2}| & \text{when } \mathrm{Re}(\xi e^{-i\pi/4}) \geq 0 \\ 1 + \frac{1}{2} |e^{i\xi^2}| & \text{when } \mathrm{Re}(\xi e^{-i\pi/4}) < 0 \end{cases} \tag{A.4}$$

which can be derived from (A1) by introducing the change of variable $t = \tau + \xi$. Substitution of the variable $-\xi$ into (A1) allows one to arrive at

$$F(\xi) + F(-\xi) = 1, \tag{A.5}$$

for complex ξ's.

There are available some fast routines for accurate determination of the Fresnel integral (A1). Application of one of these routines (see Table A-1) allows one to evaluate $F(\xi)$ for real or complex ξ's. Some representative results are shown in this appendix. Figure A-1 is the plot of the magnitude and phase of $F(\xi)$ for real ξ's. Figures A-2, A-3 and A-4 are the three-dimensional plots of the magnitude, the real and the imaginary parts of $F(\xi)$ for complex ξ's in the first quadrant, i.e., Re $\xi \geq o$ and Im $\xi \geq o$. Figures A-5, A-6 and A-7 are the counterparts of A-2, A-4, and A-5, respectively, for complex ξ's in the fourth quadrant, i.e., Re $\xi \geq o$ and Im $\xi \leq o$. Clearly, because of (A5) the behavior of $F(\xi)$ in the third and the second quadrants is similar to its behavior in the first and the fourth quadrants, respectively.

TABLE A-1

FRESNEL INTEGRAL WITH COMPLEX ARGUMENT

$$ZFR = \frac{e^{-i\pi/4}}{\sqrt{\pi}} \int_{Z1}^{\infty} e^{it^2}\, dt$$

```
      SUBROUTINE FRNL(Z1,ZFR)
      IMPLICIT REAL*8 (A-H, O-Y)
      IMPLICIT COMPLEX*16 (Z)
      REAL*8 IM
      PI=3.1415926535DO
      ZI=(0DO,1DO)
      SQPI=DSQRT(PI)
      Z=Z1*DSQRT(2.DO/PI)
      ZW=SQPI*Z/(1.-ZI)
      X=DREAL(ZW)
      Y=DIMAG(ZW)
      ABSX=DABS(X)
      ABSY=DABS(Y)
C*    Z1ST: Z IN 1ST QUADRANT
      Z1ST=DCMPLX(ABSX,ABSY)
      CALL WOFZ(ABSX,ABSY,RE,IM)
C*    1ST QUADRANT: W(Z)
      ZFR=DCMPLX(RE,IM)
C*    3RD QUADRANT: W(-Z)=2*EXP(-Z**2)-W(Z)
      CALL UNDERZ('OFF')
      IF((X.LE.O.).AND.(Y.LE.O.))
     1ZFR=2.*CDEXP(-Z1ST*Z1ST)-ZFR
C*    4TH QUADRANT: W(CONJ(Z))=CONJ(W(-Z))
      IF((X.GE.O.).AND.(Y.LE.O.))
     IZFR=DCONJG(2.*CDEXP(-Z1ST*Z1ST)-ZFR)
C*    2ND QUADRANT: W(CONJ(-Z))=CONJ(W(Z))
      IF((X.LE.O.).AND.(Y.GE.O.))
     1ZFR=DCONJG(ZFR)
      ZFR=(1.+ZI)/2.*(1.-ZFR*CDEXP(ZW*ZW))
      CALL UNDERZ('ON')
      ZFR=.5DO-(1.DO-ZI)*ZFR/2.DO
      RETURN
      END
```

```
      SUBROUTINE WOFZ(X,Y,RE,IM)
      REAL*8 X,Y,RE,IM
      INTEGER*4 CAPN,NU,N,NP1
      REAL*8 H,H2,LAMBDA,R1,R2,S,S1,S2,T1,T2,C
      LOGICAL*4 B
      IF((Y.LT.4.29).AND.(X.LT.5.33)) GO TO 1
      H=0.
      CAPN=0
      NU=8
      GOTO 2
 1    CONTINUE
      S=(1.-Y/4.29)*DSQRT(1.-X*X/28.41)
      H=1.6*S
      H2=2.*H
      CAPN=6+23*S
      LAMBDA=H2**CAPN
      NU=9+21*S
 2    CONTINUE
C* IN THE FOLLOWING STATEMENT, LAMBDA=0 COVERS THE UNDERFLOW CASE WHERE
C* H.GT.0. IS VERY SMALL.
      B=((H.EQ.0.).OR.(LAMBDA.EQ.0.))
      R1=0.
      R2=0.
      S1=0.
      S2=0.
      N=NU
 3    CONTINUE
      NP1=N+1
      T1=Y+H+NP1*R1
      T2=X-NP1*R2
      C=0.5/(T1*T1+T2*T2)
      R1=C*T1
      R2=C*T2
      IF((H.GT.0.).AND.(N.LE.CAPN)) GOTO 4
      GOTO 5
 4    CONTINUE
      T1=LAMBDA+S1
      S1=R1*T1-R2*S2
      S2=R2*T1+R1*S2
      LAMBDA=LAMBDA/H2
 5    CONTINUE
      N=N-1
      IF(N.GE.0) GOTO 3
      IF(Y.EQ.0.) RE=DEXP(-X*X)
      IF((Y.NE.0.).AND.B) RE=          1.12837916709551*R1
      IF((Y.NE.0.).AND.(.NOT.B))RE=    1.12837916709551*S1
      IF(B) IM   =                     1.12837916709551*R2
      IF(.NOT.B) IM=                   1.12837916709551*S2
      RETURN
      END
```

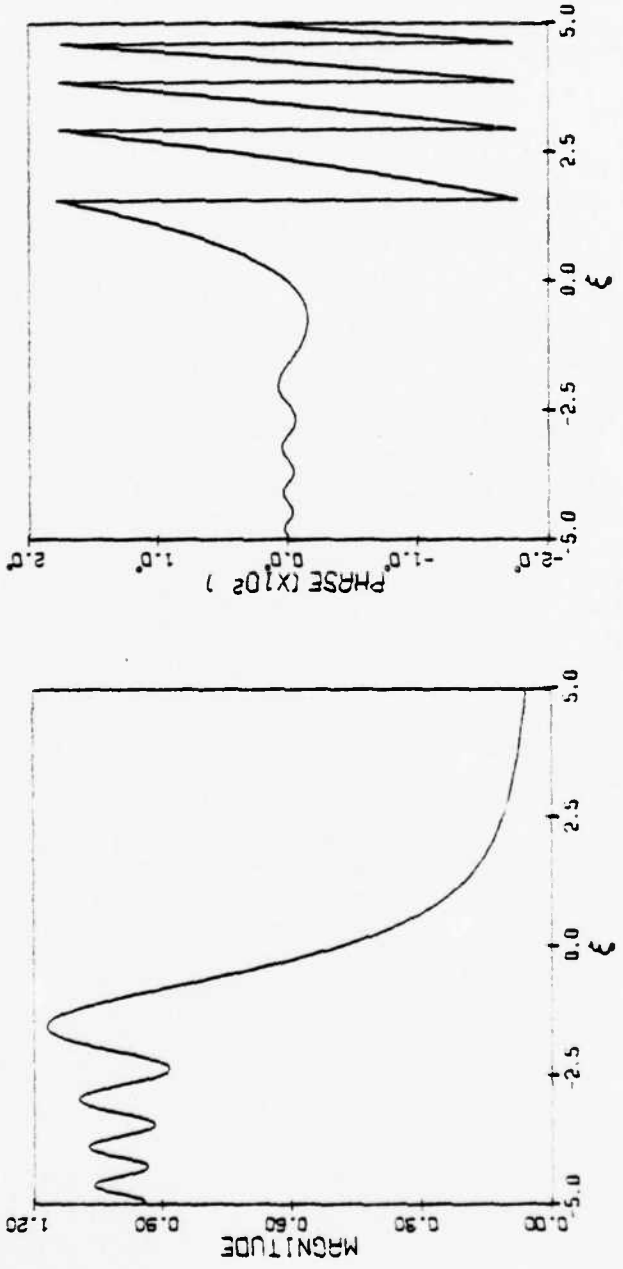

Figure A-1. Magnitude and phase of $F(\xi)$, defined in (A1), for real values of ξ.

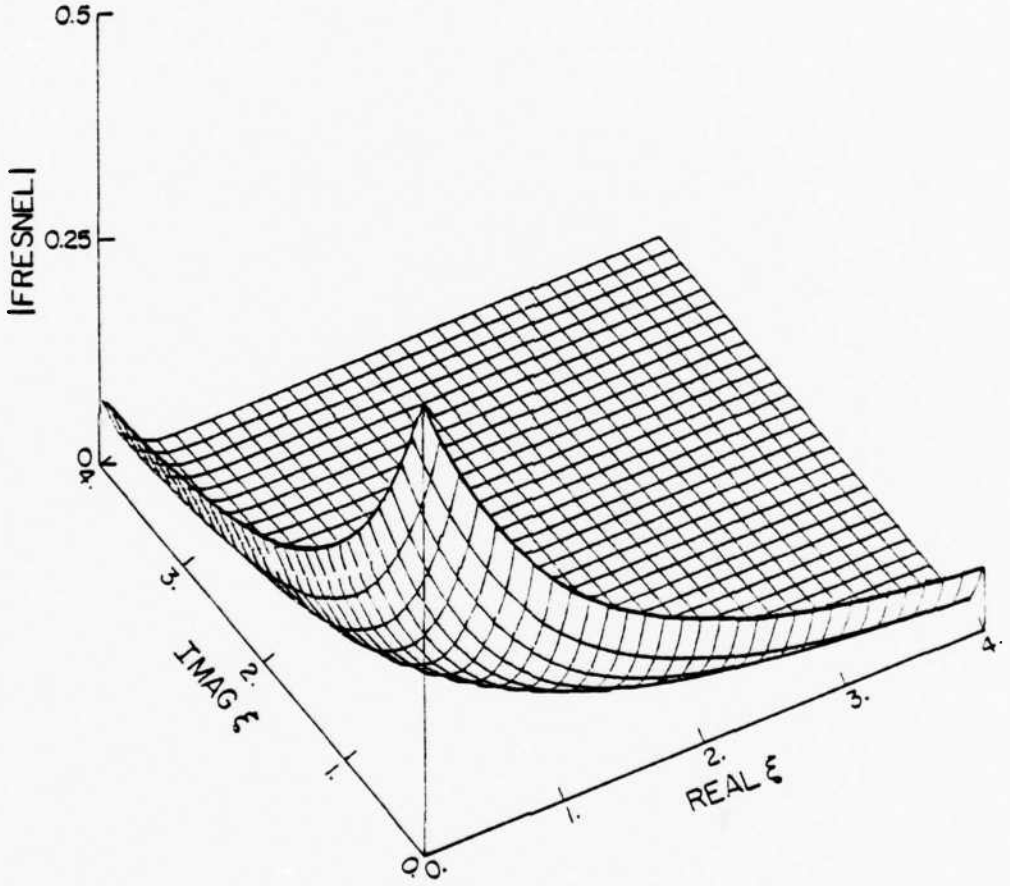

Figure A-2. Magnitude of $F(\xi)$, defined in (A1), for ξ's in the first quadrant of complex ξ-plane.

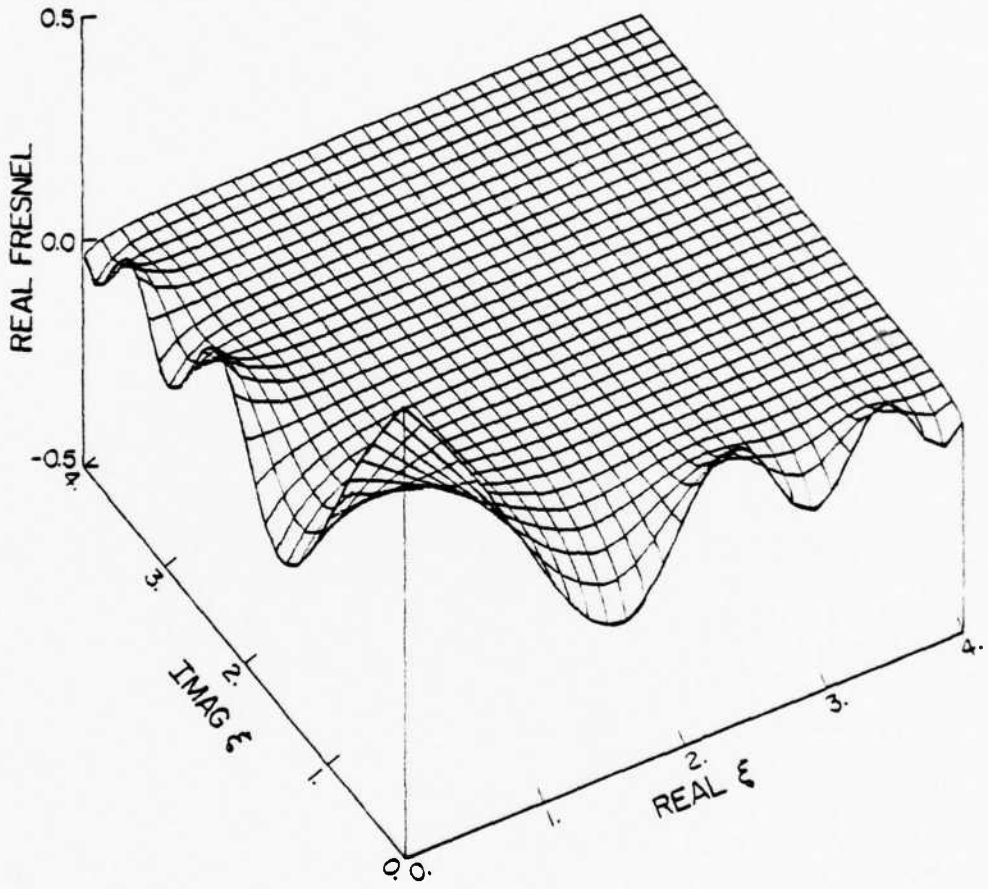

Figure A-3. Real part of $F(\xi)$, defined in (A1), for ξ's in the first quadrant of complex ξ-plane.

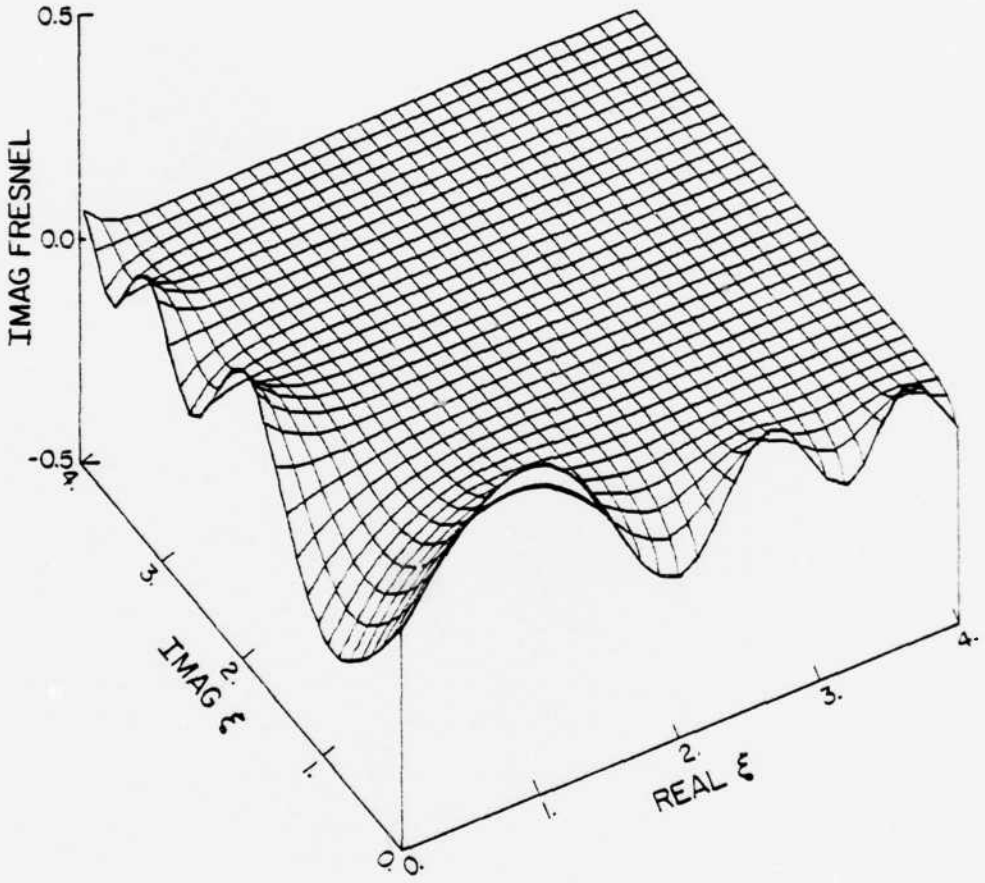

Figure A-4. Imaginary part of $F(\xi)$, defined in (A1), for ξ's in the first quadrant of complex ξ-plane.

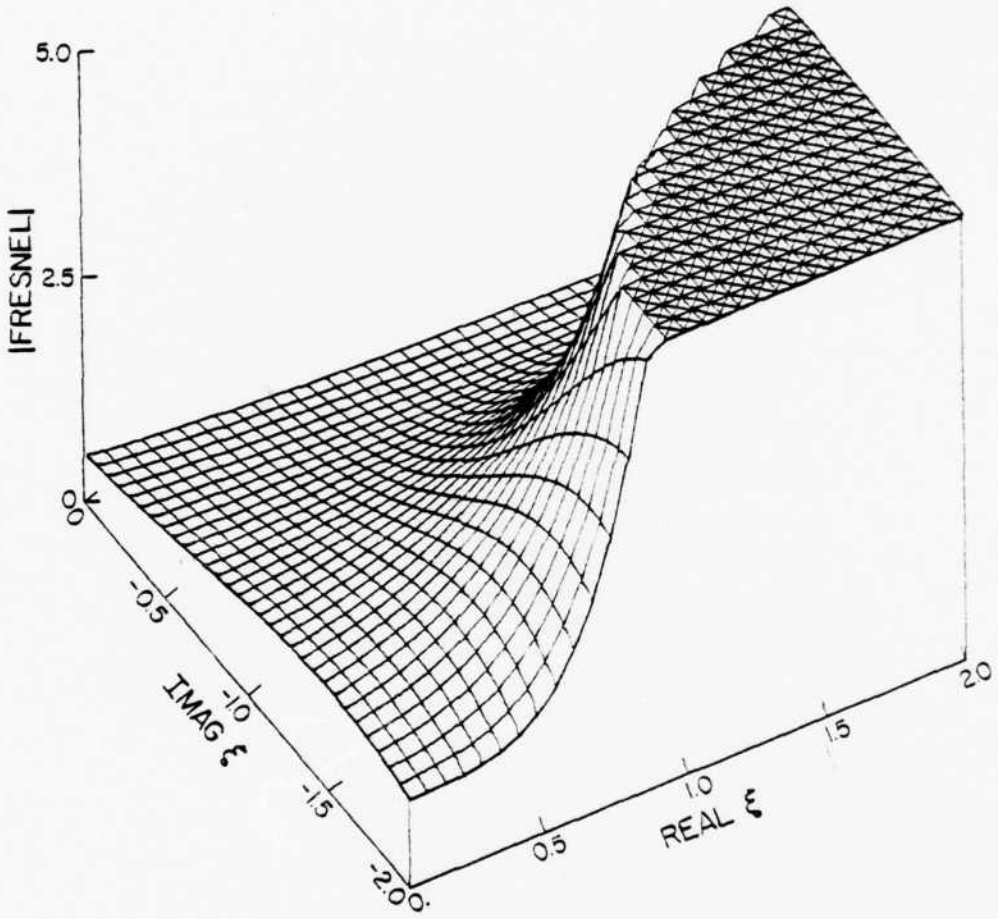

Figure A-5. Magnitude of $F(\xi)$, defined in (A1), for ξ's in the fourth quadrant of complex ξ-plane. $|F(\xi)|$ is truncated at 5.

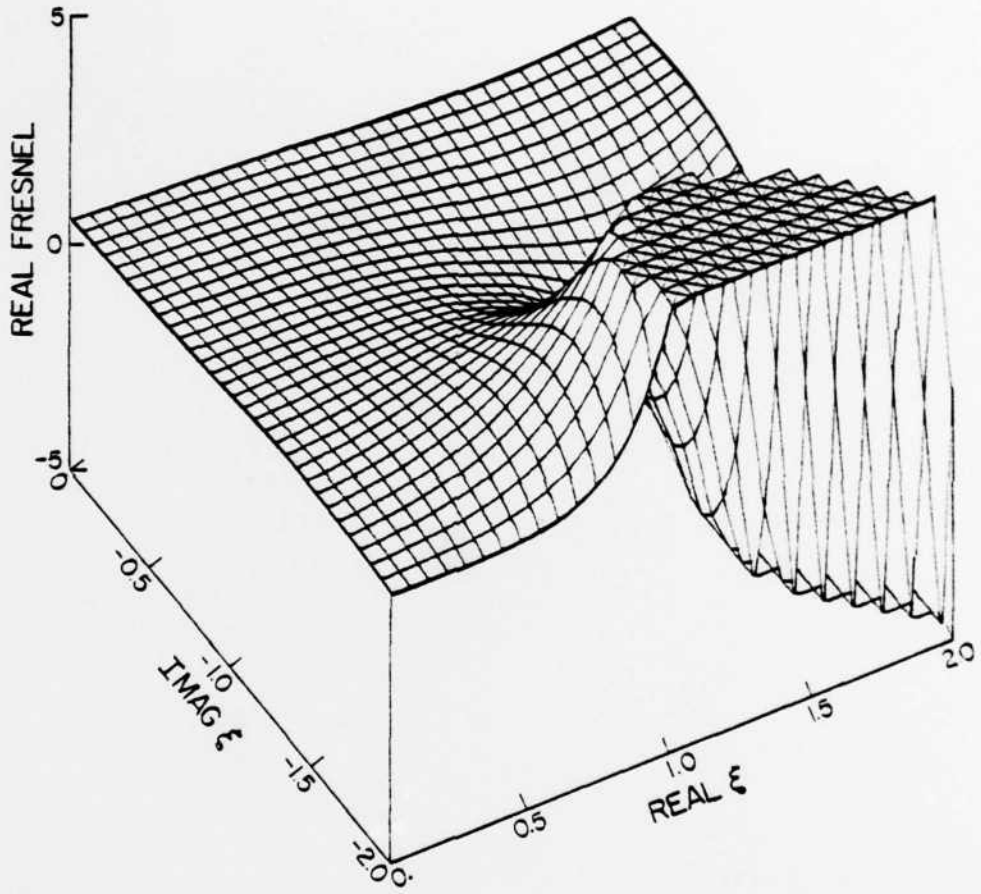

Figure A-6. Real part of $F(\xi)$, defined in (A1), for ξ's in the fourth quadrant of complex ξ-plane. Re $F(\xi)$ is truncated at -5 or 5.

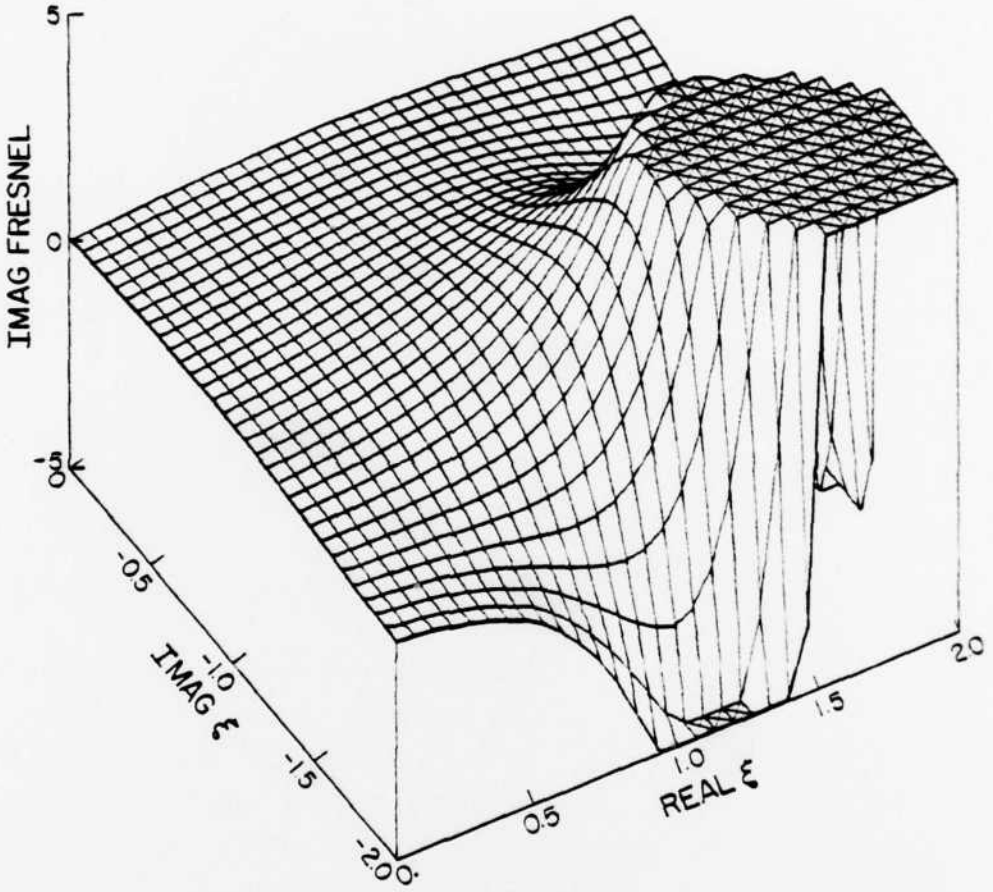

Figure A-7. Imaginary part of $F(\xi)$, defined in (A1), for ξ's in the fourth quadrant of complex ξ-plane. Im $F(\xi)$ is truncated at -5 or 5.

APPENDIX B

THE FUNCTION $G_+(\alpha)$

As illustrated in this report, a central step in the Wiener-Hopf Method as applied to the waveguide is the computation of the "plus" part of

$$G(\alpha) = 1 \mp e^{-2(\alpha^2-k^2)^{1/2}b} \quad , \tag{B.1}$$

where for the latter case (+), we say $G(\alpha) = \bar{G}(\alpha)$. One expression for $G_+(\alpha)$, already presented in Equations (III.14b) and (III.14c), is the infinite product form. For small or moderate guide dimensions, this product converges quite rapidly; however, for larger guide dimensions, the infinite product form can be very laborious. As a matter of fact, it can be shown that for truncation of the product after N terms, the error, ε, is

$$\varepsilon = [(\alpha b/\pi)^2/N] \quad \text{if} \quad \varepsilon << 1 \quad . \tag{B.2}$$

Then for αb - not small - N must be exceedingly large.

Another useful formula for $G_+(\alpha)$ is

$$G_+(\alpha) = \exp[U(\alpha/k, 2kb)] \quad \alpha > 0^1 \, , \tag{B.3}$$

where U(s,p) is the Weinstein function [21], [31], given by

$$U(s,p) = \frac{1}{2\pi i} \int_{-\infty}^{\infty} \frac{\ln(1 \mp \exp[ip - pt^2])(1 + it^2)(1 + \frac{1}{2} it^2)^{1/2} \, dt}{t(1 + \frac{1}{2} it^2) - 2^{-1/2} \, s \exp[i\pi/4]} \, , \tag{B.4}$$

[1] Equations (B.7) and (B.8) in [21] are only valid for $\alpha > 0$.

the plus in $\ln(1 \mp \exp[\cdot])$ being used for $G(\alpha) = \tilde{G}(\alpha)$.

For $\alpha < 0$, this relationship is used:

$$G_+(-\alpha)G_+(\alpha) = G(\alpha) \quad . \tag{B.5}$$

Two commonly found asymptotic expressions for $U(s,p)$ are

$$U(s,p) \sim \frac{i}{2\pi i} \int_{-\infty}^{\infty} \frac{\ln(1 \mp \exp[ip - pt^2])}{t - 2^{-1/2} s \exp[i\pi/4]} \, dt + O(p^{-1}), \text{ uniformly in } s \tag{B.6}$$

and, directly from (B.5),

$$U(s,p) \sim \sum_{n=1}^{\infty} \frac{(\mp 1)^n \exp[in(2\pi p - s^2)]}{n} F(\sqrt{ns/2}) + O(p^{-1}), \text{ uniformly in } s \tag{B.7}$$

where $F(\cdot)$ is the Fresnel integral.

By making use of a new factorization formula [19], it also may be shown that

$$G_+(\alpha) = (e^{-ikb} \mp e^{ikb})^{1/2} e^{ikb/2} \exp\left[\frac{1}{2\pi i} \int_P \ln\left\{1 \pm \frac{2\alpha b}{(s[s - 4ikb])^{1/2}}\right\} \frac{e^{2ikb}}{e^s - e^{2ikb}} \, ds\right] \tag{B.8}$$

where the path P goes from $-\infty$ to 0^+ below the real axis of s, circles around the origin, and then goes from 0^+ to $+\infty$ above the real axis. Note that the integral in (B.7) converges quite rapidly. Other asymptotic formulas for special cases may be found in the references listed above.

Tables B.1 and B.2 and Figures B.1 and B.2 give the values of $G_+(\alpha)$ for different values of kb.

TABLE B.1

Values of $G_+(kx)$, (Magnitude, Phase).

$$G(kx) = 1 - e^{-2kb(x^2-1)^{1/2}}$$

Values of $G_+(kx)$ for $kb = 1.0$

x	$G_+(kx)$	x	$G_+(kx)$
−1.00	(0.00, 0.0)	0.00	(1.30, −16.4)
−0.95	(0.50, −67.6)	0.05	(1.30, −15.3)
−0.90	(0.69, −60.2)	0.10	(1.30, −14.3)
−0.85	(0.82, −54.7)	0.15	(1.29, −13.4)
−0.80	(0.92, −50.1)	0.20	(1.29, −12.5)
−0.75	(0.99, −46.2)	0.25	(1.29, −11.7)
−0.70	(1.05, −42.8)	0.30	(1.28, −10.9)
−0.65	(1.10, −39.7)	0.35	(1.28, −10.2)
−0.60	(1.14, −36.9)	0.40	(1.27, −9.6)
−0.55	(1.18, −34.4)	0.45	(1.27, −8.9)
−0.50	(1.20, −32.0)	0.50	(1.27, −8.3)
−0.45	(1.23, −29.9)	0.55	(1.26, −7.8)
−0.40	(1.24, −27.9)	0.60	(1.25, −7.3)
−0.35	(1.26, −26.1)	0.65	(1.25, −6.8)
−0.30	(1.27, −24.4)	0.70	(1.24, −6.3)
−0.25	(1.28, −22.8)	0.75	(1.24, −5.9)
−0.20	(1.29, −21.3)	0.80	(1.23, −5.5)
−0.15	(1.29, −20.0)	0.85	(1.23, −5.1)
−0.10	(1.29, −18.7)	0.90	(1.22, −4.8)
−0.05	(1.30, −17.5)	0.95	(1.22, −4.5)
		1.00	(1.21, −4.2)

Values of $G_+(kx)$ for $kb = 2.0$

x	$G_+(kx)$	x	$G_+(kx)$
−1.00	(0.00, 0.0)	0.00	(1.35, 12.3)
−0.95	(1.12, −63.1)	0.05	(1.32, 12.6)
−0.90	(1.46, −49.3)	0.10	(1.29, 12.9)
−0.85	(1.64, −39.2)	0.15	(1.26, 13.0)
−0.80	(1.75, −31.1)	0.20	(1.23, 13.0)
−0.75	(1.81, −24.4)	0.25	(1.21, 12.9)
−0.70	(1.84, −18.7)	0.30	(1.19, 12.8)
−0.65	(1.84, −13.8)	0.35	(1.17, 12.6)
−0.60	(1.82, −9.5)	0.40	(1.15, 12.4)
−0.55	(1.79, −5.8)	0.45	(1.14, 12.1)
−0.50	(1.76, −2.6)	0.50	(1.12, 11.8)
−0.45	(1.72, 0.2)	0.55	(1.11, 11.5)
−0.40	(1.68, 2.6)	0.60	(1.10, 11.2)
−0.35	(1.63, 4.7)	0.65	(1.09, 10.9)
−0.30	(1.59, 6.5)	0.70	(1.08, 10.5)
−0.25	(1.54, 8.0)	0.75	(1.07, 10.2)
−0.20	(1.50, 9.3)	0.80	(1.06, 9.9)
−0.15	(1.46, 10.3)	0.85	(1.06, 9.5)
−0.10	(1.42, 11.2)	0.90	(1.05, 9.2)
−0.05	(1.38, 11.8)	0.95	(1.04, 8.9)
		1.00	(1.04, 8.6)

Values of $G_+(kx)$ for $kb = 3.0$

x	$G_+(kx)$	x	$G_+(kx)$
−1.00	(0.00, 0.0)	0.00	(0.53, 40.9)
−0.95	(2.11, −35.2)	0.05	(0.51, 34.6)
−0.90	(2.56, −14.1)	0.10	(0.51, 28.5)
−0.85	(2.70, 1.3)	0.15	(0.51, 23.0)
−0.80	(2.67, 13.7)	0.20	(0.52, 18.2)
−0.75	(2.56, 23.9)	0.25	(0.53, 14.2)
−0.70	(2.40, 32.5)	0.30	(0.55, 11.0)
−0.65	(2.22, 39.9)	0.35	(0.57, 8.4)
−0.60	(2.02, 46.1)	0.40	(0.59, 6.3)
−0.55	(1.82, 51.3)	0.45	(0.61, 4.6)
−0.50	(1.64, 55.6)	0.50	(0.63, 3.3)
−0.45	(1.46, 58.9)	0.55	(0.65, 2.2)
−0.40	(1.29, 61.3)	0.60	(0.67, 1.4)
−0.35	(1.14, 62.7)	0.65	(0.68, 0.7)
−0.30	(1.00, 63.0)	0.70	(0.70, 0.2)
−0.25	(0.88, 62.2)	0.75	(0.71, −0.2)
−0.20	(0.77, 60.2)	0.80	(0.73, −0.5)
−0.15	(0.69, 57.0)	0.85	(0.74, −0.8)
−0.10	(0.62, 52.5)	0.90	(0.75, −1.0)
−0.05	(0.57, 47.1)	0.95	(0.76, −1.1)
		1.00	(0.77, −1.3)

Values of $G_+(kx)$ for $kb = 3.1416$

x	$G_+(kx)$	x	$G_+(kx)$
−1.00	(0.00, 0.0)	0.00	(0.00, 135.0)
−0.95	(1.96, 162.7)	0.05	(0.08, 137.7)
−0.90	(2.35, −174.3)	0.10	(0.14, 140.3)
−0.85	(2.44, −157.2)	0.15	(0.20, 142.6)
−0.80	(2.39, −143.2)	0.20	(0.25, 144.8)
−0.75	(2.25, −131.3)	0.25	(0.30, 146.8)
−0.70	(2.08, −120.8)	0.30	(0.34, 148.7)
−0.65	(1.88, −111.6)	0.35	(0.38, 150.4)
−0.60	(1.68, −103.3)	0.40	(0.41, 152.0)
−0.55	(1.48, −95.8)	0.45	(0.44, 153.5)
−0.50	(1.28, −88.9)	0.50	(0.47, 154.8)
−0.45	(1.10, −82.7)	0.55	(0.49, 156.1)
−0.40	(0.93, −77.0)	0.60	(0.51, 157.3)
−0.35	(0.77, −71.8)	0.65	(0.53, 158.4)
−0.30	(0.63, −67.0)	0.70	(0.55, 159.4)
−0.25	(0.49, −62.5)	0.75	(0.57, 160.3)
−0.20	(0.37, −58.4)	0.80	(0.58, 161.2)
−0.15	(0.26, −54.7)	0.85	(0.60, 162.0)
−0.10	(0.16, −51.2)	0.90	(0.61, 162.8)
−0.05	(0.08, −48.0)	0.95	(0.62, 163.5)
		1.00	(0.63, 164.1)

TABLE B.1 (Continued)

Values of $G_+(kx)$ for $kb = 3.2$

x	$G_+(kx)$	x	$G_+(kx)$
−1.00	(0.00, 0.0)	0.00	(0.34, 136.7)
−0.95	(1.93, 162.7)	0.05	(0.41, 139.4)
−0.90	(2.29, −173.9)	0.10	(0.47, 141.9)
−0.85	(2.33, −156.6)	0.15	(0.52, 144.2)
−0.80	(2.23, −142.4)	0.20	(0.57, 146.4)
−0.75	(2.06, −130.2)	0.25	(0.61, 148.4)
−0.70	(1.85, −119.7)	0.30	(0.64, 150.2)
−0.65	(1.62, −110.3)	0.35	(0.68, 151.9)
−0.60	(1.39, −101.9)	0.40	(0.70, 153.4)
−0.55	(1.17, −94.3)	0.45	(0.73, 154.9)
−0.50	(0.96, −87.4)	0.50	(0.75, 156.2)
−0.45	(0.77, −81.2)	0.55	(0.77, 157.4)
−0.40	(0.59, −75.4)	0.60	(0.79, 158.6)
−0.35	(0.42, −70.1)	0.65	(0.80, 159.6)
−0.30	(0.28, −65.3)	0.70	(0.82, 160.6)
−0.25	(0.14, −60.8)	0.75	(0.83, 161.5)
−0.20	(0.02, −56.8)	0.80	(0.84, 162.4)
−0.15	(0.09, 127.0)	0.85	(0.85, 163.1)
−0.10	(0.18, 130.5)	0.90	(0.86, 163.9)
−0.05	(0.27, 133.7)	0.95	(0.87, 164.5)
		1.00	(0.87, 165.2)

Values of $G_+(kx)$ for $kb = 4.0$

x	$G_+(kx)$	x	$G_+(kx)$
−1.00	(0.00, 0.0)	0.00	(1.23, 159.6)
−0.95	(1.69, 164.7)	0.05	(1.23, 161.9)
−0.90	(1.75, −166.7)	0.10	(1.24, 163.9)
−0.85	(1.52, −145.6)	0.15	(1.23, 165.6)
−0.80	(1.19, −128.6)	0.20	(1.23, 167.2)
−0.75	(0.83, −114.2)	0.25	(1.22, 168.5)
−0.70	(0.49, −101.7)	0.30	(1.21, 169.8)
−0.65	(0.18, −90.8)	0.35	(1.21, 170.8)
−0.60	(0.10, 98.9)	0.40	(1.20, 171.7)
−0.55	(0.34, 107.5)	0.45	(1.19, 172.6)
−0.50	(0.54, 115.2)	0.50	(1.18, 173.3)
−0.45	(0.70, 122.1)	0.55	(1.17, 173.9)
−0.40	(0.84, 128.3)	0.60	(1.17, 174.5)
−0.35	(0.94, 133.9)	0.65	(1.16, 174.9)
−0.30	(1.03, 138.9)	0.70	(1.15, 175.4)
−0.25	(1.09, 143.4)	0.75	(1.14, 175.7)
−0.20	(1.14, 147.4)	0.80	(1.14, 176.1)
−0.15	(1.18, 151.0)	0.85	(1.13, 176.4)
−0.10	(1.20, 154.2)	0.90	(1.12, 176.6)
−0.05	(1.22, 157.0)	0.95	(1.12, 176.9)
		1.00	(1.11, 177.1)

Values of $G_+(kx)$ for $kb = 5.0$

x	$G_+(kx)$	x	$G_+(kx)$
−1.00	(0.00, 0.0)	0.00	(1.38, −171.8)
−0.95	(1.92, 174.0)	0.05	(1.34, −171.0)
−0.90	(1.57, −150.8)	0.10	(1.30, −170.5)
−0.85	(0.93, −125.0)	0.15	(1.26, −170.2)
−0.80	(0.27, −104.3)	0.20	(1.22, −170.2)
−0.75	(0.31, 93.0)	0.25	(1.19, −170.3)
−0.70	(0.78, 107.8)	0.30	(1.17, −170.4)
−0.65	(1.14, 120.5)	0.35	(1.15, −170.7)
−0.60	(1.40, 131.7)	0.40	(1.13, −171.0)
−0.55	(1.58, 141.4)	0.45	(1.11, −171.4)
−0.50	(1.68, 149.9)	0.50	(1.10, −171.8)
−0.45	(1.74, 157.2)	0.55	(1.09, −172.1)
−0.40	(1.75, 163.6)	0.60	(1.08, −172.5)
−0.35	(1.74, 169.1)	0.65	(1.07, −172.8)
−0.30	(1.71, 173.7)	0.70	(1.06, −173.2)
−0.25	(1.66, 177.6)	0.75	(1.06, −173.5)
−0.20	(1.61, −179.1)	0.80	(1.05, −173.8)
−0.15	(1.55, −176.5)	0.85	(1.05, −174.1)
−0.10	(1.49, −174.5)	0.90	(1.04, −174.3)
−0.05	(1.44, −172.9)	0.95	(1.04, −174.6)
		1.00	(1.04, −174.8)

Values of $G_+(kx)$ for $kb = 6.0$

x	$G_+(kx)$	x	$G_+(kx)$
−1.00	(0.00, 0.0)	0.00	(0.75, −143.1)
−0.95	(2.22, −164.6)	0.05	(0.71, −148.1)
−0.90	(1.18, −122.3)	0.10	(0.69, −153.1)
−0.85	(0.05, 88.7)	0.15	(0.68, −157.7)
−0.80	(1.06, 113.6)	0.20	(0.68, −161.7)
−0.75	(1.78, 134.4)	0.25	(0.69, −165.0)
−0.70	(2.23, 152.2)	0.30	(0.71, −167.7)
−0.65	(2.46, 167.4)	0.35	(0.72, −169.8)
−0.60	(2.51, −179.4)	0.40	(0.74, −171.6)
−0.55	(2.45, −168.0)	0.45	(0.75, −172.9)
−0.50	(2.31, −158.3)	0.50	(0.77, −174.0)
−0.45	(2.12, −150.1)	0.55	(0.78, −174.9)
−0.40	(1.92, −143.4)	0.60	(0.79, −175.6)
−0.35	(1.71, −138.1)	0.65	(0.80, −176.2)
−0.30	(1.50, −134.4)	0.70	(0.81, −176.7)
−0.25	(1.32, −132.2)	0.75	(0.82, −177.0)
−0.20	(1.15, −131.5)	0.80	(0.83, −177.4)
−0.15	(1.01, −132.4)	0.85	(0.84, −177.6)
−0.10	(0.90, −134.8)	0.90	(0.85, −177.8)
−0.05	(0.81, −138.5)	0.95	(0.85, −178.0)
		1.00	(0.86, −178.2)

TABLE B.1 (Continued)

Values of $G_+(kx)$ for $kb = 6.2832$			
x	$G_+(kx)$	x	$G_+(kx)$
−1.00	(0.00, 0.0)	0.00	(0.01, 135.0)
−0.95	(1.97, −145.5)	0.05	(0.10, 138.9)
−0.90	(0.85, −100.4)	0.10	(0.19, 142.4)
−0.85	(0.37, 113.0)	0.15	(0.26, 145.5)
−0.80	(1.31, 140.1)	0.20	(0.33, 148.3)
−0.75	(1.93, 163.0)	0.25	(0.38, 150.8)
−0.70	(2.26, −177.2)	0.30	(0.43, 153.0)
−0.65	(2.38, −159.8)	0.35	(0.47, 155.0)
−0.60	(2.33, −144.3)	0.40	(0.50, 156.8)
−0.55	(2.18, −130.5)	0.45	(0.53, 158.4)
−0.50	(1.97, −118.1)	0.50	(0.56, 159.8)
−0.45	(1.72, −106.9)	0.55	(0.58, 161.1)
−0.40	(1.47, −96.8)	0.60	(0.60, 162.3)
−0.35	(1.22, −87.8)	0.65	(0.61, 163.3)
−0.30	(0.98, −79.6)	0.70	(0.63, 164.3)
−0.25	(0.77, −72.2)	0.75	(0.64, 165.1)
−0.20	(0.57, −65.6)	0.80	(0.66, 165.9)
−0.15	(0.40, −59.6)	0.85	(0.67, 166.6)
−0.10	(0.24, −54.2)	0.90	(0.68, 167.3)
−0.05	(0.11, −49.3)	0.95	(0.68, 167.9)
		1.00	(0.69, 168.4)

Values of $G_+(kx)$ for $kb = 7.0$			
x	$G_+(kx)$	x	$G_+(kx)$
−1.00	(0.00, 0.0)	0.00	(1.15, 155.5)
−0.95	(1.50, −141.2)	0.05	(1.16, 158.7)
−0.90	(0.16, −91.4)	0.10	(1.17, 161.4)
−0.85	(0.95, 125.4)	0.15	(1.18, 163.7)
−0.80	(1.58, 155.0)	0.20	(1.17, 165.7)
−0.75	(1.80, 180.0)	0.25	(1.17, 167.4)
−0.70	(1.72, −158.5)	0.30	(1.16, 168.9)
−0.65	(1.47, −139.7)	0.35	(1.16, 170.1)
−0.60	(1.12, −123.2)	0.40	(1.15, 171.1)
−0.55	(0.75, −108.5)	0.45	(1.14, 172.0)
−0.50	(0.39, −95.5)	0.50	(1.13, 172.8)
−0.45	(0.06, −83.9)	0.55	(1.13, 173.5)
−0.40	(0.23, 106.4)	0.60	(1.12, 174.0)
−0.35	(0.47, 115.6)	0.65	(1.11, 174.5)
−0.30	(0.66, 123.7)	0.70	(1.11, 174.9)
−0.25	(0.81, 130.9)	0.75	(1.10, 175.3)
−0.20	(0.93, 137.2)	0.80	(1.10 175.6)
−0.15	(1.01, 142.8)	0.85	(1.09, 175.9)
−0.10	(1.07, 147.7)	0.90	(1.09, 176.2)
−0.05	(1.12, 151.9)	0.95	(1.08, 176.4)
		1.00	(1.08, 176.6)

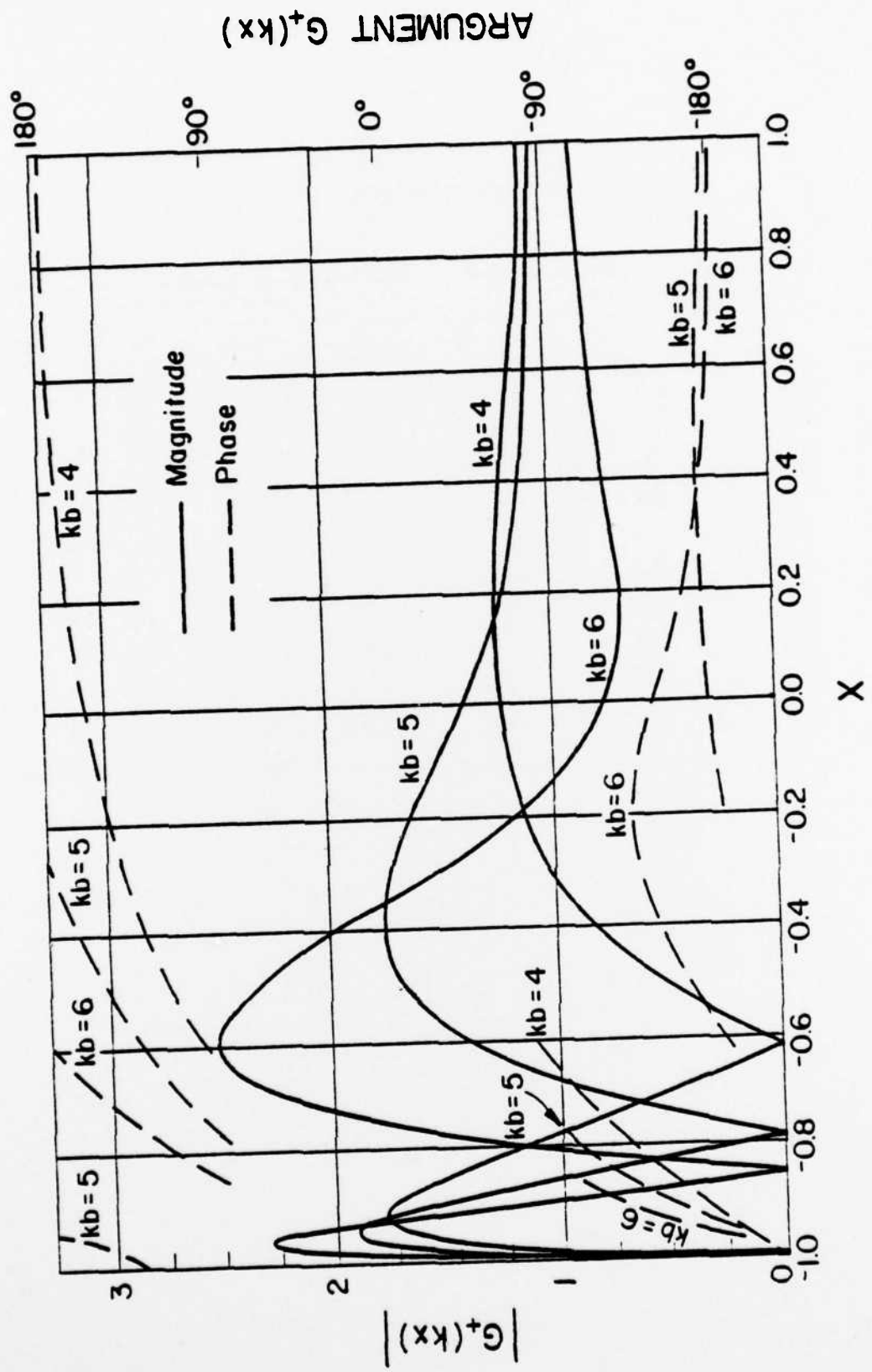

Figure B.1 Value of $G_+(kx)$: $G(kx) = 1 - \exp[-2kb(x^2 - 1)^{1/2}]$

TABLE B.2

Values of $\tilde{G}_+(kx)$, (Magnitude, Phase).

$$G(kx) = \tilde{G}(kx) = 1 + e^{-2kb(x^2-1)^{1/2}}$$

Values of $\tilde{G}_+(kx)$ for kb = 1.0

x	$\tilde{G}_+(kx)$	x	$\tilde{G}_+(kx)$
-1.00	(2.33, -12.75)	0.00	(1.04, 28.65)
-0.95	(2.22, 4.53)	0.05	(1.01, 27.94)
-0.90	(2.11, 10.98)	0.10	(0.99, 27.17)
-0.85	(2.01, 15.52)	0.15	(0.97, 26.36)
-0.80	(1.92, 19.02)	0.20	(0.96, 25.50)
-0.75	(1.83, 21.81)	0.25	(0.94, 24.63)
-0.70	(1.74, 24.07)	0.30	(0.93, 23.73)
-0.65	(1.67, 25.90)	0.35	(0.91, 22.83)
-0.60	(1.59, 27.38)	0.40	(0.90, 21.93)
-0.55	(1.53, 28.56)	0.45	(0.89, 21.04)
-0.50	(1.46, 29.46)	0.50	(0.39, 20.16)
-0.45	(1.40, 30.13)	0.55	(0.88, 19.30)
-0.40	(1.35, 30.58)	0.60	(0.87, 18.45)
-0.35	(1.30, 30.84)	0.65	(0.87, 17.64)
-0.30	(1.25, 30.92)	0.70	(0.87, 16.85)
-0.25	(1.21, 30.85)	0.75	(0.36, 16.09)
-0.20	(1.17, 30.63)	0.80	(0.86, 15.36)
-0.15	(1.13, 30.29)	0.85	(0.86, 14.66)
-0.10	(1.10, 29.84)	0.90	(0.86, 13.99)
-0.05	(1.07, 29.28)	0.95	(0.86, 13.36)
		1.00	(0.86, 12.75)

Values of $\tilde{G}_+(kx)$ for kb = 2.0

x	$\tilde{G}_+(kx)$	x	$\tilde{G}_+(kx)$
-1.00	(1.86, -168.47)	0.00	(0.91, 147.30)
-0.95	(1.51, -132.18)	0.05	(0.94, 149.21)
-0.90	(1.20, -117.47)	0.10	(0.96, 150.99)
-0.85	(0.92, -106.48)	0.15	(0.98, 152.64)
-0.80	(0.68, -97.47)	0.20	(1.00, 154.19)
-0.75	(0.46, -89.76)	0.25	(1.01, 155.62)
-0.70	(0.27, -83.01)	0.30	(1.02, 156.96)
-0.65	(0.10, -77.00)	0.35	(1.03, 158.21)
-0.60	(0.05, 108.40)	0.40	(1.04, 159.37)
-0.55	(0.19, 113.31)	0.45	(1.05, 160.43)
-0.50	(0.30, 117.78)	0.50	(1.05, 161.45)
-0.45	(0.41, 121.87)	0.55	(1.06, 162.39)
-0.40	(0.50, 125.66)	0.60	(1.06, 163.27)
-0.35	(0.58, 129.14)	0.65	(1.07, 164.09)
-0.30	(0.65, 132.35)	0.70	(1.07, 164.85)
-0.25	(0.71, 135.33)	0.75	(1.07, 165.56)
-0.20	(0.76, 138.09)	0.80	(1.07, 166.22)
-0.15	(0.81, 140.65)	0.85	(1.07, 166.84)
-0.10	(0.85, 143.03)	0.90	(1.07, 167.42)
-0.05	(0.88, 145.24)	0.95	(1.07, 167.96)
		1.00	(1.07, 168.47)

TABLE B.2 (Continued)

Values of $\bar{G}_+(kx)$ for kb = 3.0

x	$\bar{G}_+(kx)$	x	$\bar{G}_+(kx)$
-1.00	(1.79, 176.94)	0.00	(1.41, 175.94)
-0.95	(1.06, -129.43)	0.05	(1.38, 177.26)
-0.90	(0.46, -108.21)	0.10	(1.36, 178.39)
-0.85	(0.02, 87.39)	0.15	(1.34, 179.34)
-0.80	(0.40, 99.96)	0.20	(1.32, -179.86)
-0.75	(0.70, 110.53)	0.25	(1.30, -179.19)
-0.70	(0.93, 119.62)	0.30	(1.28, -178.63)
-0.65	(1.11, 127.55)	0.35	(1.26, -178.18)
-0.60	(1.24, 134.52)	0.40	(1.24, -177.82)
-0.55	(1.34, 140.69)	0.45	(1.23, -177.53)
-0.50	(1.41, 146.16)	0.50	(1.21, -177.31)
-0.45	(1.46, 151.03)	0.55	(1.20, -177.14)
-0.40	(1.49, 155.36)	0.60	(1.19, -177.01)
-0.35	(1.50, 159.20)	0.65	(1.17, -176.92)
-0.30	(1.51, 162.60)	0.70	(1.16, -176.87)
-0.25	(1.50, 165.62)	0.75	(1.15, -176.84)
-0.20	(1.49, 168.27)	0.80	(1.14, -176.83)
-0.15	(1.47, 170.60)	0.85	(1.14, -176.84)
-0.10	(1.45, 172.64)	0.90	(1.13, -176.86)
-0.05	(1.43, 174.41)	0.95	(1.12, -176.90)
		1.00	(1.12, -176.94)

Values of $\bar{G}_+(kx)$ for kb = 3.1416

x	$\bar{G}_+(kx)$	x	$\bar{G}_+(kx)$
-1.00	(1.82, 175.70)	0.00	(1.41, -180.00)
-0.95	(1.01, -128.21)	0.05	(1.39, -178.85)
-0.90	(0.36, -106.06)	0.10	(1.36, -177.91)
-0.85	(0.15, 90.19)	0.15	(1.33, -177.14)
-0.80	(0.55, 103.27)	0.20	(1.31, -176.52)
-0.75	(0.86, 114.23)	0.25	(1.28, -176.04)
-0.70	(1.09, 123.64)	0.30	(1.26, -175.67)
-0.65	(1.27, 131.82)	0.35	(1.24, -175.39)
-0.60	(1.39, 138.99)	0.40	(1.22, -175.20)
-0.55	(1.48, 145.31)	0.45	(1.21, -175.07)
-0.50	(1.53, 150.89)	0.50	(1.19, -175.00)
-0.45	(1.57, 155.82)	0.55	(1.18, -174.98)
-0.40	(1.58, 160.17)	0.60	(1.16, -174.99)
-0.35	(1.58, 164.01)	0.65	(1.15, -175.03)
-0.30	(1.57, 167.38)	0.70	(1.14, -175.09)
-0.25	(1.55, 170.32)	0.75	(1.13, -175.17)
-0.20	(1.53, 172.39)	0.80	(1.12, -175.27)
-0.15	(1.50, 175.10)	0.85	(1.12, -175.37)
-0.10	(1.47, 177.01)	0.90	(1.11, -175.48)
-0.05	(1.44, 178.63)	0.95	(1.10, -175.59)
		1.00	(1.10, -175.70)

TABLE B.2 (Continued)

Values of $\tilde{G}_+(kx)$ for kb = 3.2000

x	$\tilde{G}_+(kx)$	x	$\tilde{G}_+(kx)$
-1.00	(1.84, 175.25)	0.00	(1.41, -178.33)
-0.95	(0.99, -127.64)	0.05	(1.38, -177.26)
-0.90	(0.32, -105.11)	0.10	(1.35, -176.40)
-0.85	(0.21, 91.41)	0.15	(1.32, -175.71)
-0.80	(0.61, 104.70)	0.20	(1.30, -175.18)
-0.75	(0.93, 115.83)	0.25	(1.27, -174.78)
-0.70	(1.16, 125.36)	0.30	(1.25, -174.49)
-0.65	(1.33, 133.65)	0.35	(1.23, -174.29)
-0.60	(1.45, 140.90)	0.40	(1.21, -174.18)
-0.55	(1.53, 147.28)	0.45	(1.19, -174.12)
-0.50	(1.58, 152.90)	0.50	(1.18, -174.12)
-0.45	(1.61, 157.85)	0.55	(1.17, -174.15)
-0.40	(1.62, 162.22)	0.60	(1.15, -174.22)
-0.35	(1.61, 166.04)	0.65	(1.14, -174.32)
-0.30	(1.59, 169.39)	0.70	(1.13, -174.43)
-0.25	(1.57, 172.30)	0.75	(1.12, -174.55)
-0.20	(1.54, 174.82)	0.80	(1.11, -174.69)
-0.15	(1.51, 176.99)	0.85	(1.11, -174.83)
-0.10	(1.48, 178.83)	0.90	(1.10, -174.97)
-0.05	(1.45, -179.62)	0.95	(1.09, -175.11)
		1.00	(1.09, -175.25)

Values of $\tilde{G}_+(kx)$ for kb = 4.0

x	$\tilde{G}_+(kx)$	x	$\tilde{G}_+(kx)$
-1.00	(2.14, 173.44)	0.00	(1.14, -155.41)
-0.95	(0.68, -115.37)	0.05	(1.10, -156.33)
-0.90	(0.37, 92.56)	0.10	(1.06, -157.46)
-0.85	(1.10, 112.93)	0.15	(1.02, -158.73)
-0.80	(1.59, 129.21)	0.20	(1.00, -160.06)
-0.75	(1.89, 142.73)	0.25	(0.98, -161.41)
-0.70	(2.07, 154.19)	0.30	(0.96, -162.73)
-0.65	(2.15, 164.00)	0.35	(0.95, -163.99)
-0.60	(2.15, 172.42)	0.40	(0.94, -165.18)
-0.55	(2.11, 179.64)	0.45	(0.94, -166.29)
-0.50	(2.04, -174.22)	0.50	(0.93, -167.31)
-0.45	(1.94, -169.04)	0.55	(0.93, -168.23)
-0.40	(1.84, -164.77)	0.60	(0.93, -169.07)
-0.35	(1.73, -161.32)	0.65	(0.93, -169.84)
-0.30	(1.62, -158.65)	0.70	(0.93, -170.52)
-0.25	(1.52, -156.69)	0.75	(0.93, -171.14)
-0.20	(1.43, -155.39)	0.80	(0.93, -171.70)
-0.15	(1.34, -154.68)	0.85	(0.93, -172.20)
-0.10	(1.27, -154.50)	0.90	(0.93, -172.66)
-0.05	(1.20, -154.77)	0.95	(0.93, -173.07)
		1.00	(0.94, -173.44)

TABLE B.2 (Continued)

Values of $\tilde{G}_+(kx)$ for kb = 5.0

x	$\tilde{G}_+(kx)$	x	$\tilde{G}_+(kx)$
-1.00	(1.96, -170.85)	0.00	(0.75, 143.24)
-0.95	(0.02, -80.95)	0.05	(0.81, 146.42)
-0.90	(1.12, 134.96)	0.10	(0.85, 149.28)
-0.85	(1.72, 161.53)	0.15	(0.88, 151.85)
-0.80	(1.95, -176.90)	0.20	(0.91, 154.15)
-0.75	(1.94, -158.66)	0.25	(0.94, 156.21)
-0.70	(1.79, -142.84)	0.30	(0.95, 158.06)
-0.65	(1.57, -128.94)	0.35	(0.97, 159.71)
-0.60	(1.30, -116.59)	0.40	(0.98, 161.20)
-0.55	(1.02, -105.55)	0.45	(0.99, 162.53)
-0.50	(0.75, -95.63)	0.50	(1.00, 163.73)
-0.45	(0.49, -86.70)	0.55	(1.00, 164.80)
-0.40	(0.26, -78.64)	0.60	(1.01, 165.77)
-0.35	(0.06, -71.36)	0.65	(1.01, 166.64)
-0.30	(0.12, 115.22)	0.70	(1.01, 167.43)
-0.25	(0.27, 121.17)	0.75	(1.02, 168.14)
-0.20	(0.41, 126.34)	0.80	(1.02, 168.79)
-0.15	(0.52, 131.39)	0.85	(1.02, 169.38)
-0.10	(0.61, 135.76)	0.90	(1.02, 169.92)
-0.05	(0.69, 139.70)	0.95	(1.02, 170.41)
		1.00	(1.02, 170.85)

Values of $\tilde{G}_+(kx)$ for kb = 6.0

x	$\tilde{G}_+(kx)$	x	$\tilde{G}_+(kx)$
-1.00	(1.84, 178.59)	0.00	(1.39, 171.89)
-0.95	(0.54, 105.91)	0.05	(1.36, 173.94)
-0.90	(1.57, 148.39)	0.10	(1.33, 175.62)
-0.85	(1.81, 179.63)	0.15	(1.31, 176.98)
-0.80	(1.61, -155.21)	0.20	(1.28, 178.07)
-0.75	(1.21, -134.08)	0.25	(1.26, 178.93)
-0.70	(0.74, -115.94)	0.30	(1.24, 179.61)
-0.65	(0.27, -100.15)	0.35	(1.22, -179.87)
-0.60	(0.15, 93.70)	0.40	(1.20, -179.47)
-0.55	(0.51, 105.90)	0.45	(1.19, -179.17)
-0.50	(0.79, 116.67)	0.50	(1.17, -178.95)
-0.45	(1.02, 126.17)	0.55	(1.16, -178.79)
-0.40	(1.18, 134.54)	0.60	(1.15, -178.68)
-0.35	(1.29, 141.90)	0.65	(1.14, -178.60)
-0.30	(1.37, 148.33)	0.70	(1.13, -178.56)
-0.25	(1.41, 153.92)	0.75	(1.12, -178.53)
-0.20	(1.43, 158.76)	0.80	(1.11, -178.53)
-0.15	(1.43, 162.90)	0.85	(1.11, -178.53)
-0.10	(1.43, 166.43)	0.90	(1.10, -178.54)
-0.05	(1.41, 168.40)	0.95	(1.09, -178.56)
		1.00	(1.09, -178.59)

TABLE B.2 (Continued)

Values of $\bar{G}_+(kx)$ for kb = 6.2832

x	$\bar{G}_+(kx)$	x	$\bar{G}_+(kx)$
-1.00	(1.88, 176.73)	0.00	(1.41, -180.00)
-0.95	(0.71, 109.01)	0.05	(1.37, -178.46)
-0.90	(1.71, 153.38)	0.10	(1.33, -177.30)
-0.85	(1.83, -174.04)	0.15	(1.30, -176.46)
-0.80	(1.49, -147.83)	0.20	(1.27, -175.87)
-0.75	(0.97, -125.87)	0.25	(1.24, -175.48)
-0.70	(0.41, -107.05)	0.30	(1.21, -175.26)
-0.65	(0.11, 89.28)	0.35	(1.19, -175.15)
-0.60	(0.55, 103.55)	0.40	(1.17, -175.14)
-0.55	(0.90, 116.07)	0.45	(1.15, -175.19)
-0.50	(1.17. 127.05)	0.50	(1.14, -175.28)
-0.45	(1.36, 136.68)	0.55	(1.13, -175.41)
-0.40	(1.48, 143.08)	0.60	(1.12, -175.55)
-0.35	(1.55, 152.38)	0.65	(1.11, -175.70)
-0.30	(1.58, 158.68)	0.70	(1.10, -175.86)
-0.25	(1.58, 164.05)	0.75	(1.09, -176.01)
-0.20	(1.57, 168.59)	0.80	(1.08, -176.17)
-0.15	(1.54, 172.38)	0.85	(1.08, -176.32)
-0.10	(1.50, 175.50)	0.90	(1.07, -176.46)
-0.05	(1.46, 178.01)	0.95	(1.07, -176.60)
		1.00	(1.07, -176.73)

Values of $\bar{G}_+(kx)$ for kb = 7.0

x	$\bar{G}_+(kx)$	x	$\bar{G}_+(kx)$
-1.00	(2.06, 174.89)	0.00	(1.23, -159.46)
-0.95	(1.19, 119.85)	0.05	(1.17, -160.06)
-0.90	(2.05, 169.13)	0.10	(1.12, -161.01)
-0.85	(1.76, -154.76)	0.15	(1.08, -162.18)
-0.80	(1.01, -125.77)	0.20	(1.05, -163.45)
-0.75	(0.17, -101.56)	0.25	(1.02, -164.74)
-0.70	(0.58, 99.10)	0.30	(1.01, -165.98)
-0.65	(1.18, 116.93)	0.35	(0.99, -167.15)
-0.60	(1.60, 132.39)	0.40	(0.98, -168.23)
-0.55	(1.87, 145.80)	0.45	(0.98, -169.20)
-0.50	(2.00, 157.41)	0.50	(0.97, -170.07)
-0.45	(2.04, 167.37)	0.55	(0.97, -170.84)
-0.40	(2.01, 175.82)	0.60	(0.97, -171.53)
-0.35	(1.94, -177.14)	0.65	(0.97, -172.14)
-0.30	(1.84, -171.42)	0.70	(0.97, -172.68)
-0.25	(1.72, -166.93)	0.75	(0.97, -173.16)
-0.20	(1.61, -163.58)	0.80	(0.97, -173.58)
-0.15	(1.49, -161.29)	0.85	(0.97, -173.97)
-0.10	(1.39, -159.93)	0.90	(0.97, -174.31)
-0.05	(1.30, -159.37)	0.95	(0.97, -174.61)
		1.00	(0.97, -174.89)

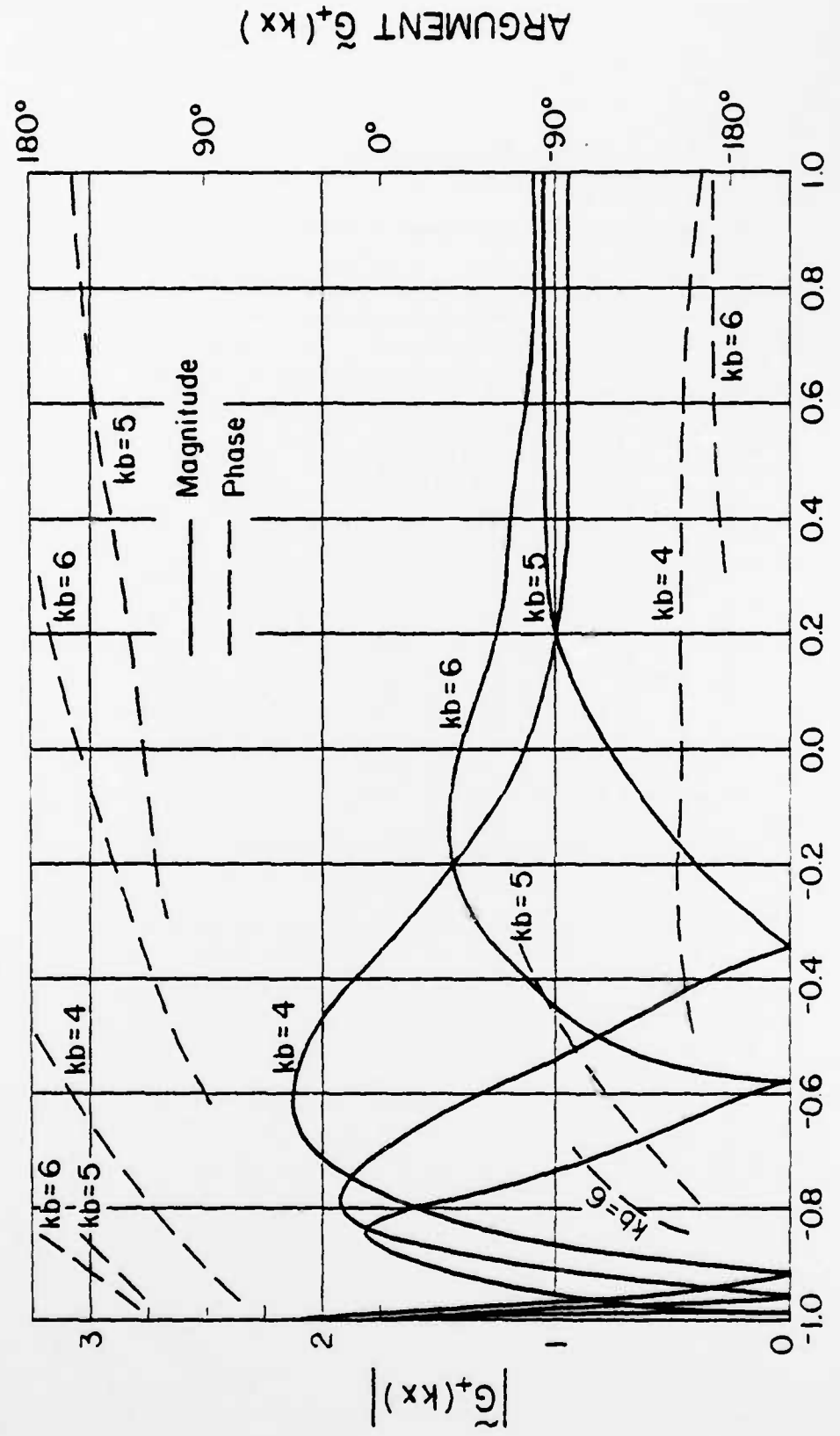

Figure B.2 Value of $\tilde{G}_4(kx)$: $\tilde{G}(kx) = 1 + \exp[-2kb(x^2 - 1)^{1/2}]$


DAT
FILM